Astronomical seeing conditions as determined by turbulence modelling and optical measurement

by

Marisa Nickola

Submitted in partial fulfilment of the requirements for the degree

MASTER OF SCIENCE

in the Faculty of Natural & Agricultural Sciences

University of Pretoria

Pretoria

South Africa

November 2012

Astronomical seeing conditions as determined by turbulence modelling and optical measurement

Author:	Nickola Marisa
Promoter:	Prof. George Djolov[1] and
	Prof. Ludwig Combrinck[1, 2]
Department:	[1]Department of Geography, Geoinformatics and Meteorology,
	University of Pretoria, Pretoria 0002, South Africa
	[2]Hartebeesthoek Radio Astronomy Observatory (HartRAO),
	P.O. Box 443, Krugersdorp 1740, South Africa
Degree:	Master of Science

Abstract

Modern space geodetic techniques are required to provide measurements of millimetre-level accuracy. A new fundamental space geodetic observatory for South Africa has been proposed. It will house state-of-the-art equipment in a location that guarantees optimal scientific output. Lunar Laser Ranging (LLR) is one of the space geodetic techniques to be hosted on-site. This technique requires optical (or so-called astronomical) seeing conditions, which allow for the propagation of a laser beam through the atmosphere without excessive beam degradation. The seeing must be at ~ 1 arc second resolution level for LLR to deliver usable ranging data. To establish the LLR system at the most suitable site and most suitable on-site location, site characterisation should include a description of the optical seeing conditions. Atmospheric turbulence in the planetary boundary layer (PBL) contributes significantly to the degradation of optical seeing quality. To evaluate astronomical seeing conditions at a site, a two-sided approach is considered – on the one hand, the use of a turbulence-resolving numerical model, the Large Eddy Simulation NERSC (Nansen Environmental and Remote Sensing Centre) Improved Code (LESNIC) to simulate seeing results, while, on the other hand, obtaining quantitative seeing measurements with a seeing monitor that has been developed in-house.

Keywords: optical turbulence, astronomical seeing, large eddy simulation, seeing monitor, Lunar Laser Ranging (LLR).

List of Publications

The following contributions have been published in peer review journals or proceedings as part of this work or related to it.

1. **<u>Nickola, M.</u>**, Botha, R.C., Esau, I. and Djolov, G.D. and Combrinck, W.L. 2011. Site characterisation: astronomical seeing from a turbulence-resolving model. *South African Journal of Geology*, **114**(3-4): 581-584.

2. **<u>Nickola, M.</u>**, Esau, I. and Djolov, G. 2010. Determining astronomical seeing conditions at Matjiesfontein by optical and turbulence methods. *IOP Conference Series: Earth and Environmental Science*, **13**(1): 012010.

3. **<u>Nickola, M.</u>**, Botha, R. and Combrinck, W.L. 2009. Investigation of techniques to determine astronomical seeing conditions at Matjiesfontein. *Proceedings of the South African Geophysical Association 2009 Biennial Technical Meeting and Exhibition "Ancient rocks to modern techniques"*. Swaziland, 16-18 September 2009: 598-602.

Declaration

I, Marisa Nickola, hereby declare that the work on which this thesis is based, which I hereby submit for the degree Master of Science, Faculty of Natural and Agricultural Sciences at the University of Pretoria, is my own work except where acknowledgements indicate otherwise. This work has not previously been submitted by me for another degree at this or any other tertiary institution.

…………………………..

November 2012

Acknowledgements

This thesis is the result of research I carried out at the Hartebeesthoek Radio Astronomy Observatory under the Space Geodesy programme while registered at the University of Pretoria.

I would like to thank the following people and institutions for their assistance with the research:

- Prof George Djolov, Prof Ludwig Combrinck, Roelf Botha and Dr Igor Esau
- Hartebeesthoek Radio Astronomy Observatory (HartRAO) and especially Glenda Coetzer, Christina Botai and Sarah Buchner
- University of Pretoria and especially Prof Hannes Rautenbach, Ingrid Booysen, Corné van Aardt and fellow-student, Philbert Luhunga
- G.C. Rieber Climate Institute at the Nansen Environmental and Remote Sensing Center (NERSC)
- Inkaba yeAfrica and especially Elronah Smit
- Dr Stoffel Fourie and the people of Matjiesfontein
- South African Astronomical Observatory (SAAO) and especially Laure Catala, Dr David Buckley, Dr Steve Crawford and Dr Timothy Pickering
- Dr Aziz Ziad and Yan Fantei-Caujolle from the University of Nice
- The South African Weather Service (SAWS) and especially Colleen de Villiers and Dr Jan Gertenbach
- Roelof Burger from the Climatological Research Group at the University of the Witwatersrand (Wits)
- Jaco Mentz , Prof Johan van der Walt, Prof Pieter Meintjies and Willie Koorts
- Johan Posthumus and Gerda Herne from Promethium Carbon Pty Ltd
- Eric Aristidi, Eric Fossat, Hubert Galleé, Florent Losse, Andreas Muschinski, Andrea Pelligrini, Tony Iaccarino, Tatanya Sadibekova and Mark Swain
- Gerhard Koekemoer, Wayne Mitchell, Johan Smit, Oleg Toumilovitch and Andrie van der Linde
- Mike Cameron
- Leslie Nickola as well as Golda and Tewie Muller

Table of Contents

List of Tables

List of Figures

List of Abbreviations and Acronyms

AA	: Angle of Arrival
AC	: Achromatic
A/D	: Analogue to Digital
ADC	: Analogue-to-Digital Conversion
AGAP	: Astronomy Geographic Advantage Protection
alt-az	: altitude-azimuth
APO	: Apochromatic
APOLLO	: Apache Point Lunar Laser-ranging Operation
AWS	: Automatic Weather Station
C-BASS	: C-Band All Sky Survey
CCD	: Charge-Coupled Device
CFL	: Courant-Fridrihs-Levi
CO-SLIDAR	: COupled SLodar scIDAR
CRF	: Celestial Reference Frame
CTIO	: Cerro Tololo Inter-American Observatory
D/A	: Digital to Analogue
DB64	: DATABASE64
DC	: Direct Current
Dec	: Declination
DIMM	: Differential Image Motion Monitor
DNS	: Direct Numerical Simulation
Dobs	: Dobsonian
DORIS	: Doppler Orbitography and Radiopositioning Integrated by Satellite
EOP	: Earth Orientation Parameters
FF	: Full-Frame
FL	: Focal Length
FOV	: Field Of View
FWC	: Full-Well Capacity
FWHM	: Full Width at Half Maximum
G-SCIDAR	: Generalised SCIDAR
GE	: German Equatorial
GEM	: German Equatorial Mount
GNSS	: Global Navigation Satellite System

GPS	: Global Positioning Satellite
GSM	: Generalized Seeing Monitor
GUI	: Graphical User Interface
HartRAO	: Hartebeesthoek Radio Astronomy Observatory
HVR-GS	: High Vertical Resolution G-SCIDAR
IAC	: Instituto de Astrofisica de Canarias
IEEE	: Institute of Electrical and Electronics Engineering
IL	: InterLine
ING	: Isaac Newton Group of Telescopes
IPEV	: Institut Polaire Français Paul Emile Victor
KAT	: Karoo Array Telescope
LES	: Large Eddy Simulation
LESNIC	: Large Eddy Simulation NERSC Improved Code
LLR	: Lunar Laser Ranging
LOLAS	: Low Layer SCIDAR
LuSci	: Lunar Scintillometer
M-N	: Maksutov-Newtonian
MASS-DIMM	: Multi-Aperture Scintillation Sensor - Differential Image Motion Monitor
MeerKAT	: Karoo Array Telescope (larger array)
MLRO	: Matera Laser Ranging Observatory
MLRS	: McDonald Laser Ranging Station
NERSC	: Nansen Environmental and Remote Sensing Center
ORM	: Observatorio del Roque de los Muchachos
OCA	: Observatoire de la Côte d'Azur
OS	: Operating System
OTA	: Optical Tube Assembly
PBL	: Planetary Boundary Layer
PBL	: Profileur Bord Lunaire (or Lunar Limb Profiler)
PE	: Periodic Error
PEC	: Periodic Error Correction
PMT	: Photo-Multiplier Tube
PNRA	: Programma Nazionale di Ricerche in Antartide
PPEC	: Permanent Periodic Error Correction

PSF	:	Point Spread Function
RA	:	Right Ascension
RANS	:	Reynolds-Averaged Navier-Stokes
RC	:	Ritchey-Chrétien
RFI	:	Radio Frequency Interference
RH	:	Relative Humidity
S/LLR	:	Satellite/Lunar Laser Ranging
S-N	:	Schmidt-Newtonian
SAAO	:	South African Astronomical Observatory
SALT	:	South African Large Telescope
SAWS	:	South African Weather Service
SBL	:	Stably stratified planetary Boundary Layer
SCIDAR	:	SCIntillation Detection And Ranging
SCT	:	Schmidt-Cassegrain Telescope
SHABAR	:	SHAdow BAnd Ranging
SI	:	Scintillation Indice
SKA	:	Square Kilometre Array
SLODAR	:	SLOpe Detection And Ranging
SLR	:	Satellite Laser Ranging
SNODAR	:	Surface layer NOn-Doppler Acoustic Radar
SODAR	:	SOnic Detection And Ranging
TRF	:	Terrestrial Reference Frame
USB	:	Universal Serial Bus
VLBI	:	Very Long Baseline Interferometry
WF	:	Weighting Function

1. Introduction

1.1 Background

Demands for increased performance and accuracy are being placed on global geodetic networks. The Hartebeesthoek Radio Astronomy Observatory (HartRAO) Space Geodesy Programme operates from a site in close proximity to cities and industrial areas, which are sources of air and light pollution as well as Radio Frequency Interference (RFI). Cloud cover and obsolete instrumentation also adversely affect geodetic data quantity and quality at the current site. This has necessitated the establishment of a new fundamental space geodetic observatory in South Africa (Combrinck *et al.*, 2007). The space geodetic observatory will host state-of-the-art equipment at a site suitable for optimal scientific output with the current site of choice being Matjiesfontein. A Satellite/Lunar Laser Ranging (S/LLR) system is under development and will form part of the geodetic instrumentation to be located at Matjiesfontein.

The LLR technique is used to measure the distance to the Moon – an LLR system on the Earth transmits a beam of laser pulses to one of several retro-reflector arrays on the Moon with the aim of measuring the round-trip time-of-flight of reflected return photons and calculating the distance travelled. The LLR's laser beam becomes diverged and the beam energy profile is adversely affected during propagation from the Earth to the Moon and back. To be successful, LLR requires optimal optical (/astronomical) seeing conditions, which will allow for the propagation of a laser beam through the atmosphere without excessive beam degradation. Site characterisation should therefore include determination of astronomical seeing conditions for various locations on-site as well as overall atmospheric conditions (Combrinck *et al.*, 2007).

1.1.1 Space geodesy

The following description is partially based on a report by the Committee on the National Requirements for Precision Geodetic Infrastructure, Committee on Seismology and Geodynamics and National Research Council (2010):

Geodesy is the science of measuring many aspects of the Earth - its size, shape, rotation, orientation and gravitational field - and other geodynamic phenomena such as crustal and polar motion as well as ocean tides. Space Geodesy is geodesy utilising extra-terrestrial objects such as artificial satellites, the Moon and quasars as reference points, allowing for measurement and representation of the Earth in three-dimensional time-varying space. Space Geodesy helps in understanding the Earth-Atmosphere-Oceans systems interaction.

Space geodesy techniques allow for determining station position, Celestial and Terrestrial Reference Frames (CRF and TRF), Earth Orientation Parameters (EOP), Earth rotation and gravity field, time, tectonic plate motion, tropospheric parameters, orbits of satellites as well as the Moon's distance, orientation and motion, amongst others. These data products are influenced by processes such as crustal motion, earthquakes and volcanism, ocean and atmospheric circulation, weather and climate, solid Earth and ocean tides, sea and ice sheet level changes and postglacial rebound, allowing scientists to model these processes.

Four major space geodesy techniques are used to measure Earth crustal dynamic parameters at sub-centimetre accuracy, with each of these techniques having its own unique observable:

- Geodetic Very Long Baseline Interferometry (VLBI) allows for determining distances between radio telescopes in a global network with an accuracy of several millimetres. This is inferred from varying arrival times of a quasar signal at the different radio telescopes.
- The Global Navigation Satellite System (GNSS) allows for determining antenna-satellite distances from the arrival times of GNSS satellite signals at receiver antennas on Earth, and also allows for determining three-dimensional position, velocity and time.
- Doppler Orbitography and Radiopositioning Integrated by Satellite (DORIS) is a technique whereby signals are transmitted from beacons on the Earth to satellites in orbit. From the observed Doppler shift, satellite orbits and station positions can be determined.

- Satellite/Lunar Laser Ranging (S/LLR) allows for determining the range between a ground station and a satellite (SLR) or the Moon (LLR) by transmitting laser pulses from the ground station to a satellite or Moon. The pulses are reflected back to the ground station's telescope by retro-reflectors placed on the satellite or Moon. By measuring the round-trip time-of-flight of the laser pulse, the position of the satellite or station or Moon can be determined with sub-centimetre accuracy.

Although each space geodesy technique has its own unique strength, all techniques work in synergy and for many final products, a combination of several techniques is used.

1.1.2 Lunar Laser Ranging

Lunar Laser Ranging is made possible by retro-reflector arrays deployed on the Moon during the Apollo 11, 14 and 15 missions as well as by retro-reflectors onboard two parked Soviet Lunakhod rovers (Figure 1.1 and Figure 1.2).

Figure 1.1. Location of LLR targets on the the Moon (source: NASA).
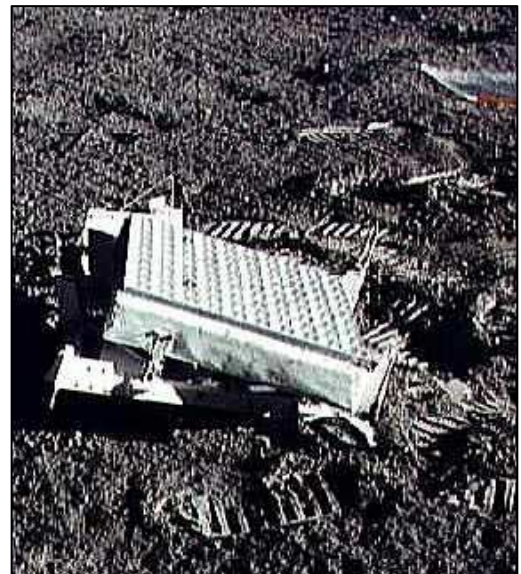
Figure 1.2. A retro-reflector array on the Moon's surface (source: NASA).

At a laser ranging observatory on Earth, powerful laser pulses are aimed through a large telescope and directed at the retro-reflectors on the Moon's surface. It is reflected back to the telescope at the observatory and the return signal time is measured. The round-trip travel time of a pulse allows one to translate it to the distance between the observatory and

the retro-reflector on the Moon. This is then translated to centre of mass (Earth) to centre of mass (Moon) for most data products (Combrinck *et al.*, 2007).

Currently there are only four operational LLR stations in the world, namely the Apache Point Observatory Lunar Laser-ranging Operation (APOLLO) in New Mexico and the McDonald Laser Ranging Station (MLRS) near Fort Davis in Texas, both in the United States of America (USA), the Observatoire de la Côte d'Azur (OCA) in Grasse, France, as well as the Matera Laser Ranging Observatory (MLRO) in Italy. At the Wettzell fundamental station in Bavaria, Germany, a lunar laser ranging system is under development. The aforementioned LLR stations are all located in the Northern Hemisphere. In the near-term, the only LLR in the Southern Hemisphere will be located in South Africa.

The accuracy of LLR allows for precise monitoring of the Moon's motion around the Earth, and the Moon's and Earth's relative acceleration towards the Sun, enabling verification of the Strong Equivalence Principle postulated in the theory of General Relativity. It also allows evaluation of the value of the gravitational constant G, in particular the estimation of the first order derivative of G. In addition to the Earth-Moon distance, LLR has also provided information about the structure and dynamics of the Moon and that of the Earth, such as (Dickey *et al.*, 1994) –

- the Moon's rotation rate, and motions caused by the Sun's and Earth's gravitational forces, provide evidence that the Moon possesses a small (radius < 350 km) liquid core;
- tidal friction is slowing the Earth's rotation causing the length of an Earth day to change by about 2 milliseconds per century, causing the Moon's orbit to expand at a rate of ~ 3.8 cm per year.

1.1.3   The need for a new fundamental space geodetic observatory

Space Geodesy in South Africa is operated from HartRAO as a base. HartRAO is situated in a valley in the Magaliesberg hills, approximately 50 km north-west of Johannesburg. Both radio astronomy and space geodetic research are performed at HartRAO. The

HartRAO Space Geodesy Programme focuses on the four major space geodesy techniques - VLBI, GNSS, DORIS and SLR (Figure 1.3). Long-term monitoring of Earth processes with these four space geodesy techniques from the very same site provides a trusted long-term data record. The co-location of the four space geodetic techniques makes HartRAO one of only five fiducial geodetic sites worldwide. It is also the only fundamental station in Africa. Located in Africa as well as the Southern Hemisphere, the station position is of strategic importance in the worldwide space geodesy network (Combrinck and Combrink, 2004).
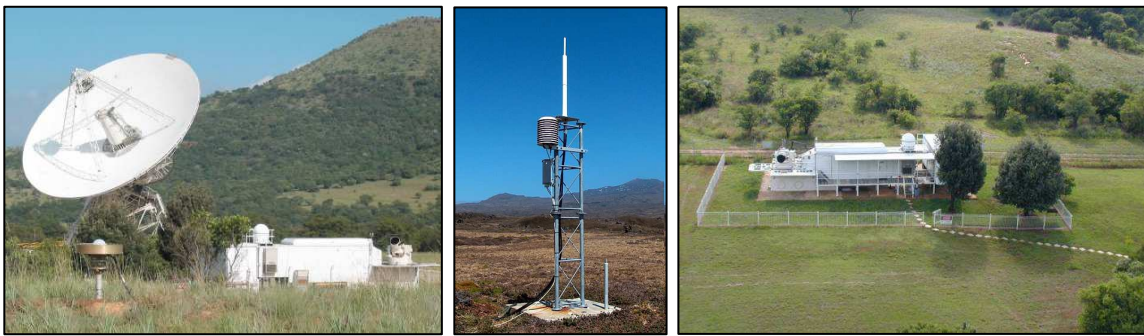
Figure 1.3. Space geodesy at HartRAO – VLBI, GNSS, DORIS (Marion Island) and SLR (MOBLAS-6).

Geodetic equipment at HartRAO is ageing and experiences more downtime than before. The HartRAO 26-m radio telescope does not meet VLBI2010 requirements for a future geodetic VLBI system. Currently, only 15% of telescope time is allocated to geodetic VLBI, whereas VLBI2010 requires continuous 24-hour VLBI observations. Currently, HartRAO operates at S (13 cm / 2.3 GHz) and X (3.5 cm / 8.6 GHz) bands only, while VLBI2010 requires operating up to 14 GHz. Another drawback of the current site at HartRAO is the increased pollution from the ever advancing city boundaries. It creates both RFI as well as deteriorating visibility of the sky at the site, limiting geodetic data quantity and quality. Also, cloud covered summer skies do not allow for optimal scientific output where laser ranging is concerned. The global geodetic network will be weakened considerably should HartRAO not participate in future space geodetic developments such as dedicated geodetic VLBI antennas, kilo-Hertz (kHz) SLR, densification of GNSS networks and near real-time data dissemination (Combrinck and Combrink, 2004; Combrinck et al., 2007).

Increased performance and accuracy are demanded from global geodetic networks. It has become apparent that HartRAO needs to build additional outstations. Establishing a new fundamental space geodetic observatory in a location suitable for optimal scientific output has been proposed (Combrinck and Combrink, 2004; Combrinck *et al*., 2007). All four main space geodetic techniques should be hosted on-site at a single location. The observatory will be equipped with advanced instrumentation. An LLR system is under development and will form part of the geodetic instrumentation at the new site. In an S/LLR collaboration with OCA in France, a 1-m aperture Cassegrain telescope has been donated by OCA to HartRAO (Figure 1.4). It will have to be refurbished before installation and a new generation LLR system will have to be designed and built to utilise this telescope.

Figure 1.4. The OCA 1-m aperture Cassegrain telescope mount and tube at HartRAO.

The new fundamental space geodetic observatory is to be deployed on a site most suitable for high quantity and quality data output, i.e. a site with a benign atmosphere and reduced RFI. According to Combrinck *et al*. (2007), site requirements include:

- Stable bedrock – Location on deep soils or expansive clays would bias short-term and long-term results. Installation of a superconducting gravimeter and precision GNSS receiver to detect solid Earth movements would allow for modelling of Earth-tide, pole-tide, ocean and atmospheric loading motion and the vertical motion of the site to

be determined. This combination would enable the use of site-specific models, in particular by using Love numbers which are 'tuned' to a specific site.

- Protection from RFI – Locating the site in a protected valley would reduce chances of RFI from sources such as cellular phones and microwave ovens.

- Dry, clear and non-turbulent skies presenting good astronomical seeing conditions – Earth's atmosphere absorbs and distorts light and radio waves. Installation of a weather station and seeing monitor with state-of-the-art instruments to map parameters such as pressure, cloud coverage and seeing conditions.

- Low horizon cut-offs – Open sky is required for early source acquisition. An average horizon level of ~ 15° or better is required.

- Accessibility and infrastructure such as roads, electricity and water.

- Internet access and sufficient bandwidth is required for autonomous operation and streaming data.

Investigations into a possible new location for a fundamental space geodetic station started in 2002 (Combrinck and Combrink, 2004). Potential sites within southern Africa identified initially included only Lesotho, Sutherland and Matjiesfontein. Recently Klerefontein and other sites in the Eastern Cape and KwaZulu-Natal have been added to the list of possible sites. A short description of potential sites is provided in Appendix A1.

1.1.4 Astronomical seeing determined by turbulence and optical methods

Turbulence in the atmosphere causes dispersion and divergence of the LLR's laser beam. Astronomical seeing is a term used to quantify turbulence in the Earth's atmosphere. Image degradation and positional shifts are manifestations of turbulence in the Earth's atmosphere. Plane wave fronts emanating from stars are distorted by index of refraction variations caused by turbulent layers in the atmosphere. From the change in a stellar image relative to that expected under perfect conditions, a quantitative measure of seeing conditions can be derived (Roddier, 1981; Coulman, 1985; Roggeman and Welsh, 1996). The LLR return signal consists of a small number of photons. Single photon detection from the Moon is a non-trivial task (Combrinck et al., 2007), therefore optimal astronomical seeing conditions of ≤ 1 arc-second resolution level is required for ranging success.

Seeing quality is significantly degraded by atmospheric turbulence in the boundary layer (lowest part of the atmosphere affected by interaction with Earth's surface). Integration of methods from instruments measuring astronomical seeing and boundary layer meteorology (models) is necessary to link astronomical seeing conditions with time-space variations of atmospheric properties caused by turbulent processes (Erasmus, 1988; Erasmus, 1996).

1.2   Motivation for the research

As an international facility, the new fundamental space geodetic observatory will be expected to meet international standards for data quantity and quality. Adverse astronomical seeing conditions (atmospheric turbulence) present severe limitations on the quantity and quality of data collected, therefore all space geodesy techniques require a benign atmosphere. For the S/LLR to achieve the required accuracy in tracking calibration stars, satellites and the targets on the Moon, astronomical seeing conditions of ≤ 1 arc-second resolution level are required. A very important consideration for a specific site is that the laser beam diverges at a ratio directly proportional to the astronomical seeing conditions. For example, for every 1 arc-second of seeing, the laser beam will have diverged 2 km by the time it strikes the surface of the Moon. Sites with poor seeing conditions would reduce the chance of receiving a sufficient number of return photons to such an extent that LLR would simply not be possible. Calculations for a link budget indicate that for seeing conditions of 2 arc-seconds, only about 5-7 photons per minute would be captured. A proper characterisation of astronomical seeing conditions at the best proposed locations is therefore essential.

1.3   Aim and objectives

A two-pronged approach to determine astronomical seeing conditions at a potential site is proposed – the use of a turbulence-resolving numerical model, the Large Eddy Simulation NERSC (Nansen Environmental and Remote Sensing Centre) Improved Code (LESNIC) (Esau, 2004), to simulate atmospheric boundary-layer structure and behaviour, in conjunction with a seeing monitor for on-site quantitative measurements of seeing conditions (Roddier, 1981).

The overall aim of this study is to determine whether a turbulence-resolving numerical simulation model, such as LESNIC, and an in-house developed seeing monitor can be utilised to determine astronomical seeing as part of site characterisation for a new fundamental space geodetic observatory.

The overall aim will be achieved by the following objectives:

OBJECTIVE 1

Make use of LESNIC to obtain modelled seeing results and verify these results against observed results obtained during field campaigns as reported in the literature.

OBJECTIVE 2

Investigate the optimal design for a seeing monitor and verify scientific functionality of the seeing monitor equipment and techniques employed.

OBJECTIVE 3

Investigate how parameters of modelled results obtained with LESNIC may be used in conjunction with measured results from the seeing monitor to predict the seeing at a site.

1.4   Method

To determine astronomical seeing conditions at a proposed site, a two-pronged approach of simulation and measurement, using methods from both boundary layer meteorology and astronomical seeing, was envisaged. The Large Eddy Simulation (LES) method was extended to calculate turbulence profiles and seeing parameter values and tested using the LESNIC model. Simulated results for turbulence profiles and seeing parameter values were provided by the LESNIC model for a site for which the necessary meteorological data were available. Quantitative seeing measurements were obtained at Matjiesfontein by employing a seeing monitor designed in this study. In a future study (not conducted during this work),

the relationship between modelled and measured seeing conditions at a particular site should be investigated and an integrated system developed.

Cost and availability of equipment dictate the possible methods to be employed for determining astronomical seeing conditions and boundary layer meteorology at a proposed site for the new fundamental space geodetic observatory. Although *in-situ* experimental methods for determining seeing conditions are difficult, time-consuming and expensive, seeing is not stationary and requires near real-time monitoring necessitating continuous operations. It was decided to investigate the possibility of developing an in-house seeing monitor for on-site quantitative measurements of seeing conditions. Double star separation measurements were used for calibration and verification purposes (Napier-Munn, 2008). With this system it is possible to determine the column seeing (the column of the atmosphere through which the telescope is observing and the laser beam is propagating) as would be experienced by an optical telescope or laser beam.

A more general approach to secure data for the huge variety of Planetary Boundary Layer (PBL) states is not possible with the seeing monitor. The use of a turbulence-resolving numerical model, the Large Eddy Simulation NERSC Improved Code (LESNIC) (Esau, 2004), to simulate atmospheric boundary-layer structure and behaviour, was therefore proposed and an appropriate script for calculating turbulence profiles and seeing parameter values was developed.

A model, such as LESNIC, would allow for predicting approximate and general seeing at a site (seeing scenarios), whereas the seeing monitor would make actual measurements to determine column seeing as at the time of measurement. The two techniques are therefore supportive of each other, but one must realise the suitability of each for their particular field of application. A combined approach could be used to rapidly select sites using the LESNIC model, followed with site specific testing using a seeing monitor to determine the better site from the modelled selection.

1.5   Study outline

The thesis consists of seven chapters. In Chapter 2, the theoretical background linking astronomical seeing conditions to atmospheric turbulence is provided. Chapter 3 follows with a description of the experimental methodology employed in deriving astronomical seeing from LESNIC and DATABASE64 results, as well as that used in obtaining quantitative seeing measurements with the seeing monitor. The design and automation of a seeing monitor setup, as well as support-infrastructure and -instrumentation required on-site, are described in Chapter 4. In Chapter 5, comparative results for turbulence profiles and seeing parameter values obtained from DB64 (not site-specific) and results measured over Dome C in Antarctica, as well as results from a seeing monitor setup verification test and preliminary results for the PSF technique, are presented. The use of a two-pronged complementary approach to measure and predict seeing at a site is proposed in Chapter 6. The investigation into the suitability of using a turbulence-resolving model such as LESNIC and an in-house developed seeing monitor to characterise astronomical seeing conditions at a site is rounded off in Chapter 7, which contains final conclusions and recommendations.

2. Theoretical background to seeing

2.1. Introduction

In this chapter, the theoretical background of atmospheric turbulence and astronomical seeing is presented. The origin of and processes involved in turbulence generation are discussed, as is the Kolmogorov statistical theory of turbulence (Kolmogorov, 1941) and the refractive index structure parameter, which gives a measure of optical turbulence strength in the atmosphere (Tatarski, 1961). Astronomical seeing is discussed with reference to diffraction- and seeing-limited telescopic observation. Required parameters are introduced to quantify optical seeing quality. Atmospheric turbulence and astronomical seeing are linked to each other through certain parameters.

2.2. Atmospheric turbulence

Atmospheric turbulence, which occurs mostly in the atmospheric layer closest to Earth, the Planetary Boundary Layer (PBL) / Atmospheric Boundary Layer (ABL)), degrades seeing. Turbulence results when the boundary layer between air masses with different temperatures breaks up into local unstable air masses, called eddies (Stull, 1988). The eddies act as weak, irregular lenses causing refractive index variations which can distort electromagnetic wave fronts (Roddier, 1981; Roggeman and Welsh, 1996). The vertical distribution of turbulence is given by the profile of the refractive index structure constant $C_N^{\,2}(h)$ (Tatarski, 1961; Roddier, 1981; Roggeman and Welsh, 1996; Andrews and Phillips, 2005).

2.2.1. Earth's atmosphere

Earth's atmosphere consists of an envelope of air held near the surface by the Earth's gravitational attraction. This mixture of gases mainly comprises nitrogen, oxygen, argon and carbon dioxide. Spatial-temporal variations in temperature and pressure are used to divide the atmosphere into different layers, namely the troposphere, stratosphere, mesosphere and thermosphere (Figure 2.1). The troposphere is the lowest layer of the atmosphere. Here pressure and temperature decrease with altitude. Most of the turbulence

is also generated here, as most of the weather processes take place in this layer. The troposphere is composed of different molecules, one of which is water vapour, which plays a large role in controlling the troposphere's physical properties and processes. Water vapour drives structural and dynamical processes and carries latent heat for global redistribution of energy.
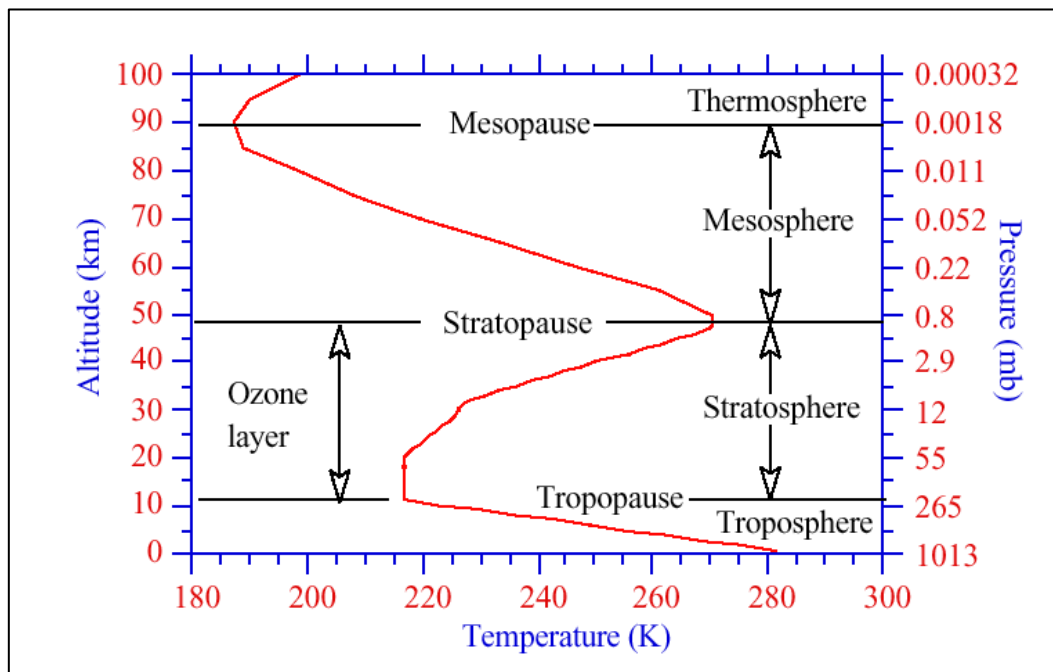
Figure 2.1. Temperature profile in the atmosphere (source: Claire E. Max, University of California, Santa Cruz).

Various forces influence the motion of the atmosphere. There are forces which affect horizontal flow - the pressure gradient force, friction and the Coriolis force, which is due to the Earth's rotation. These horizontal forces change the speed and direction of the wind. There are also forces that affect the vertical motion of the atmosphere - gravity, friction, buoyancy and terrain features all influence the wind's vertical motion.

The PBL is directly influenced by interaction with the Earth's surface and, depending on time of day and weather conditions, varies from surface level up to an altitude of ~ 200 m to 2 km (Trinquet and Vernin, 2006) (Figure 2.2). Turbulence occurs mainly in the surface layer [0 to 100 m], planetary boundary layer [0 to 2 km] and free atmosphere [2 to 30 km]. The most disruptive turbulence occurs near the Earth's surface. The PBL therefore

contributes significantly to the degradation of optical seeing quality. The index of refraction fluctuations affecting astronomical seeing are located mainly in the PBL of the troposphere.
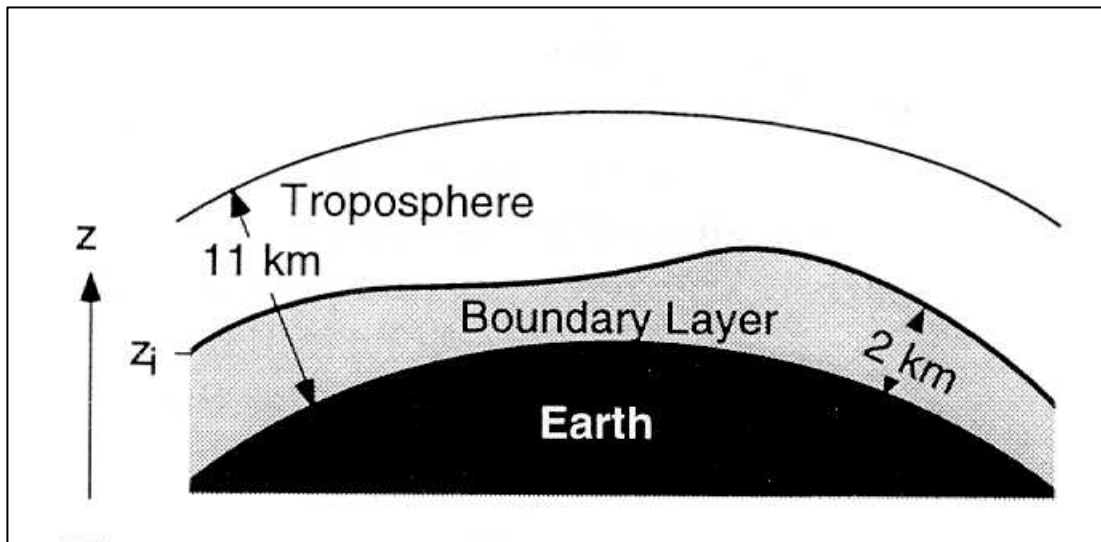
Figure 2.2. Planetary boundary layer (PBL) (source: Stull, 1988).

Turbulence in the PBL is responsible for the vertical transportation of surface turbulent fluxes of momentum, mass as well as sensible and latent heat. Friction acts on the ambient flow, creating wind shears, which are changes in the direction and speed of wind with height. Turbulent eddies are formed by these wind shears. The size of the turbulent eddies is proportional to the size and shape of the obstacles in the wind's path and also depends on the wind's speed. Mean profiles of wind speed, wind direction, temperature and humidity in the PBL are controlled or mixed by turbulent eddies.

The PBL can be divided into four sub-layers: the surface layer, the mixed layer, the stable layer, and the residual layer (Figure 2.3). The surface layer is the sub-layer closest to Earth. Molecular viscosity dominates at centimetre-level close to the surface and above it in this layer, and turbulence is relatively constant and isotropic. A mixed layer forms when turbulent mixing is produced mainly by convective motion. Turbulent motion in the mixed layer is driven by wind shear and buoyancy forcing (Moeng and Sullivan, 1994). Coherent eddies (thermals, plumes, vortices) cause turbulent fluxes of momentum, heat and other scalars such as humidity, gases (e.g. carbon dioxide) and pollutants (Chou and Ferguson,

1991). The residual layer begins to form when turbulence and the mixed layer decay on sunset. This (residual) layer is not directly influenced by the Earth's surface.
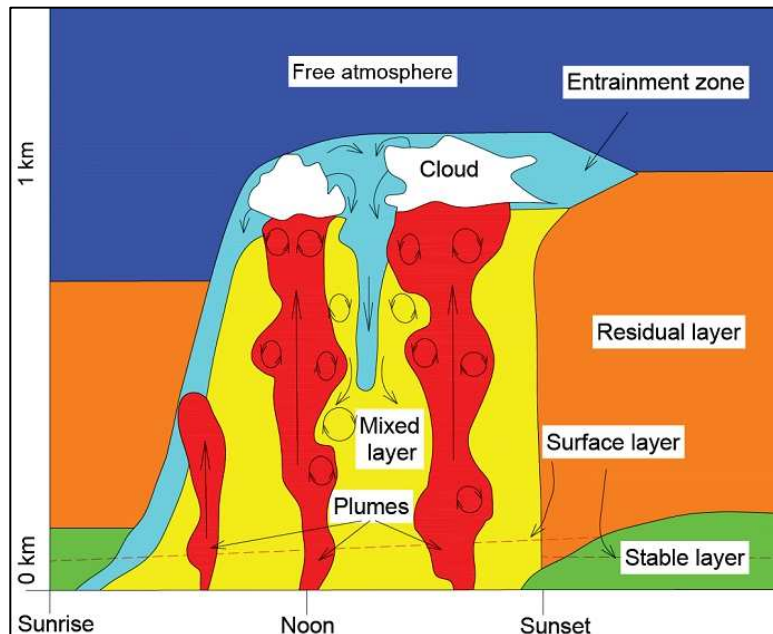
Figure 2.3. The PBL regions (source: University of Wisconsin Lidar Group (adapted)).

As the sun sets, convective motion decreases. The lower part of the PBL is stabilised by radiative cooling and surface friction. A stable boundary layer (SBL), in which turbulence is intermittent and affected by the underlying terrain, is formed. Turbulence in the lower layer of the SBL is locally coherent (Grant, 1992). It is weak, sporadic and contains a large portion of the night-time heat flux (Nappo, 1991).

Generation of turbulence in the PBL is influenced by factors such as energy budgets, moisture, diurnal variations, buoyancy, shear and roughness length. The amount of energy entering and leaving the PBL determines the surface heating. The magnitude of convective turbulence generated in the PBL is determined by this surface heating, while the amount of mechanical turbulence formed in the PBL is determined by wind shear. A rapid change in wind speed and direction causes instabilities and energy cascade of turbulent eddies of different sizes. Heterogeneous surface properties such as water, vegetation, land cover, buildings and forests also influence turbulence in the PBL. These properties create differences in surface fluxes of momentum, heat and moisture. Together with terrain

irregularities, these surface fluxes produce transient eddies, which modify turbulent fluxes within the PBL.

2.2.2. Turbulence theory

Image degradation is caused by atmospheric turbulence. In order to understand the optical properties of the atmosphere, it is therefore necessary to understand the processes involved in generating atmospheric turbulence. In his work, A.N. Kolmogorov (1941) founded the field of the statistical analysis of turbulence. The Kolmogorov theory of turbulence was further developed by Obukhov (1941), Tatarski (1961), Fried (1965) and Fried (1966). The following discussion of Kolomogorov turbulence is based on descriptions that can be found in Tatarski (1961), Roddier (1981), Roggeman and Welsh (1996) as well as Andrews and Phillips (2005), the latter work having been referred to extensively. In the Kolmogorov model of turbulence (Kolmogorov, 1941) (Figure 2.4), it is assumed that the medium is incompressible and that small-scale turbulence is homogeneous and isotropic. Energy is added on the largest scales, transferred to progressively smaller scales and dissipated by viscous action. This cascade process is responsible for variations in temperature and density, which leads to refractive index variations.
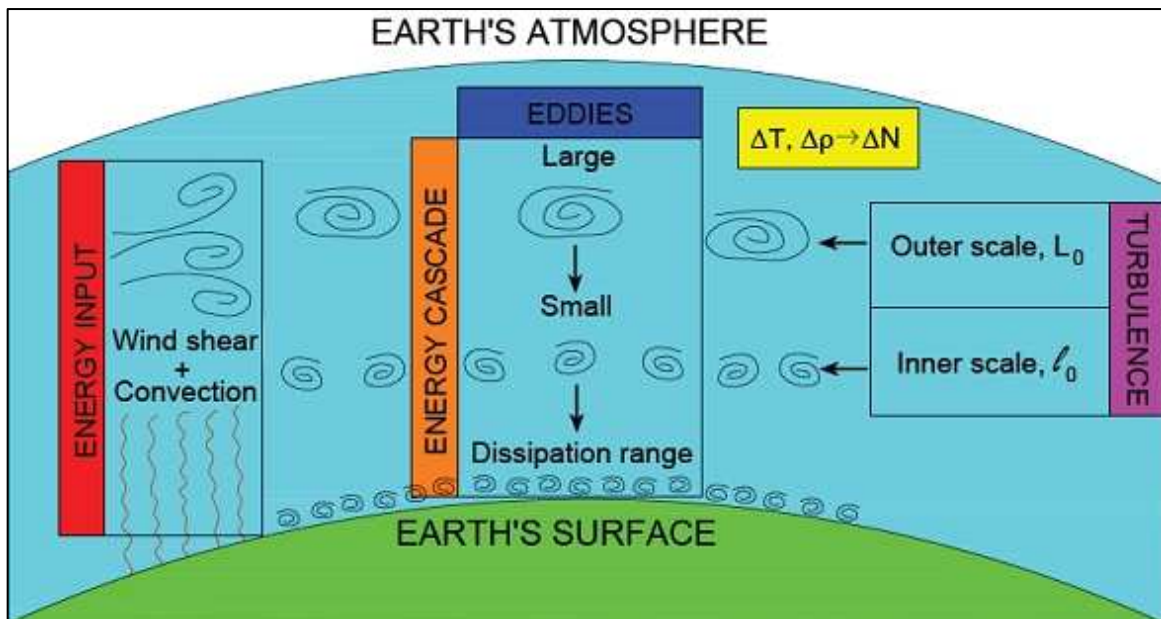
Figure 2.4. Kolmogorov model of turbulence.

The atmosphere, which can be treated as a viscous fluid, displays either laminar or turbulent flow. Turbulent flow is not stable or linear, but chaotic, and it is characterised by mixing. Eddies with different temperatures are mixed by wind and convection and break up into smaller structures. The mixing produces fluctuations in density and therefore in the refractive index of air. Eddies have large and small scales referred to as the outer scale of turbulence L_0 and the inner scale of turbulence l_0, respectively. Here L_0 ranges from 10 – 10^2 m and has wind shear or convection as energy source. Small scale eddies are too small to impart energy to the flow but large enough to avoid energy dissipation by friction. The inner scale of turbulence l_0 is on the order of a 10^{-3} m in size. Eddies with scale sizes smaller than the inner scale (Kolmogorov scale) are subject to viscous dissipation and belong to the dissipation range. Thus, energy flows from L_0 to l_0 and is dissipated by friction.

The Reynolds number Re gives the critical value at which the flow of a viscous fluid changes from laminar to turbulent. When dynamic forces of flow exceed damping forces of viscosity, the Reynolds number exceeds the critical value and turbulence results. The flow becomes unstable, forming vortices, which grow large enough to interfere with neighbouring eddies and is dominated by chaotic interactions between the eddies. The Reynolds number Re is a dimensionless quantity given by

$$\mathrm{Re} = \frac{VL}{\nu} \quad \left(\frac{[m.s^{-1}][m]}{[m^2.s^{-1}]} \right),$$
(2.1)

where V and L represent characteristic velocity and length scales of the flow and ν is the kinematic viscosity.

Kolmogorov introduced structure functions to provide a statistical description of the random processes involved in turbulence. With turbulence, variables such as velocity, temperature, pressure and humidity are non-stationary and therefore do not have well-defined averages. By making use of stationary increments it is possible to find well-defined averages of the differences between the values. A structure function is an example of this type of quantity and allows for determining the intensity of fluctuations over a short time scale. A structure function is thus a measure of the intensity of fluctuations of a non-

stationary random variable over a short time scale. The structure function $D_x(R)$ of a random variable x (e.g. temperature, index of refraction etc.), measured at two points separated by distance R, is defined by

$$D_x(R) = \left\langle \left(x_1 - x_2 \right)^2 \right\rangle. \tag{2.2}$$

Kolmogorov's theory of turbulence was developed considering velocity fluctuations of the turbulent field. Kolmogorov introduced the longitudinal velocity structure function, parallel to the vector $\vec{R}$ connecting two points separated by distance R, to describe velocity field fluctuations

$$D_V(R) = \left\langle \left(V_1 - V_2 \right)^2 \right\rangle, \tag{2.3}$$

where V_1 and V_2 [m.s^{-1}] are velocities measured at two points separated by distance R, and the triangle brackets denote ensemble averages. A similar expression applies to any conservative, passive additive such as temperature (temperature fluctuations do not exchange energy with the velocity field). By extending the Kolmogorov theory of the structure function to statistically homogeneous and isotropic temperature fluctuations, the structure function of the temperature field is similarly described by

$$D_T(R) = \left\langle \left(T_1 - T_2 \right)^2 \right\rangle, \tag{2.4}$$

where T_1 and T_2 [K] are temperatures measured at two points separated by distance R, and the triangle brackets denote ensemble averages.

In order to derive a universal description for the turbulence spectrum, Kolmogorov proposed that, in locally isotropic turbulence, the cascade of energy from large scales to smaller scales leads to a statistically self-similar model that depends only on two parameters, the energy dissipation rate ε and the kinematic viscosity ν. Kolmogorov used a dimensional analysis argument combining these parameters to form characteristic time, velocity, and length scales, which were then used to derive the velocity structure function. Assuming isotropic and homogeneous turbulence, and arguing that the structure function of the velocity field must be independent of viscosity in the inertial range (where dissipation does not play a role), the Kolmogorov-Obukhov two-thirds power law for the velocity field (Kolmogorov, 1941; Obukhov, 1941) is given by

$$D_V(R) = C_V{}^2 R^{2/3} \qquad l_0 << R << L_0 , \tag{2.5}$$

where $C_V{}^2$ [m$^{4/3}$s^{-2}] is a measure of the total amount of energy in the turbulence for separation distance R (which falls between the inner and outer scales of turbulence) between the two velocity measurements of Equation (2.3). This power law gives turbulence strength as a function of eddy size, the spatial correlation of turbulence decreasing in proportion to the two-thirds power of the spatial separation. The relationship is only valid for R in the inertial sub-range. By extending the Kolmogorov theory of the structure function to statistically homogeneous and isotropic temperature fluctuations, a similar two-thirds power law relation is found for the temperature field and is given by

$$D_T(R) = C_T{}^2 R^{2/3} \qquad l_0 << R << L_0 , \tag{2.6}$$

where the temperature fluctuation constant, also known as the temperature structure parameter, $C_T{}^2$ [m$^{-2/3}$] represents the thermal strength of the turbulence for separation distance R between the two temperature measurements of Equation (2.4).

2.2.3. Index of refraction structure parameter, $C_N{}^2$

As for the previous section, the following discussion and derivations follow the description in Andrews and Phillips (2005). The vertical distribution of turbulence, also known as the profile of the refractive index structure parameter $C_N{}^2(h)$, is a measure of the fluctuations in the refractive index field, and thus of the strength of optical turbulence responsible for image degradation. The index of refraction in air depends on temperature, pressure and water vapour content. At optical wavelengths, temperature fluctuations dominate water vapour fluctuations in contributing to refractive index fluctuations. Temperature and pressure variations are caused by velocity fluctuations. Pressure variations are rapidly smoothed out by sound waves, but conduction takes much longer to smooth out the variations in temperature. Temperature thus provides the important link between turbulent velocity and index of refraction N.

Analogous to the structure functions of the velocity and temperature fields, the structure function of the optical field is given by

$$D_N(R) = \left\langle (N_1 - N_2)^2 \right\rangle, \qquad (2.7)$$

where N_1 and N_2 are the atmospheric refractive index measured at two points separated by distance R, and the triangle brackets denote ensemble averages. The Kolmogorov-Obukhov two-thirds power law of Equation (2.5) also describes the structure function of the refractive index fluctuations in the inertial sub-range, which is given by

$$D_N(R) = C_N{}^2 R^{2/3} \qquad l_0 << R << L_0, \qquad (2.8)$$

where the refractive index structure parameter $C_N{}^2$ [m$^{-2/3}$] represents the strength of optical turbulence for separation distance R between the two refractive index measurements of Equation (2.7). The wave is assumed to maintain a single frequency as it propagates, therefore time variations are not taken into account.

At optical wavelengths, the index of refraction for the atmosphere is given by

$$N - 1 \cong 79 \times 10^{-6} \frac{P}{T}, \qquad (2.9)$$

where P is the pressure in hectopascal [hPa] and T the temperature in Kelvin. Refractive index fluctuations with respect to temperature variations are obtained by differentiating Equation (2.9) to give

$$\frac{\partial N}{\partial T} = \frac{-\left(79 \times 10^{-6}\right) P}{T^2}. \qquad (2.10)$$

The index of refraction and temperature structure parameters are obtained by combining Equation (2.7) with Equation (2.8) and combining Equation (2.4) with Equation (2.6), respectively, to give

$$C_N{}^2 = \frac{\left\langle (N_1 - N_2)^2 \right\rangle}{R^{2/3}} \qquad (2.11a)$$

and

$$C_T{}^2 = \frac{\left\langle (T_1 - T_2)^2 \right\rangle}{R^{2/3}}, \qquad (2.11b)$$

where $\left\langle (N_1 - N_2)^2 \right\rangle$ and $\left\langle (T_1 - T_2)^2 \right\rangle$ represent ensemble averages of index of refraction fluctuations, N_1 and N_2, and temperature fluctuations, T_1 and T_2, respectively, at two points separated by a distance R.

Combining the two equations for the index of refraction and temperature structure parameters as described in Equation (2.11a) and Equation (2.11b), respectively, with Equation (2.10), gives

$$C_N^{\ 2} = \frac{\left\langle \left(N_1 - N_2\right)^2 \right\rangle}{\left\langle \left(T_1 - T_2\right)^2 \right\rangle} C_T^{\ 2} = \left(\frac{\partial N}{\partial T}\right)^2 C_T^{\ 2} = \left(79 \times 10^{-6}\, \frac{P}{T^2}\right)^2 C_T^{\ 2}, \qquad (2.12)$$

which provides the index of refraction structure parameter $C_N^{\ 2}$ in terms of the temperature structure parameter $C_T^{\ 2}$ and ambient pressure P and temperature T.

The profile of the index of refraction structure parameter with height $C_N^{\ 2}(h)$ was derived by Tatarski (1961) as

$$C_N^{\ 2}(h) = \left(79 \times 10^{-6}\, \frac{P(h)}{T^2(h)}\right)^2 C_T^{\ 2}(h), \qquad (2.13)$$

where $C_N^{\ 2}(h)$ may be assumed constant for a given height h above ground and over small time scales at fixed propagation distance. The unit for both $C_N^{\ 2}$ and $C_T^{\ 2}$ is m$^{-2/3}$, while P is measured in hectopascal [hPa] and T is measured in Kelvin [K]. It is difficult to measure $C_N^{\ 2}$ directly. Rather, at a given height h, fast-response thermometers are employed to measure $C_T^{\ 2}$ and, together with the measured values of ambient temperature and pressure for that height h, are used to determine $C_N^{\ 2}$. Values for $C_N^{\ 2}$ usually range from 10^{-17} m$^{-2/3}$ up to 10^{-13} m$^{-2/3}$, for weak and strong turbulence, respectively.

2.3.   Astronomical seeing

The relationship between atmospheric turbulence and seeing quality is described in Tatarski (1961), Fried (1965), Fried (1966), Roddier (1981), Coulman (1985), Roggeman and Welsh (1996), Erasmus (1986), Erasmus (1988) and Erasmus (2000). From Section 2.2, it follows that, through index of refraction fluctuations, atmospheric turbulence can result in perturbations of electromagnetic wave fronts (Figure 2.5). For astronomical observations, these perturbations cause electromagnetic wave fronts from extra-terrestrial sources to undergo refraction, absorption, dispersion, blurring etc.
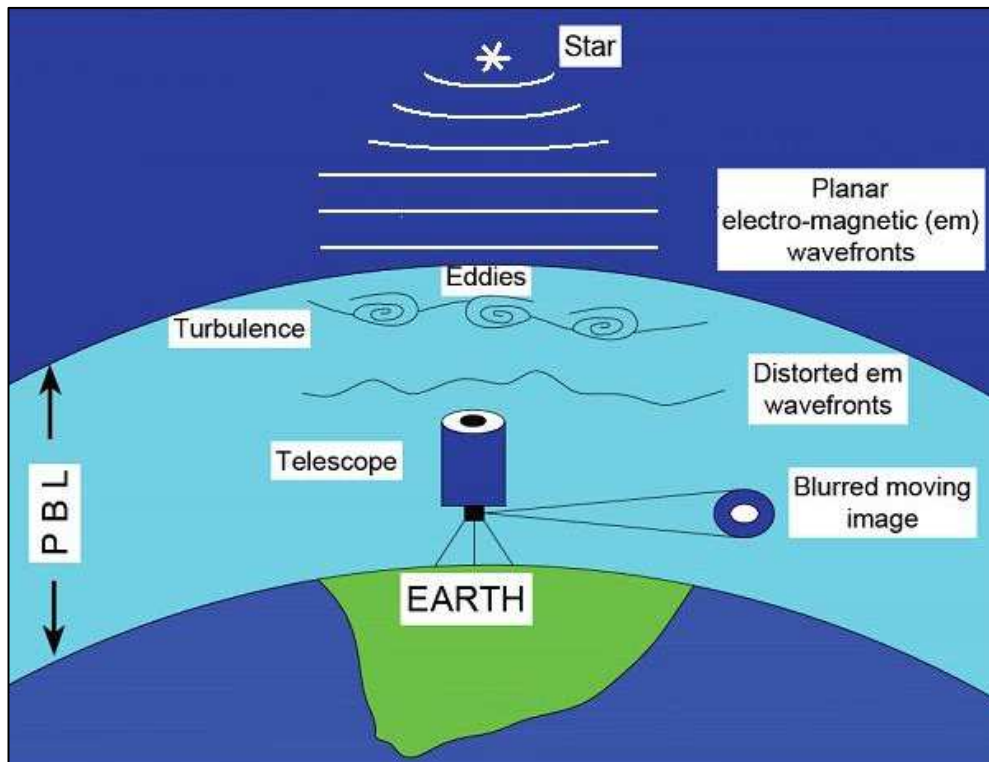
Figure 2.5. Degradation of image quality by turbulence.

Stars are located at an immense distance from the Earth and should therefore appear as no more than point sources when observed through a telescope (or by the naked eye). However, using a telescope on Earth, a star is observed as a blurred, moving image. Although image quality can be affected by the instrument's diameter and quality of optical components, the main contributor to the distortion is atmospheric turbulence.

The degradation of the image quality relative to that expected under ideal conditions provides a measure of the seeing conditions. Although a telescope's theoretical angular resolution, the Rayleigh limit, may be smaller than an arc-second, the image resolution will be limited further by atmospheric seeing conditions. For the purpose of seeing tests, one would usually choose a telescope large enough so that aperture is not the limiting factor for image quality. The smallest resolvable angle in such a setup will then provide the seeing used to measure seeing conditions in optical astronomy.

2.3.1. Diffraction limit of telescope

The following explanation for diffraction-limited telescopic observation is based on Léna (1986), Longair (1992) as well as Born and Wolf (1999). Stars, although point sources, do not form point images in the focal plane. Stars rather form discs due to diffraction of the light by lenses, mirrors and other internal components of the telescope. The light passing through the telescope's objective is diffracted. Under perfect seeing conditions, the light forms a bull's eye diffraction pattern (Figure 2.6). The diffraction pattern consists of light and dark rings with a small bright disc, the Airy disc, in the centre. The Airy disc, together with the concentric rings surrounding it, is known as an Airy pattern. The Airy disc represents the central maximum of the diffraction pattern and is the smallest point to which a light beam can be focused. Nearly 84% of light is concentrated in the Airy disc with the remainder contained in the light rings.
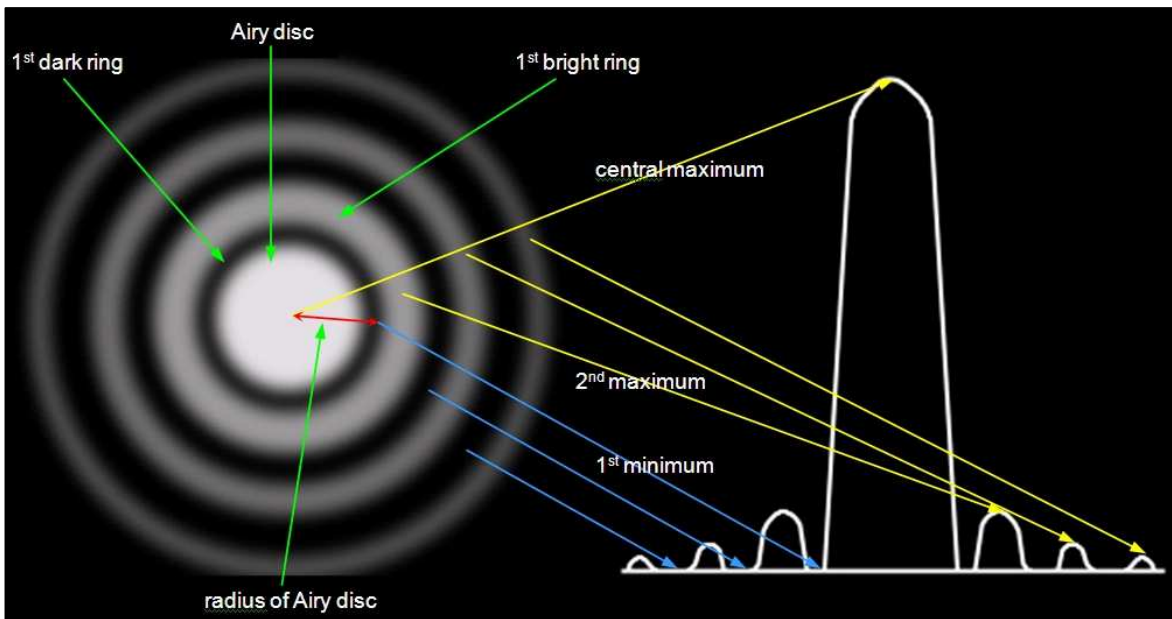
Figure 2.6. Diffraction pattern of star image through a telescope and profile of image brightness (source: http://starizona.com (adapted)).

The intensity of the diffraction pattern of a circular aperture, or Airy pattern, is given by the Airy function

$$I(\theta) = I_0 \left[\frac{2J_1(ka\sin\theta)}{ka\sin\theta} \right]^2 = I_0 \left[\frac{2J_1(x)}{x} \right]^2, \qquad (2.14)$$

where $I(\theta)$ is the intensity of radiation at observation angle θ from the axis of the circular aperture, I_0 is the central intensity of the Airy pattern, J_1 is a Bessel function of the first kind of order unity, $k = 2\pi / \lambda$ is the wave number, a is the radius of the circular aperture, and $x = ka \sin \theta$, with $I(\theta)$ reaching a maximum or zero depending on whether $2J_1(x)/x$ reaches its extremum or zero.

Diffraction effects limit the smallest diameter the Airy disc can take and therefore also the telescope's or imaging system's resolution. The angular size of the Airy disc is given by its radius from the centre of the disc (central maximum) out to the centre of the first dark interspace (inner, most conspicuous dark ring, the first minimum) between the central disc and the first bright diffraction ring (second maximum). Based on Airy diffraction theory, the Rayleigh criterion gives the theoretical resolution limit of a telescope, as determined by the radius of the Airy function's first null, and given by

$$\theta = 1.22 \frac{\lambda}{D} \quad (radians) \quad = 206265\left(1.22 \frac{\lambda}{D}\right) \quad (arc\text{-}seconds), \qquad (2.15)$$

where θ is the angular resolution, λ the wavelength of incoming light and D the telescope aperture diameter. Point sources separated by an angle smaller than this angular resolution cannot be resolved. The factor of 1.22 is derived from calculating the position of the first dark ring surrounding the central Airy disc (Argyle, 2004; Napier-Munn, 2008). The diameter of the disc is directly proportional to the wavelength of the light but inversely proportional to the telescope aperture. The Airy disc diameter gets smaller for light of shorter wavelength (i.e. higher frequency) and in instruments of larger aperture. Therefore bigger telescopes produce better images of stars, i.e. smaller Airy discs. The smaller the Airy disc, the less it intrudes on detail. Poor seeing conditions make it appear as an amorphous blob. Although a telescope's theoretical angular resolution may be smaller than an arc-second, the telescope's resolving power will be limited further by adverse seeing conditions.

In order to determine the resolution limit of a telescope, close double stars may be observed to determine the smallest angular separation of double stars that can be observed by the telescope. Dawes' limit is applicable to the resolution of double stars and is based

on the observation of a pair of sixth magnitude stars. According to Dawes' limit, the resolving power of the telescope R is given by

$$R = \frac{11.6}{D} \quad (arc\text{-}seconds),$$ (2.16)

where D is the aperture of the telescope in cm (Napier-Munn, 2008).

2.3.2. Fried parameter

The Fried parameter r_0 is a statistical parameter derived from the Kolmogorov model of turbulence (Kolmogorov, 1941) by Fried (1965) and Fried (1966). The Fried parameter describes the effect of the atmosphere on the performance of a telescope and provides a measure of image degradation due to atmospheric turbulence. Variations in refractive index produce phase fluctuations of the wave front entering the telescope. The turbulent field is statistically described by a structure function and given by

$$D_\varphi(\rho) = \left\langle \left(\varphi_1 - \varphi_2 \right)^2 \right\rangle,$$ (2.17)

where $D_\varphi(\rho)$ is the atmospherically induced variance between the phase at two parts of the wave front, φ_1 and φ_2, separated by a distance ρ in the aperture plane, and the triangle brackets denote ensemble averages. From this follows the phase structure function at the telescope aperture, given by

$$D_\varphi(\rho) = 6.88 \left(\frac{|\rho|}{r_0} \right)^{5/3},$$ (2.18)

where the coherence length r_0 (the Fried parameter) corresponds to the diameter of the telescope for which the resolution is beginning to be significantly affected by phase fluctuations (Tubbs, 2003). For telescopes with diameters larger than the Fried parameter, the resolution is no longer just limited by diffraction effects, but is also now seeing-limited. The resolution cannot be increased any further by increase of telescope aperture size (Travouillon, 2004).

Seeing can also be determined by measuring the smallest resolvable angular resolution of an object outside of Earth's atmosphere. Astronomers generally quantify the quality of optical seeing conditions at a particular site with a parameter they refer to as the "seeing".

Seeing ε_{FWHM} is described in terms of the Full Width at Half Maximum (FWHM) of the star's intensity profile, the Point Spread Function (PSF), at the focus of a telescope (Travouillon, 2004). Seeing ε_{FWHM} is related to the Fried parameter r_0 by (Dierickx, 1992)

$$\varepsilon_{FWHM} = 0.98 \frac{\lambda}{r_0} \quad (radians) \quad = 206265 \left(0.98 \frac{\lambda}{r_0} \right) \quad (arc\text{-}seconds) , \qquad (2.19)$$

where λ is the wavelength of observation.

A larger r_0 (therefore smaller ε_{FWHM}) indicates better seeing conditions. The Fried parameter r_0 typically takes on values of between 2 and 30 cm in the visible light range. This translates to seeing ε_{FWHM} values between 5.7" and 0.4", respectively, for $\lambda = 550\ nm$. The seeing is typically about one arc-second or less for a good astronomical site. The seeing quality of a site will vary with time and for different seasons (Travouillon, 2004).

2.4.   Link between atmospheric turbulence and astronomical seeing

In summary of what has been discussed in the preceding sections, in the PBL of the troposphere, atmospheric turbulence is caused by wind and temperature gradients which cause refractive index variations. The refractive index variations distort electromagnetic wave fronts resulting in image degradation.

The vertical distribution of turbulence, as given by the profile of the refractive index structure parameter $C_N^{\ 2}(h)$, allows for predicting atmospheric optical quality in terms of astronomical seeing. The integrated value of the index of refraction structure parameter for all atmospheric layers gives the total effect of the atmospheric turbulence and may be obtained by making use of the integral of Equation (2.13) and by measuring the atmosphere's temperature profile $C_T^{\ 2}(h)$ as well as the meteorological parameters, pressure P [hPa] and absolute temperature, T [K].

The Fried parameter r_0 may be determined from the $C_N^{\ 2}(h)$ profile by (Roddier, 1981)

$$r_0(\lambda, \gamma, h) = \left(16.7\lambda^{-2}\frac{1}{\cos\gamma}\int_0^\infty C_N^{\,2}(h)dh\right)^{-3/5}, \qquad (2.20)$$

where the turbulence strength $C_N^{\,2}(h)$ varies as function of height h above the telescope, γ is the angle relative to zenith and λ the wavelength of light. Usually γ is chosen at zenith with $1/\cos\gamma = 1$.

Therefore, the expression for seeing, Equation (2.19), becomes (Vernin and Muñoz-Tuñón, 1992)

$$\varepsilon_{FWHM} = 0.98\frac{\lambda}{r_0} = 5.25\lambda^{-1/5}\left(\int_0^\infty C_N^{\,2}(h)dh\right)^{-3/5}, \qquad (2.21)$$

and, knowing the wavelength of observation λ and height above the telescope h, the integrated value of the seeing ε_{FWHM} can be determined for a site. The inclusion of a turbulence-resolving model to obtain $C_N^{\,2}(h)$ profiles for a specific site also allows one to estimate seeing at the site.

3. Methodology

3.1. Introduction

In this chapter, boundary layer numerical modelling with a Large Eddy Simulation (LES) model named the Large Eddy Simulation NERSC (Nansen Environmental and Remote Sensing Center) Improved Code (LESNIC), a turbulence-resolving simulation code developed by Igor Esau (Esau, 2004) at G.C. Rieber Climate Institute at the Nansen Environmental and Remote Sensing Center, is discussed. Methodology employed to obtain astronomical seeing from this turbulence-resolving model and its DATABASE64, a collection of LESNIC runs, is explained in detail.

An optical method to measure astronomical seeing is also implemented. It is explained how seeing may be quantified experimentally by comparison of an ideal and observe image. For the seeing monitor to be able to measure sub-arcsecond seeing conditions, it must itself have a resolution of better than an arc-second. Factors such as image scale and sampling, which determine the resolution the seeing monitor is capable of, are specified. The experimental method pertaining to image capture, stacking and evaluation as well as the measurement of double star separations is outlined.

3.2. Modelling seeing by turbulence method

Atmospheric boundary-layer structure and behaviour may be simulated with numerical modelling (Garratt, 1992). With this approach, the PBL's dynamics, thermodynamics and interaction with the underlying surface are described by a set of differential equations, the Reynolds-averaged Navier-Stokes equations, and appropriate boundary conditions from fluid mechanics. Solutions of the equations are found by appropriate numerical methods. The volume occupied by the fluid is divided into a mesh. The governing equations with specified boundary and initial conditions are then solved for the mesh by applying a suitable algorithm.

Numerical models for solving the Navier-Stokes equations include Direct Numerical Simulation (DNS), Reynolds-Averaged Navier-Stokes (RANS) and Large Eddy Simulation (LES) (Pope, 2000). With LES, a more refined mesh than with RANS but a coarser mesh than with DNS is used. Solving the Navier-Stokes equations by DNS allows for the wide range of length and time scales associated with turbulent eddies to be resolved, but currently no computer exists with enough memory and speed to model configurations of the real PBL. By simply modelling the turbulent motions, as in the RANS approach, computational effort is reduced but depends heavily on the closure assumptions and does not provide finer PBL structure statistics. With LES, large eddies are resolved directly, while small eddies are filtered and modelled.

3.2.1. Large Eddy Simulation (LES)

According to Stull (1988), Garratt (1992) and Pope (2000), LES is based on the Kolmogorov model of turbulence, a statistical analysis of turbulence (Kolmogorov, 1941 and Tatarski, 1961). In the LES approach, local unstable air masses called eddies are either resolved or modelled (Figure 3.1). Large-scale eddies are resolved directly while small-scale eddies are filtered out and modelled. By numerically filtering out the smaller eddies, which cannot be resolved explicitly, equations that govern the dynamics of large eddies only can be determined

Large-scale eddies are transporters of momentum, mass, energy and other passive scalars and are more problem-dependent than small-scale eddies. Large-scale eddies are therefore resolved through solving filtered partial differential equations governing turbulent fluid flow – the Navier-Stokes equations.

Small-scale eddies dissipate their energy through viscous interactions and are less dependent on the flow geometry. They are more isotropic than the larger scale eddies and therefore more universal, increasing the chances of finding a universal model. The small-scale eddies are therefore filtered out numerically and modelled. A filter width or grid spacing is employed in computations to filter out these eddies of smaller scale. These sub-

grid scale eddies' effect on the flow is then parameterised and may be modelled with a universal subgrid-scale model.

If realistic fields are to be derived for wind, temperature, humidity and pressure, factors such as turbulence, atmospheric composition, radiation, clouds, gravity waves, Earth's rotation, orography and surface friction should be considered when providing numerical solutions to the equations.
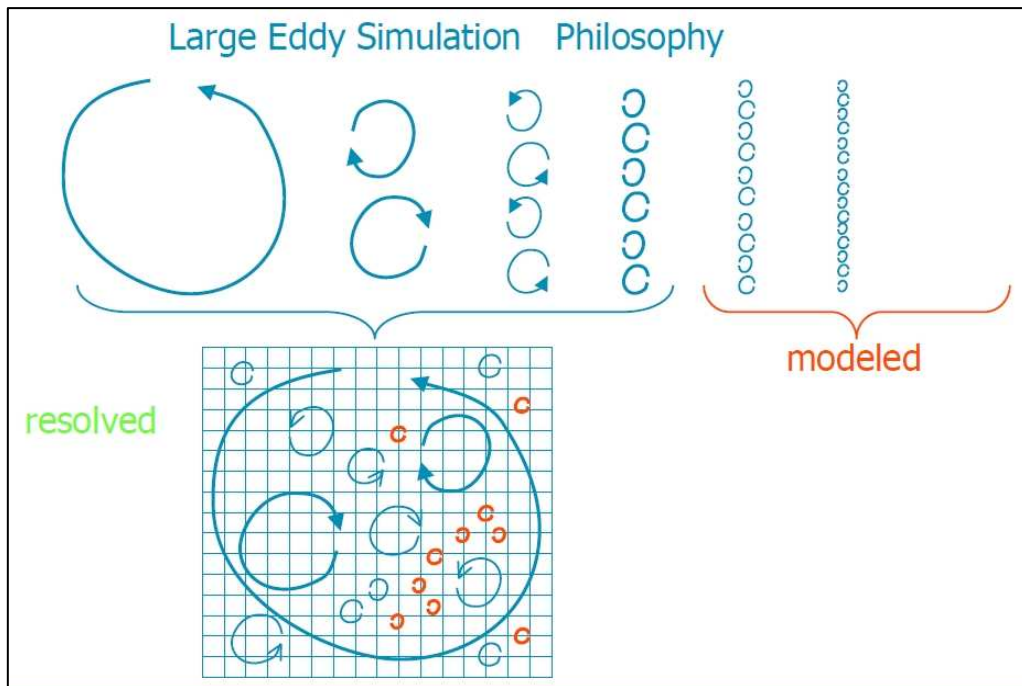
Figure 3.1. Large Eddy Simulation (LES) – large eddies are solved for while small eddies are filtered out and modelled (source: Harm Jonker, Delft University of Technology).

3.2.2. The LES NERSC Improved Code (LESNIC) and DATABASE64

Atmospheric turbulence is simulated by numerical modelling by making use of a turbulence-resolving simulation code called LESNIC (Esau, 2004) (Figure 3.2). It numerically solves the filtered Navier-Stokes equations of motions for incompressible Boussinesq fluid and the transport equations for the potential temperature and passive scalars. The LESNIC code has been used to compile a database of turbulence-resolving simulations, referred to as DATABASE64 (DB64) (Esau, 2004).

This database DB64 consists of a collection of LESNIC runs for a stably stratified planetary boundary layer (SBL) over a homogeneous aerodynamically rough surface (Esau, 2004). The runs simulate a period of 16 hours of PBL turbulence and produce three-dimensional fields of fluctuations of the potential temperature as well as three Cartesian components of the wind velocity, *u*, *v* and *w*. Turbulence statistics and horizontally time-averaged profiles of required quantities are obtained by further processing of the above mentioned fluctuations.
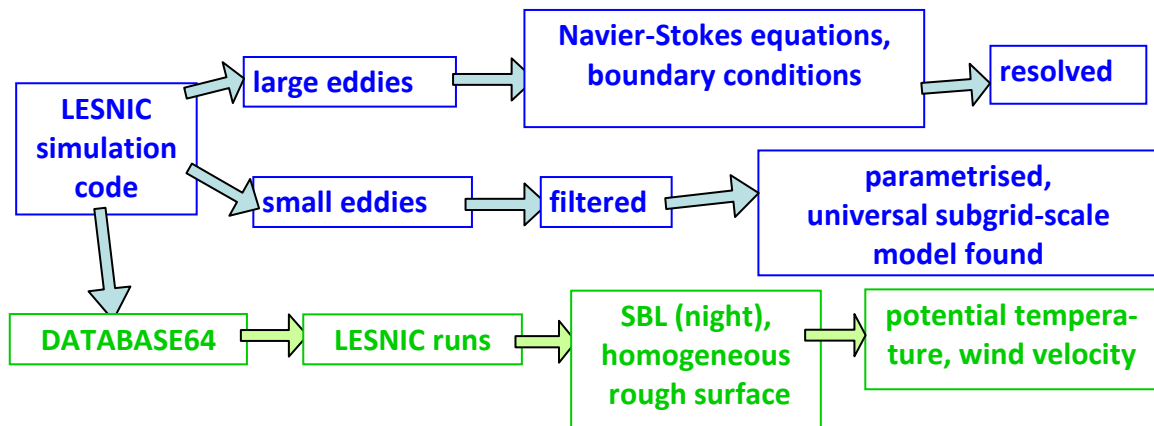
Figure 3.2. The LES NERSC Improved Code (LESNIC) provides a database of turbulence-resolving simulations, called DATABASE64.

3.2.3. Turbulence method – LESNIC modelling

Vertical profiles of $C_N^{\,2}(h)$ as well as the Fried parameter r_0 and seeing ε_{FWHM} were obtained by using LESNIC runs from DATABASE64 for a stably stratified planetary boundary layer (SBL) over a homogeneous aerodynamically rough surface. The LESNIC runs are controlled by external parameters. Control parameters which vary from run to run for the first 8 LES runs are the following:

- the physical size of the domain range between 100 and 500 m in each of the x, y and z directions;
- the model is run for 45, 70 or 90 degrees latitude;
- the surface roughness for momentum takes on one of the values: 0.03, 0.05, 0.07 or 0.1 m;
- surface heat flux takes on one of the values: -2, -3, -4, -5 or - 6 x 10^{-3} K.m.s^{-1};

- the Courant-Fridrihs-Levi (CFL) parameter used in calculating the time step is either 2.2 or 2.6.

The geostrophic wind was assigned a value of 3 or 5 m.s^{-1} as an initial value. There are 64 grid levels between 0 and 200 m. A temperature of 10 °C (= 283 K), pressure of 90500 mbar (= 905 hPa = 90500 Pa) and relative humidity of 70% were assigned to all runs.

$C_N^{\ 2}(h)$ profiles

Profiles of $C_N^{\ 2}(h)$ were obtained by making use of Equation (2.13) and data from the LESNIC DATABASE64. An Octave program (see Appendix A2) was written and used to calculate $C_N^{\ 2}(h)$ from the $C_T^{\ 2}(h)$ profile as well as temperature $T(h)$ and pressure $P(h)$ profiles as follows (Figure 3.3):

- The $C_T^{\ 2}$ parameter was determined from rates of temperature variance dissipation ε_θ and turbulence kinetic energy dissipation $\varepsilon^{-\frac{1}{3}}$ in accordance with (André et al., 1978)

$$C_T^{\ 2} = 1.6\,\varepsilon_\theta\,\varepsilon^{-\frac{1}{3}}, \tag{3.1}$$

where ε_θ and $\varepsilon^{-\frac{1}{3}}$ were provided by DATABASE64 for the specific run.

- Temperature $T(h)$ and pressure $P(h)$ profiles were determined by employing iteration to give

$$T_k(z_k) = T_{k-1} + \left(\left.\frac{d\theta}{dz}\right|_{z_{k-1}} + \gamma_{k-1}\right)\Delta z \tag{3.2a}$$

and

$$P_k(z_k) = P_{k-1} + \Delta P(T_k, r_{k-1}) = P_{k-1} - g\,\Delta z\,\rho = P_{k-1} - g\,\Delta z\,\frac{P_{k-1}}{R_{sd}T_{k-1}}, \tag{3.2b}$$

where

g :   gravitational acceleration = 9.8076 m.s^{-2} ;

ρ :   air density $= P_{k-1}/R_{sd}T_{k-1}$ [kg.m^{-3}];

R_{sd} :   specific gas constant of dry air = 287.052 J.kg^{-1}.K^{-1} .

- The gradient of the potential temperature $d\theta/dz$ and difference in level height Δz were provided by DATABASE64.

- The saturated adiabatic lapse rate γ is given by

$$\gamma = \frac{g \times \left(1 + \dfrac{H_v \times r}{R_{sd} \times T}\right)}{c_{pd} + \dfrac{H_v^2 \times r \times \varepsilon}{R_{sd} \times T^2}}, \tag{3.3a}$$

where

H_v : latent heat of vaporisation of water = 2.257 x 10^6 J.kg^{-1} ;

c_{pd} : specific heat of dry air at constant pressure = 1004 J.kg^{-1}.K^{-1} ;

ε : ratio of gas constants for dry air and water vapour = 0.622 ;

and where the actual mixing ratio r, which is the ratio of the mass of water vapour to the mass of dry air, was calculated from a provided relative humidity RH to give

$$r = \frac{RH}{100} \times x_s, \tag{3.3b}$$

with the saturation mixing ratio x_s given by

$$x_s = \frac{\varepsilon \, e_s}{P}, \tag{3.3c}$$

and the saturation vapour pressure e_s given by the Clausius-Clapeyron equation

$$e_s = 611 \, e^{\left[\frac{\varepsilon H_v}{R_{sd}}\left(\frac{1}{273} - \frac{1}{T}\right)\right]}. \tag{3.3d}$$

- Surface temperature T_1 and surface pressure P_1 were obtained from the base temperature T_{base} (= 283 K) and base pressure P_{base} (= 90500 Pa) at the site as given by

$$P_1 = P_{base} \tag{3.4a}$$

and

$$T_1 = T_{base} - \frac{\theta_*}{\kappa}\left(\log\frac{z_2}{2z_0} - \psi\left(\frac{z_2}{L_s}\right)\right), \tag{3.4b}$$

where

$$\psi\left(\frac{z_2}{L_s}\right) = 1 - 2.5\frac{z_2}{L_s}, \tag{3.4c}$$

and the following are given by DATABASE64:

surface temperature flux scale θ_*;
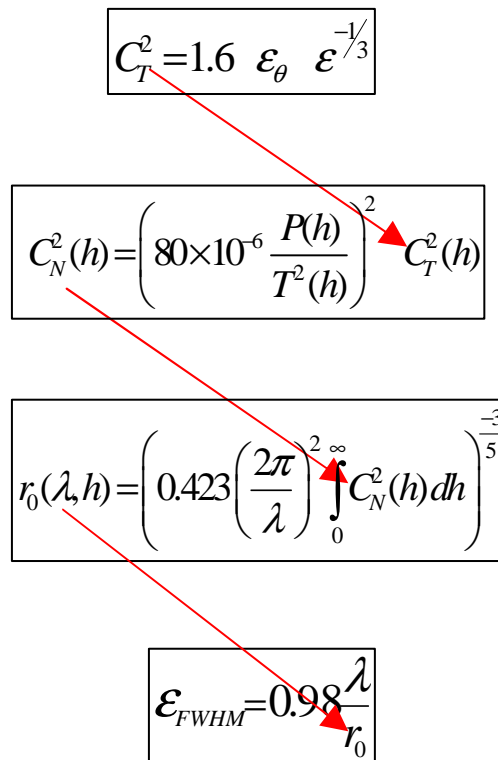
Von Karman constant $\kappa = 0.4$;

surface roughness length scale z_0;

and Monin-Obukhov length scale L_s.

Seeing parameter values

The Kolmogorov model of turbulence provides a statistical parameter (Fried parameter r_0) to characterise the seeing. The Fried parameter was obtained from Equation (2.20) by integrating $C_N{}^2(h)$ with respect to zenith. Seeing, as given by ε_{FWHM}, is related to the Fried parameter by Equation (2.19) and is therefore given by Equation (2.21) (Figure 3.3). A turbulence-resolving model is able to produce $C_N{}^2(h)$ profiles which may then be used to determine seeing at a site.

$$C_T^2 = 1.6 \ \varepsilon_\theta \ \varepsilon^{-1/3}$$

$$C_N^2(h) = \left(80\times10^{-6}\frac{P(h)}{T^2(h)}\right)^2 C_T^2(h)$$

$$r_0(\lambda,h) = \left(0.423\left(\frac{2\pi}{\lambda}\right)^2 \int_0^\infty C_N^2(h)\,dh\right)^{-\frac{3}{5}}$$

$$\varepsilon_{FWHM} = 0.98\frac{\lambda}{r_0}$$

Figure 3.3. Seeing from ε_θ, $\varepsilon^{-1/3}$, P and T from DATABASE64.

3.3.   Measuring seeing by optical method

Seeing may be quantified experimentally by comparison of ideal and observed images. Ideally, the response of an imaging system to incoming radiation from a point source would be described by the theoretical Airy function (Equation (2.14)) (Longair, 1992; Roggeman and Welsh, 1996 and Tubbs, 2003). In reality, however, the Airy function is broadened by poor seeing conditions and the response of the imaging system is described by the Point Spread Function (PSF). Seeing conditions captured by an optical seeing monitor setup can be measured by comparing the observed PSF with the theoretical Airy function. The optimal telescope and Charge-Coupled Device (CCD) camera combination to be used in a seeing monitor setup is determined by the resolution required and therefore by factors such as image scale, telescope focal length, camera pixel size and shape.

3.3.1. Point Spread Function (PSF)

Under ideal conditions, with no atmosphere present, the image of a point source is limited by diffraction effects only and is described by the theoretical Airy function (Equation (2.14)) (Longair, 1992 and Roggeman & Welsh, 1996). In reality, when imaging a point source, such as a star, the resulting image will not be a point, but will have spread out. This is due, not only to diffraction effects, but also to degradations of the electromagnetic wave front by turbulence in the atmosphere. Atmospheric turbulence distorts the image, and the distortions average out as a filled disc, called the PSF or seeing disc (Figure 3.4).

Figure 3.4. Example of a star's intensity profile or Point Spread Function (PSF) (source: Andrei Tokovinin, Cerro Tololo Inter-American Observatory (CTIO), Chile).
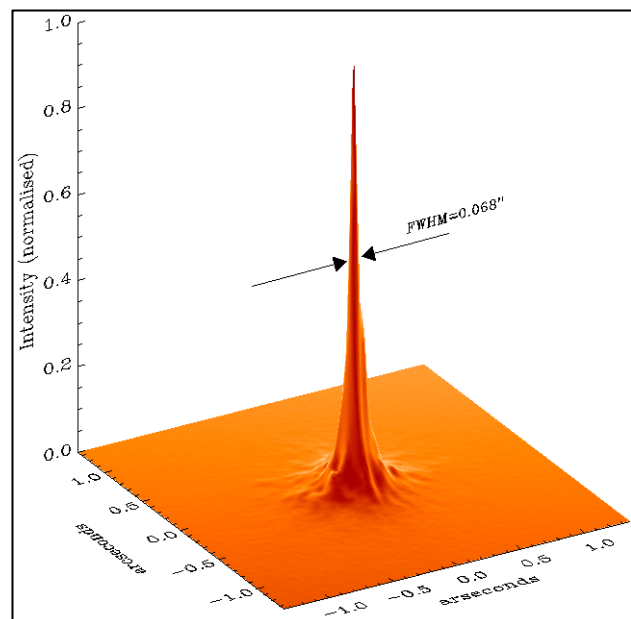
The PSF is used to characterise the imaging and provides the overall shape of the distribution of light which originates from a point source. It depicts where photons from a star have fallen, with the highest number of photons, the peak value, being accumulated in the central pixel in the profile. Aberrations and image motion broaden the PSF.

3.3.2. Image scale

The image scale gives the amount of sky covered by a single pixel of the CCD camera. It is dependent on the CCD camera's pixel size and the focal length of the telescope. The focal length of the telescope is the distance from the primary mirror or lens to the focal point where the light rays converge. Image scale is measured in arc-seconds per pixel according to the formula (Wodaski, 2002)

$$Image\ scale\ =\ \frac{205\ x\ CCD\ pixel\ size\ (\mu m)}{telescope\ focal\ length\ (mm)}. \tag{3.5}$$

Smaller pixel size and longer focal length give higher resolution images.

3.3.3. Sampling

Sampling refers to the number of pixels that a star image covers. If the image covers too few pixels, it is an under sampled image and the best possible resolution is not achieved. Critical sampling may be determined from the width of the PSF. For a Gaussian PSF, with the resolution measured across the diagonal of a square pixel, this corresponds to a critical sampling frequency of (Howell, 2006)

$$FWHM = \sqrt{2} \times 2.355 = 3.33\ pixels, \tag{3.6a}$$

where $FWHM$ is the full-width at half-maximum of the PSF (Figure 3.5). $FWHM$ is the diameter at which the star's intensity distribution falls to one-half of its peak value.

In order to obtain the required resolution of 1 arc-sec an image scale of less than

$$\frac{1\ arc\text{-}sec}{3.33\ pixels} = 0.3\ arc\text{-}sec\ per\ pixel \tag{3.6b}$$

is required.
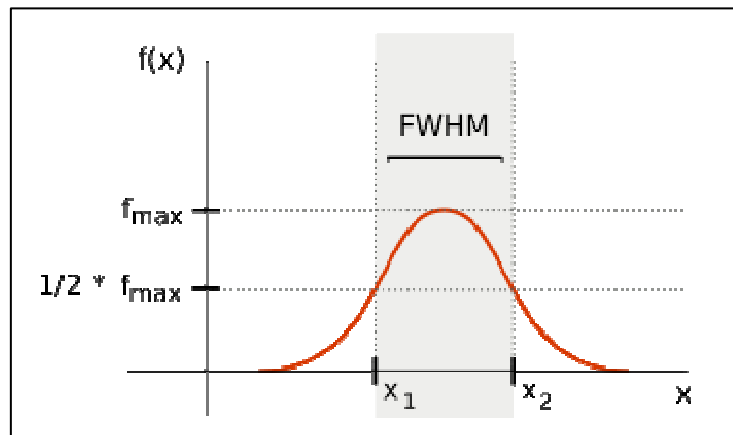
Figure 3.5. Full Width at Half Maximum (FWHM) of a Gaussian distribution (source: Arne Nordmann, Wikipedia).

3.3.4. Experimental method

Images captured by CCD were statistically analysed and compared with the theoretical Airy function, which is a measure of an absence of turbulence (Figure 3.6). Deviation from the Airy function gives an indication of seeing conditions. Close double stars were also observed for calibration and verification purposes.
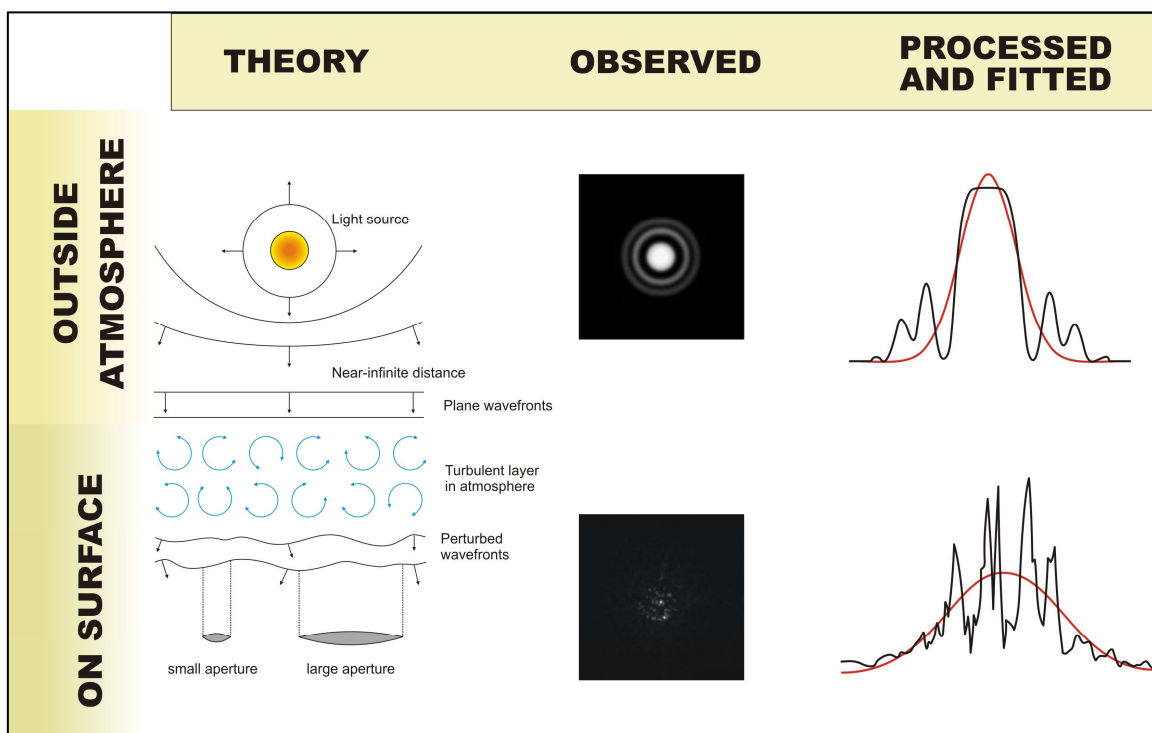
Figure 3.6. Diagrammatic representation of seeing analysis process (courtesy: Roelf Botha).

Image capture

Seeing varies spatially as well as temporally (Erasmus, 1986; Erasmus 2000 and Roddier, 1981). Seeing varies with elevation angle and is best at zenith. Seeing also changes with season, from night to night, with time of night and at a rate of more than 100 Hz. Usual terrain layouts are non-uniform and therefore have an influence on turbulence generation; seeing will be different for different classes of terrain.

Taking all this into account, we can deduce that for a site:

- stars at various positions on the night sky must be observed;
- observations must be made at different times;
- long-term data collection is required and
- observations must be made from various on-site locations.

Numerous short exposure images of a specific source were captured to allow for sampling of seeing variations and short-term image wander. Short exposure times eliminate telescope tracking errors (which contribute to image width) and allow for the "freezing" of atmospheric turbulence. Exposure times of 3 or 4 seconds allow for sampling of seeing variations and short-term image wander but are not influenced by bad tracking.

Image stacking and evaluation

The images were evaluated individually but could also be stacked to obtain an average output image of the star's intensity distribution, the PSF. Stacking was not implemented in this work. The PSF is broadened by poor seeing conditions (Longair, 1992; Roggeman and Welsh, 1996 and Tubbs, 2003). The broadened PSF was compared with the theoretical Airy function. A quantitative measure of the seeing was be obtained by fitting an appropriate function, a bell-shaped Gaussian intensity profile, to the PSF (Roddier, 1981) and determining the Gaussian profile's FWHM value.

The FWHM of a star's intensity distribution at the focus of the telescope describes the seeing ε_{FWHM}. This is related to the standard deviation from the Gaussian distribution σ by (Wargau, 1994)

$$\varepsilon_{FWHM} = FWHM = 2\sqrt{2 \ \ln 2} \ \sigma \approx 2.355 \ \sigma \qquad (3.7a)$$

in seconds of arc (number of FWHM pixels multiplied by image scale in arc-seconds per pixel). The Fried parameter r_0, as given by Equation (2.19), may be obtained from seeing observations through the relation

$$\varepsilon_{FWHM} \approx 2.355 \ \sigma = 206265 \left(0.98 \frac{\lambda}{r_0} \right), \tag{3.7b}$$

where λ is the wavelength of observation.

Measuring double star separation

Due to diffraction, the Airy disc represents the smallest point to which a light beam can be focused in accordance with the Rayleigh criterion of Equation (2.15). Similarly, the Dawes limit, as given by Equation (2.16), is applicable to resolving double stars, specifically a pair of white stars, each of magnitude 6 brightness (Napier-Munn, 2008). Dawes' limit represents the closest angular separation between two such stars with the stars still resolvable as separate objects, i.e. with the observer still being able to 'split the double'. If the two stars' Airy discs overlap, a single elongated star will be observed. If one star's Airy disc falls in the first dark diffraction ring of the other star, the two stars will be observed as two small disks forming a figure of eight (Figure 3.7).
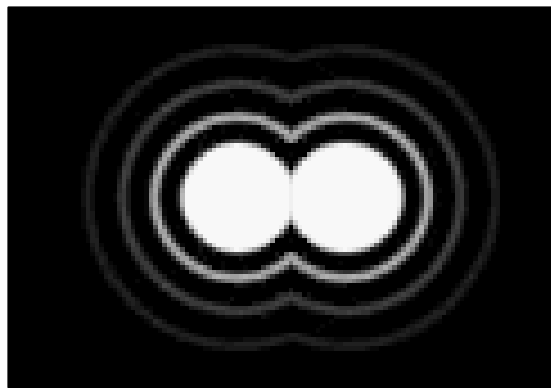
Figure 3.7. Binary stars: overlapping Airy discs (source: The Royal Astronomical Society of Canada, Calgary Centre).

Successively closer double stars will be observed until a limit is reached where a pair can no longer be resolved. The achieved resolution limit will be compared with the telescope's theoretical resolution limit (according to the Rayleigh criterion and Dawes' limit) in order to determine seeing conditions.

4. Seeing monitor – proposed design

4.1. Introduction

An investigation into suitable hardware components for the seeing monitor is detailed in this chapter. A possible seeing monitor setup is proposed. Astronomical seeing conditions conducive to the propagation of the LLR's laser beam are those for which the seeing is at better than arc-second resolution level. The seeing monitor setup must therefore be capable of a theoretical resolution of better than an arc-second not to be the limiting factor for image quality during astronomical seeing measurements. The proposed system is to consist of a telescope, CCD camera and control/processing PC. The seeing monitor's requirements with respect to the telescope mount, automation and infrastructure will also be discussed. Instrumentation that should be co-hosted on-site in support of seeing measurements with the seeing monitor setup, as well as in support of LESNIC modeling, are briefly mentioned (with a more thorough description of such instruments given in the Appendix A4).

4.2. Hardware requirements

The optimal combination of telescope and CCD camera must deliver a theoretical resolution of better than 1 arc-second if it is to measure whether seeing below 1 arc-second is possible at a site. For an image not to be under sampled, a critical sampling frequency of 3.33 pixels is required according to Equation (3.6a), which means that the star image must cover at least 3.33 pixels of the CCD sensor. According to Equation (3.6b), to achieve a resolution of better than 1 arc-second and a critical sampling frequency of at least 3.33 pixels, an image scale of less than 0.3 arc-second per pixel is required. Equation (3.5) was used to compile the graph in Figure 4.1. The graph depicts the Field Of View (FOV) per pixel, i.e. the image scale, resulting from various telescope aperture and focal ratio sizes in combination with various CCD sensor pixel sizes. It can be deduced from this graph that the larger the telescope's aperture and the higher its focal ratio and the smaller the CCD sensor's pixel size, the better the resolution achieved.
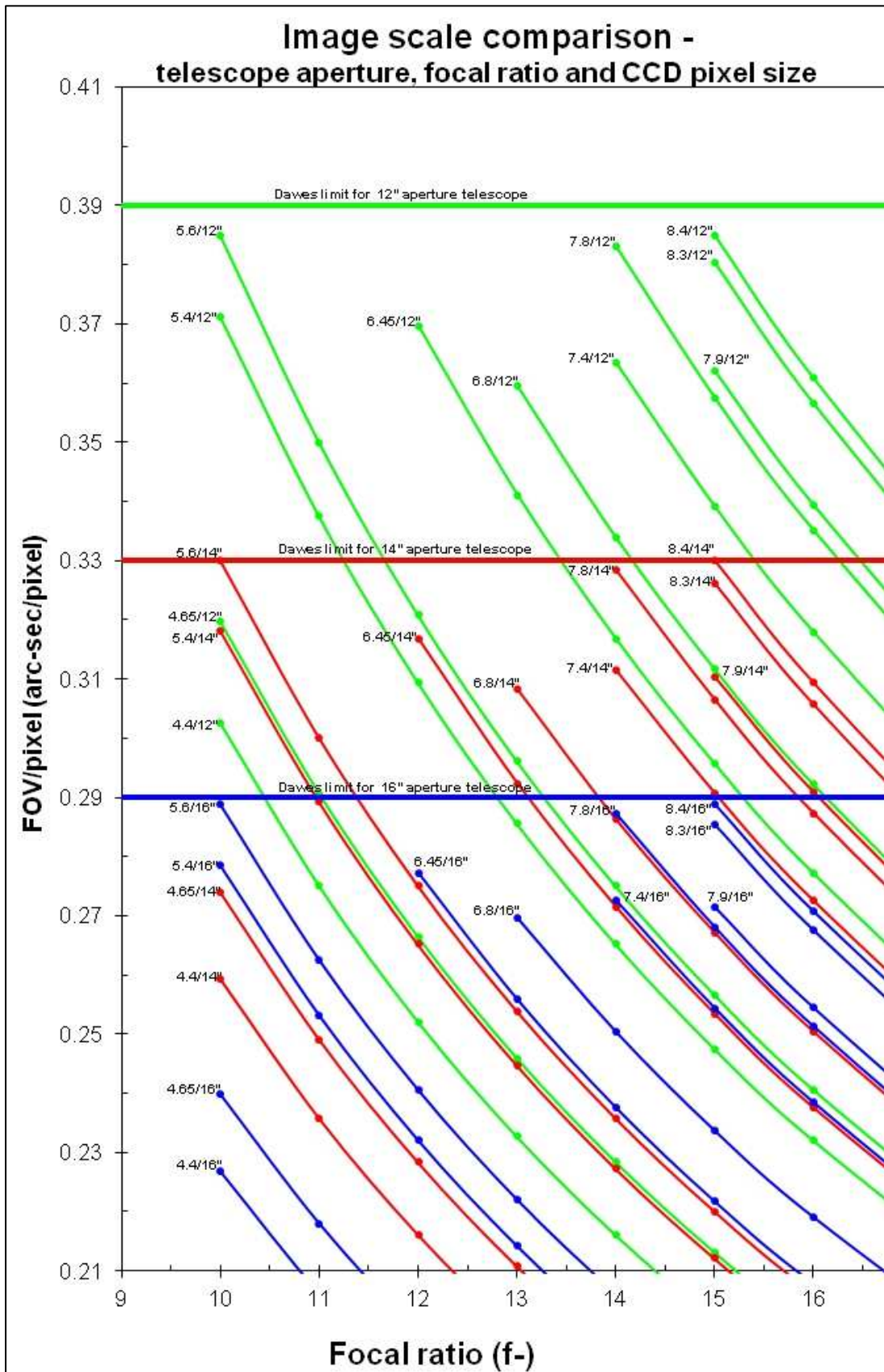
Figure 4.1. Graph depicting possible telescope and camera combinations.

CCD sensor pixel size will be chosen in accordance with a predetermined telescope diameter and focal length, with the combination comparable to Airy disc size to fully utilise the capabilities of the optics. A suitable mount, which is able to accommodate the weight and dimensions of the Optical Tube Assembly (OTA) of the telescope and all its attachments, in particular the CCD camera, must be found for the required imaging resolution to be achievable.

4.2.1. Telescope

The following discussion is based on information obtained from Mobberley (1998), Starizona (2000) and Wodaski (2002). According to Equation (3.5), the image scale depends on both the focal length of the telescope and the size of the pixels in the camera sensor. Long focal lengths and small pixels result in a smaller image scale and therefore higher resolution. The focal length of a telescope is given by

$$FL = D \times f\text{-}ratio ,\tag{4.1}$$

where FL is the focal length in mm, D the aperture diameter in mm and the $f\text{-}ratio$ is the focal ratio, which is a dimensionless quantity. For a given aperture diameter, the higher (longer, slower) the focal ratio the longer the focal length of the telescope and therefore the smaller the image scale for a specific CCD sensor pixel size.

Regarding the choice of the telescope OTA then, for the best resolution, the largest aperture telescope with the highest focal ratio is required. This was the primary requirement in choosing the most suitable telescope. Further requirements with regard to excellence of optical quality, GOTO functionality (for easy automation), sturdiness of the mount and portability of the setup were also considered.

4.2.2. CCD camera

The following discussion is based on information obtained from Martinez and Klotz (1998) as well as Howell (2006). A CCD camera is a detector which makes use of the photo-electric effect to convert incoming photons to electrons at photo-sensitive sites known as pixels. The electronic charge is transferred during readout. Voltage is converted to a digital

signal to produce a digitised image. Definitions of terms describing CCD camera characteristics are provided in Appendix A3.

In comparing various CCD camera models (in effect the CCD chips), although the primary consideration was to find an ideal match between CCD pixel size and telescope focal length, other CCD camera specifications that were also considered are as follows:

Monochrome / colour - due to higher sensitivity, a monochrome CCD camera is required.

Number of pixels in array - with relatively small pixel size, a large number of pixels in the pixel array is required to ensure a FOV wide enough to avoid difficulties with centring and focusing of the star image.

Full frame / frame transfer / interline - a full-frame CCD camera is preferred over frame transfer or interline CCD cameras, as sensitivity is compromised in the latter two types due to their mode of charge transfer and readout.

Readout rate / frame rate / minimum exposure length - to capture turbulence fluctuating at 100 - 200 Hz, high readout and maximum frame rates as well as the shortest possible minimum exposure length are required.

Dimensions / weight - the CCD camera's dimensions and weight should be as small as possible to allow for problem-free mount-clearance and as little weight as possible to be added to the payload.

Interface / transfer rate - computer connectivity should be established by means of a USB 2.0 or Firewire (IEEE1394) PC interface and high transfer rates are required.

Digital resolution - a digital resolution with at least 14-bit Analogue to Digital (A/D) conversion for full use of a high Dynamic Range (large Full-Well Capacity, low Read Noise) is required.

Operating temperature - the CCD camera should be able to operate at a range of temperatures from below 0 °C to above 30 °C with regulated cooling to reduce Dark Current.

Power consumption - low power consumption requirements are necessary as power will be supplied by battery charged by solar panel.

4.2.3. Mount

The following discussion is based on information obtained from Mobberley (1998), Starizona (2000) and Wodaski (2002). For commercially available telescopes, the OTA and mount, together with the drive system, are oftentimes sold as a pre-assembled package. The mount is the determining factor for long focal-length, high-resolution astronomical imaging. A quality mount is required for CCD imaging. It must be sturdy enough to support a heavy load without any flexure and must be able to damp any vibrations quickly. The mount together with its drive motors must track accurately and any gearing must have very low backlash.

The two basic telescope mount designs are the alt-az and equatorial mounts. The SCTs sold with computerised alt-az fork mounts and German Equatorial Mounts (GEM) are popular for use in CCD imaging. These GOTO mounts have on-board computers for locating stars and commanding drive motors to point the telescope at and track these stars across the sky. The more stable the mount, the greater the pointing accuracy and tracking precision. To follow, a short summary of the strengths and weaknesses of these two types of mount:

Fork mount

Commercial fork mounts tend to be mechanically unstable. This type of mount also has limited space between the back of the telescope, where the CCD camera is attached, and the base of the fork. Large CCD cameras will therefore not be able to clear the base of the fork when the telescope is pointing at declinations near zenith. Fork-mounted telescopes can, however, cross the meridian without any problem. Variable-rate motors on both axes are controlled by computer and allow the telescope to track the desired star. Field rotation must be corrected for by the addition of a de-rotator. By attaching an equatorial wedge between the fork mount and telescope, the fork mount is transformed into an equatorial mount. Stars can then be tracked with a constant-speed motor on the polar axis and field rotation does not occur.

German Equatorial Mount (GEM)

This type of mount has a short fulcrum and delivers the best mechanical stability. It is also capable of carrying more load than a fork mount and is easier to balance. The mount has two axes of rotation and can point a telescope anywhere in the sky. A motor turns the mount on the axis which is aligned with the celestial pole (Right Ascension, (RA)), which enables it to track at the sidereal rate. The Declination (Dec) axis moves at right angles to the RA axis. With a GEM, the CCD camera or even the telescope can strike the pier when crossing the meridian. A telescope with a GEM must therefore be flipped from the western to the eastern side of the mount before crossing the meridian. This will interrupt imaging and may affect accuracy during the remainder of the observing session.

4.3. Hardware selection

4.3.1. Telescope

The following discussion is based on information obtained from Mobberley (1998), Starizona (2000) and Wodaski (2002). To follow, a short description of the basic telescope optics used in the design of telescope Optical Tube Assemblies (OTAs):

- Refracting telescopes make use of an objective lens to bring the starlight to a focus at the back of the telescope.
- Prime focus reflecting telescopes make use of a paraboloidal primary mirror to reflect light back to a detector at prime focus.
- Newtonian reflecting telescopes consist of a paraboloidal primary mirror, which reflects starlight onto a flat secondary mirror, tilted at 45° to reflect the light onto the detector at the side of the telescope.
- Cassegrain reflecting telescopes use a paraboloidal primary mirror to reflect starlight onto a hyperboloidal secondary mirror, which then reflects the lights back through a hole in the centre of the primary mirror and out to the detector.

Different types of commercially available telescope OTA designs were compared (Table 4.1). The various designs all include the required large aperture diameter telescopes

Table 4.1. Comparison of commercially available telescope Optical Tube Assemblies (OTAs).

Telescope design	Refractors	Reflectors – Newtonian / Dobsonian	Schmidt-Cassegrain (SCT)	Maksutov-Cassegrain	Classical Cassegrain	Ritchey-Chrétien (RC)
Types	Achromatic (AC) Apochromatic (APO)	Dobsonians (Dobs) Schmidt-Newtonians (S-N) Maksutov-Newtonian (M-N)				
Aperture diameter	2"-14"	Dobs: 3"-17.5" Newts: 3"-16"	3.5"-20"	4"-13"	10"-16"	6"-23.6"
Focal length	324-4272 mm	Dobs: 300-2225 mm Newts: 600-2436 mm	1034 - 4064 mm	1251-4290 mm	3810-6090 mm	1372-4800 mm
Focal ratio	f/5-f/15	Dobs: f/3.95-f/9 Newts: f/3.6-f/9.75	f/8-f/13.8	f/11.5-f/13.9	f/12 – f/20	f/5.4– f/9
Aberrations	AC: chromatic	Coma M-N: Maksutov corrector lens for coma S-N: Schmidt corrector for spherical aberration	Schmidt corrector lens for spherical aberration; aspheric secondary mirror for coma	Maksutov corrector lens for spherical aberration; aspheric secondary mirror for coma	Coma Field curvature	Field correctors for residual astigmatism
Optical quality	APO: excellent	M-N: excellent				Very good
Imaging	Short f-ratios popular for wide-field; large APOs for high-resolution		Wide-field & high-resolution		Mostly high-resolution	Mostly high-resolution
OTA – dimensions and weight	280-2280 mm 0.38–100? kg	Dobs: 457-2235 mm 1.8-59.88 kg Newts: 400-2438 mm 1.6-50 kg	279-1016 mm 2.1-87 kg	254-933 mm 1.4-19.8 kg	1016-1677 mm 18.2-59 kg	457-1790 mm 5.9-115 kg
Mounts	Depends on OTA dimension, weight	Depends on OTA dimensions, weight	Small, computer-controlled			
Portability	Less portable than SCTs of same aperture	Less portable than SCTs of same aperture	Compact	Compact	Reasonably compact	Compact

in their range. Newtonian/Dobsonian reflectors as well as Ritchey-Chrétien (RC) telescopes, however, do not meet the requirement of a high focal ratio. The seeing monitor requires a telescope that is compact and portable for field work. Large-aperture

Newtonian/Dobsonian reflectors and refractors are large and unwieldy instruments compared to Cassegrain telescopes of similar aperture and are not very portable. Classical Cassegrain telescopes have longer tubes than Schmidt-Cassegrain and Maksutov-Cassegrain telescopes of similar aperture. Maksutov-Cassegrain and classical Cassegrain telescopes with the required large apertures and high focal ratios are not readily available. The choice thus fell on the commercially available Schmidt-Cassegrain telescopes (SCTs).

Commercially available SCTs have focal ratios of f/10. These telescopes are popular for CCD imaging as they are versatile, providing for both high-resolution and wide-field imaging. Spherical aberration is minimised by employing a Schmidt corrector lens. Coma may be eliminated by employing an aspheric secondary mirror. A secondary mirror is employed to pack a longer focal length into a shorter tube. This folded optical design delivers a compact, light-weight telescope requiring a smaller mount, which adds to portability. Some of the commercially available SCTs include a computer-controlled mount with GOTO functionality. The telescope is easy to set up and use and provides easy access for a CCD camera. By the Dawes limit of Equation (2.16) and as indicated in Table 4.2, only telescopes with aperture diameters of 14" and above are capable of delivering a theoretical resolution of ~ 0.3 arc-sec. A second-hand 14" Meade LX200 GPS SCT with a computer-controlled heavy-duty altitude azimuth (alt-az) fork-type mount was purchased (Figure 4.2).

Figure 4.2. Recently acquired second-hand 14" Meade LX200 GPS SCT with alt-az fork-arm mount and field tripod.

4.3.2. CCD camera

The commercially available SCTs have relatively short focal ratios of f/10. Although the focal length of a telescope may be increased by inserting a Barlow lens into the optical path, this would just add another optical component to the light path and flaws may be magnified. It would be preferable to match aperture diameter and f-ratio (in other words focal length, see Equation (3.5) and Equation (4.1)) with CCD pixel size to deliver the required FOV of ~ 0.3 arc-sec per pixel (in accordance with Equation (3.6b)). A focal ratio of f/10 and aperture diameter of 14" therefore limited possible combinations to those with CCD cameras with sensor pixel sizes of 4.4, 4.65, 5.4 or 5.5 µm at most. Popular commercially available CCD cameras in this pixel-size range are listed in Table 4.2.

Table 4.2. Dawes' limit (red) for specific telescope aperture sizes and FOV/pixel for various CCD camera / telescope aperture combinations. Focal ratio of telescope under consideration is f/10 in all cases.

CCD camera	Pixel size	# Pixels		Telescope aperture (f/10)				
	[square sides]			25 cm	27.5 cm	30 cm	35 cm	40 cm
	µm			10"	11"	12"	14"	16"
Dawes' limit = 11.6/D (cm)				**0.46**	**0.41**	**0.38**	**0.32**	**0.28**
						FOV/pixel (arc-sec/pixel)		
Point Grey GRAS-20S4M	4.4	1624	1224	0.36	0.30	0.30	0.26	0.23
ATIK 320E	4.4	1620	1220	0.36	0.30	0.30	0.26	0.23
IS DMK 51	4.4	1600	1200	0.36	0.30	0.30	0.26	0.23
Lumenera SKYnyx2-2	4.4	1616	1232	0.36	0.30	0.30	0.26	0.23
Apogee Ascent A205	4.65	1360	1024	0.38	0.35	0.32	0.27	0.24
ATIK 314E	4.65	1360	1024	0.38	0.35	0.32	0.27	0.24
FLI MLx205	4.65	1360	1024	0.38	0.35	0.32	0.27	0.24
IS DMK 41	4.65	1280	960	0.38	0.35	0.32	0.27	0.24
Lumenera SKYnyx2-1	4.65	1392	1040	0.38	0.35	0.32	0.27	0.24
IS DMK 31	4.65	1024	768	0.38	0.35	0.32	0.27	0.24
Apogee Alta U8300	5.4	3326	2504	0.45	0.41	0.37	0.32	0.28
ATIK 383L+	5.4	3326	2504	0.45	0.41	0.37	0.32	0.28
FLI ML8300M	5.4	3326	2504	0.45	0.41	0.37	0.32	0.28
Orion Parsec 8300M	5.4	3326	2504	0.45	0.41	0.37	0.32	0.28
QSI 5/683S	5.4	3326	2504	0.45	0.41	0.37	0.32	0.28
SBIG ST/STF8300M	5.4	3326	2504	0.45	0.41	0.37	0.32	0.28
Apogee Ascent A1050	5.5	1024	1024	0.45	0.41	0.37	0.32	0.28
FLI ML01050	5.5	1024	1024	0.45	0.41	0.37	0.32	0.28
Apogee Ascent A2050	5.5	1600	1200	0.45	0.41	0.37	0.32	0.28
Apogee Ascent A2150	5.5	1920	1020	0.45	0.41	0.37	0.32	0.28
Apogee Ascent A4050	5.5	2336	1752	0.45	0.41	0.37	0.32	0.28
Apogee Ascent A8050	5.5	3296	2472	0.45	0.41	0.37	0.32	0.28
FLI ML8050	5.5	3296	2472	0.45	0.41	0.37	0.32	0.28
Apogee Acent A29050	5.5	6576	4384	0.45	0.41	0.37	0.32	0.28
FLI ML29050	5.5	6600	4408	0.45	0.41	0.37	0.32	0.28
Point Grey GRAS-03K2M	7.4	640	480	0.61	0.55	0.51	0.43	0.38

In Table 4.3, CCD cameras in the 4.4- to 5.5-µm range (listed in Table 4.2) were compared with respect to the specifications referred to in Section 4.2.2.

Table 4.3. Comparison of CCD cameras appearing in Table 4.2 according to the specifications discussed.

CCD camera	Advantages	Disadvantages
Apogee Ascent	Some models - large number of pixels in array... Some models - high frame rate 16-bit ADC OS: W/L/M	… but slow frame rates Expensive to very expensive CCD type: IL Large body
Apogee Alta	KAF-8300 FF chip with mechanical shutter Large number of pixels in array 16-bit ADC Large FWC	Expensive Min t_{exp} = 30 ms Large, heavy body Max T_{op} = 27 °C
ATIK 320E & 314E	16-bit ADC Light in weight	CCD type: IL Large body
ATIK 383L+	KAF-8300 FF chip with mechanical shutter Large number of pixels in array 16-bit ADC Large FWC	Min t_{exp} = 200 ms Large body High power requirements
FLI	Some models - large number of pixels in array... 16-bit ADC Most models - wide range of T_{op}	… and slow frame rates Very expensive CCD type: IL
FLI ML8300M	KAF-8300 FF chip with mechanical shutter Large number of pixels in array 16-bit ADC Wide range of T_{op} Large FWC	Expensive Min t_{exp} > 6 ms Large body
IS DMK	Inexpensive Some models - high frame rate … Small, light body USB 2.0 / Firewire / GigE Max T_{op} = 45°C Low power requirements	CCD type: IL … but small number of pixels in array 8-bit ADC Min T_{op} = -5 °C Min t_{exp} > 6 ms
Lumenera SKYnyx	Light body Max T_{op} = 50°C Low power requirements	Expensive Low frame rate 8- & 12-bit ADC
Orion Parsec 8300M	KAF-8300 FF chip with mechanical shutter Large number of pixels in array 16-bit ADC Large FWC	Min t_{exp} = 6 ms Heavy body High power requirements
QSI 5/683S	KAF-8300 FF chip with mechanical shutter Large number of pixels in array 16-bit ADC Large FWC Min T_{op} = -20 °C OS: W/L/M	Expensive Min t_{exp} = 30 ms Large, heavy body Max T_{op} = 30 °C High power requirements
Point Grey GRAS-20S4M (for PSF seeing monitor)	Min t_{exp} = 0.02 ms Small, light body Firewire Max T_{op} = 40 °C Low power requirements OS: L/M	CCD type: IL Min T_{op} = 0 °C
SBIG ST/STF8300M	KAF-8300 FF chip with mechanical shutter Large number of pixels in array 16-bit ADC Large FWC OS: W/L/M	Min t_{exp} = 100 ms Large, heavy body High power requirements
IL=Interline; FOV=Field Of View; T_{op}=operating Temperature ; ADC=Analogue-to-Digital Conversion; OS=Operating System; W=Windows; L=Linux; M=Mac; FWC=Full-Well Capacity; FF=Full-Frame; t_{exp} = exposure time		

The initial decision was to select from CCD cameras containing the Kodak KAF-8300 chip (5.4-μm pixel size, see Table 4.2). From the initial selection appearing in Table 4.2, these cameras are the only full-frame CCD cameras with mechanical shutters. The decision changed once Tim Pickering of SAAO placed the software of the DIMM component of their SALT MASS-DIMM at our disposal. Setting up a DIMM configuration would simply equate to placing a two-hole mask at the telescope's entrance aperture, a prism at one of the two small sub-apertures, and a high-speed CCD camera at the back of the telescope. The SALT DIMM software, TimDIMM, supports an IEEE1394 Firewire CCD camera, the Point Grey Grasshopper GRAS-03K2M (highlighted in blue at the bottom of Table 4.2) and runs on a Mac mini under OS X. The TimDIMM software could also be adapted to run under Linux but would require the IEEE1394 interface to be in at an added expense, while this interface is already built into the Mac mini. It was therefore decided to acquire the Point Grey Grasshopper GRAS-03K2M-C CCD camera (Figure 4.3), together with a Mac mini, in order to set up a DIMM in addition to our self-built PSF seeing monitor.

Figure 4.3. The Point Grey Grasshopper GRAS-03K2M (for DIMM measurements) and GRAS-20S4M (for PSF seeing monitor measurements) CCD cameras.

Although the GRAS-03K2M, an interline-type CCD camera, has a very high frame rate of 200 frames per second (fps), it possesses a small number of pixels in its pixel array and would therefore not provide a sufficient FOV for the purposes of the PSF seeing monitor. In order to accommodate the IEEE1394 Firewire and Mac mini requirements of the DIMM setup, it was decided to compromise with respect to CCD type for the PSF seeing monitor and acquire an interline-type CCD camera, the Point Grey Grasshopper GRAS-20S4M (highlighted in green at the top of Table 4.2, also shown in Figure 4.3), which provides a larger number of pixels and a reasonably high frame rate of 30 fps.

A webcam, the Philips ToUcam Pro II PCVC840K (Figure 4.4), a colour camera with a high frame rate but a small number of pixels in its pixel array, was acquired previously to be used in an initial binary star observation test setup for the PSF seeing monitor (Figure 4.5). Webcams allow for very short exposure times. It would be possible to modify the ToUcam to become a monochrome camera by replacing its colour chip, the SONY ICX098BQ, with the black and white version thereof, the SONY ICX098BL. An Orion StarShoot USB Live View Value Kit (Figure 4.6) was acquired to assist in centering and focusing of the star image. It includes a flip mirror to visually find, center and focus the star image as well as a StarShoot USB eyepiece which transmits the image to the laptop.

Figure 4.4. The Philips ToUcam Pro II PCVC840K webcam with lens removed and replaced by MOGG adapter.

Figure 4.5. Test setup for double star observation – 10" Meade LX200 SCT, ToUcam webcam and laptop.

Figure 4.6. The Orion StarShoot USB Live View Value Kit with imaging flip mirror and StarShoot USB eyepiece.

4.3.3. Mount

The 14" Meade LX200 GPS SCT that was acquired comes with an alt-az fork-arm mount. Although fork-arm mounts are not ideal for imaging, the intention is to test the image quality delivered by this telescope with its heavy-duty alt-az fork-arm mount and field tripod before purchasing a high-quality GEM. As described previously, by fitting an equatorial wedge, the fork mount can be turned into a polar mount, eliminating field rotation. The short exposure images required by the PSF seeing monitor should eliminate telescope tracking errors and preclude the need for a field de-rotator, auto-guider or an equatorial mount. If the experience of the South African Astronomical Observatory (SAAO) South African Large Telescope (SALT) Site Monitoring Team with their MASS (Multi-Aperture Scintillation Sensor) - DIMM (Differential Image Motion Monitor) 10" Meade LX200 SCT on an alt-az fork-arm mount is anything to go by, however, an equatorial mount with guiding is more or less mandatory for DIMM imaging. At first, they used an equatorial wedge to turn their alt-az mount into a polar mount. During system automation, problems were encountered with computer controlled guiding and slewing using the Meade Autostar II control system. They replaced the mount with an A-P 900GTO mount, which provided much improved tracking in automated mode.

Even a mechanically, electrically and electronically sound mount will still suffer from wind buffeting (Starizona, 2000). A polar mount with guiding is therefore more or less mandatory for CCD imaging. High-quality telescope mounts such as those made by Astro-Physics and Software Bisque are known for rigidity, high pointing accuracy, smooth and accurate tracking as well as advanced GOTO capability and computer interfacing. A selection of commercially available GE mounts identified as being of sufficient quality for seeing monitor requirements is presented in Table 4.4.

The Astro-Physics (A-P) 900GTO and 1600GTO and Software Bisque (SB) Paramount MX are top quality mounts. The Losmandy HGM Titan mount is of slightly higher quality than the Celestron CGE Pro and Meade LX800 GE mounts, the latter being a recent addition of a GEM to the Meade brand of mostly fork-arm mounts. All the mounts come with mount calibration and modelling circuits or specialised software for Periodic Error Correction (PEC) to improve polar alignment and pointing precision etc. The Meade

LX800 GE additionally offers StarLock, which makes use of two auto-guiding cameras to refine the pointing and assist with alignment, target acquisition and guiding corrections.

Table 4.4. Comparison of telescope mounts.

Mount	Astro-Physics		Software Bisque	Meade	Losmandy	Celestron
Model	1600GTO	900GTO	Paramount MX	LX800 GEM	HGM Titan	CGE Pro
Instrument payload	90 kg	31 kg	40 kg	40 kg	45 kg	40 kg
Counterweights incl.	No	No	2x 9 kg	8 kg	2x 9.5 kg	10 kg
SCT apertures	> 18"	> 12"	> 14"	> 14"	>14"	>14"
Price	$11700	$8750	$8995	$7299	$5995	$4999
Imaging past meridian	Well past	Well past	2 h	20 deg	?	20 deg
Latitude range	0° - 78°	20° - 68°	10° - 65°	?	12° - 70°	10° - 65°
Pointing accuracy	< 1'	< 1'	30"	1'	1'-2'	1'
Periodic Error (PE)	5"	7"	7"	?	5"	3"
PE Correction (PEC)	PEMPro	PEMPro	1", TPoint	1", StarLock	< 2"	PPEC
Control software	PulseGuide	PulseGuide	MKS5000	AustoStar II	Gemini 2	NexRemote
Power requirements	12 V / 5 A	12 V / 5 A		12 V / 5 A	12 V / 3 A	12 V / 3.5 A
Servo drive system	DC	DC	DC	DC	DC	DC
Mount weight	52.5 kg	24.5 kg	23 kg	35 kg	34 kg	34 kg
Tripod incl.	No	No	No	Yes	No	Yes

In choosing the most appropriate mount from the selection of GEMs, the mount's payload capacity should be matched to the weight of the instrument payload it would be expected to carry. The instrument payload currently anticipated is as follows:

- Meade LX200 14" GPS SCT of 27 kg;
- finder scope of < 1 kg;
- Point Grey GRAS-20S4M-C CCD camera of 104 g;
- Point Grey GRAS-03K2M-C CCD camera of 104 g;
- PhilipsToUcam PCVC840K webcam of 100 g;
- Orion StarShoot USB Live View Value Kit of < 1 kg;
- DIMM mask and prism of < 1 kg;
- instrument mounting interfaces and adapter plates of < 2 kg
- and instrument housing of < 1 kg,

therefore requiring a mount with a payload capacity of less than 35 kg.

However, the generally accepted view is that, for imaging purposes, a mount should carry far below its rated payload. The A-P 900GTO has a recommended SCT aperture diameter of 12" and a rated payload capacity of only 31 kg, which excludes it from further consideration. The SB Paramount MX, Celestron CGE Pro and Meade LX800 GEMs with payload capacities of 40 kg appear to be borderline cases, while the Losmandy HGM Titan with its payload capacity of 45 kg is able to handle only a few additional kilograms. Considering instrument capacity alone, the A-P 1600GTO is the only mount that meets the requirement of being able to carry well below its rated payload.

4.4. Software and automation

Once the final location of the seeing monitor has been decided, the system must be able to operate autonomously. A robotic system will be put in place with the master control system controlling the entire observatory – operation of the telescope, CCD camera, enclosure as well as the processing and communications computer. Observatory automation software allowing for automated control and remote monitoring of the observatory will have to be developed. The following tasks must be performed autonomously:

- the mount must be able to point the telescope with high accuracy towards the star and allow the telescope to accurately track;
- exact focus must be achieved;
- the CCD camera must be able to complete an entire acquisition session successfully;
- images must be processed and evaluated;
- seeing monitor measurements must be made available;
- the mount, CCD camera and computer must be turned on/off;
- the telescope must be parked;
- air conditioning units and ventilation fans must be controlled;
- the roof of the telescope enclosure needs to close automatically in the event of imminent bad weather;
- the status of weather and observatory conditions must be reported.

The master control system must control and integrate the functioning of all these subsystems and tasks without the necessity for human intervention and must therefore be flexible and robust.

4.5.   Logistical issues

During the initial phase, a portable seeing monitor setup will be used to measure seeing conditions at various locations on-site. Once the location offering the best seeing conditions has been determined, a seeing monitor observatory will be established at this location, in close proximity to the LLR.

An access road, water, electricity and communications will be available at the location of the LLR but will be lacking for the various on-site locations during the initial monitoring of seeing conditions. Rough terrain will have to be traversed to reach these locations on ridges and koppies, requiring the use of an off-road vehicle and a very portable seeing monitor. The portable seeing monitor will not require access to water as there will be no cooling systems involved. A means of communication will also not be required for the relatively short seeing campaigns at the various on-site locations as all data will be stored to a laptop computer. Solar power will be required to provide electricity for the seeing monitor and a laptop computer.

Stable piers will have to be erected on which to mount the portable seeing monitor at the various on-site locations. The portable seeing monitor will be well-protected from wind by screens and from rain by a waterproof covering. The observatory seeing monitor will be housed in an enclosure built in close proximity to the LLR but as far as possible from local sources of bad seeing. This enclosure will consist of either a building with a roll-off roof or a motorised canvas clamshell dome (Figure 4.7). A stable platform isolated from vibrations will be erected so that the seeing monitor may operate from the same height above ground level as the LLR telescope (Figure 4.8).

Figure 4.7. The Cerro Tololo Inter-American Observatory (CTIO) Robo-DIMM in Chile with motorised canvas clamshell enclosure (source: CTIO).

Figure 4.8. The Isaac Newton Group of Telescopes (ING) – Instituto de Astrofísica de Canarias (IAC) RoboDIMM with Astro Haven fibreglass clamshell at the Observatorio del Roque de los Muchachos (ORM) La Palma, Canary Islands (source: Javier Méndez, ING).

4.6. Target instrumentation

During a short intensive seeing campaign at the SAAO site in Sutherland in August 2011, the SALT combined MASS-DIMM instrument was calibrated against their Generalized Seeing Monitor (GSM) and Profileur de Bord Lunaire (PBL) by staff of the Laboratoire Hippolyte Fizeau of the Université de Nice Sophia-Antipolis. Three different optical remote sensing instruments were therefore employed simultaneously to measure optical parameters and turbulence profiles. This made it possible to cross-correlate SALT MASS-DIMM results with those from the GSM and PBL for verification, validation and calibration of the SALT MASS-DIMM. Combining the three different techniques provided for instruments complementing each other. The entire atmosphere could be sampled at a higher resolution and a number of seeing parameters could be measured. A possibility exists that the GSM and PBL as well as a spare DIMM from SAAO could be made available for a short intensive site testing campaign at Matjiesfontein. For continuous monitoring of local meteorological parameters to be used in support of seeing measurements and turbulence modelling, an Automatic Weather Station (AWS) needs to be installed on-site, in close proximity to the seeing monitor. Techniques and

instrumentation currently employed as part of site characterisation to determine seeing and boundary layer conditions are briefly described in Appendix A4. Instrumentation, such as the DIMM, MASS, MASS-DIMM, GSM and PBL, that could become available for use during short seeing campaigns, are described in detail in Appendix A4.

5. Results and discussion

5.1. Introduction

Site characterisation requires knowledge of the vertical distribution of optical turbulence, the $C_N^{\ 2}(h)$ profile. Such a profile may be obtained by turbulence and optical methods. Dr Igor Esau of NERSC has used LESNIC to compile a database of turbulence-resolving simulations named DATABASE64 (DB64). It consists of a collection of LESNIC runs for a stably stratified planetary boundary layer (SBL) over a homogeneous aerodynamically rough surface (Esau, 2004). The large-eddy simulation technique's ability to determine seeing conditions has been tested by employing the first eight runs from DB64. The $C_N^{\ 2}(h)$ profiles and seeing parameter values obtained from DB64 results are presented and compared with observational results that have been published in the literature. Results from tests of the newly acquired seeing monitor hardware, and preliminary seeing measurements using the PSF technique, are also presented.

5.2. Turbulence method

5.2.1. Preliminary results using LESNIC

In Figure 5.1 and Table 5.1, respectively, profiles of the refractive index structure parameter $C_N^{\ 2}(h)$ and the temperature structure parameter $C_T^{\ 2}(h)$ as well as seeing parameter values for the first eight LESNIC runs from DB64, which cover a broad range of stability conditions in the PBL, as indicated in Section 3.2.3, are presented.

Profiles of $C_N^{\ 2}$ and $C_T^{\ 2}$ using DB64 Runs 1 to 8

Profiles of $C_N^{\ 2}$ and $C_T^{\ 2}$ for the first eight SBL runs of DB64, obtained as indicated in Section 3.2.3, are displayed in Figure 5.1.
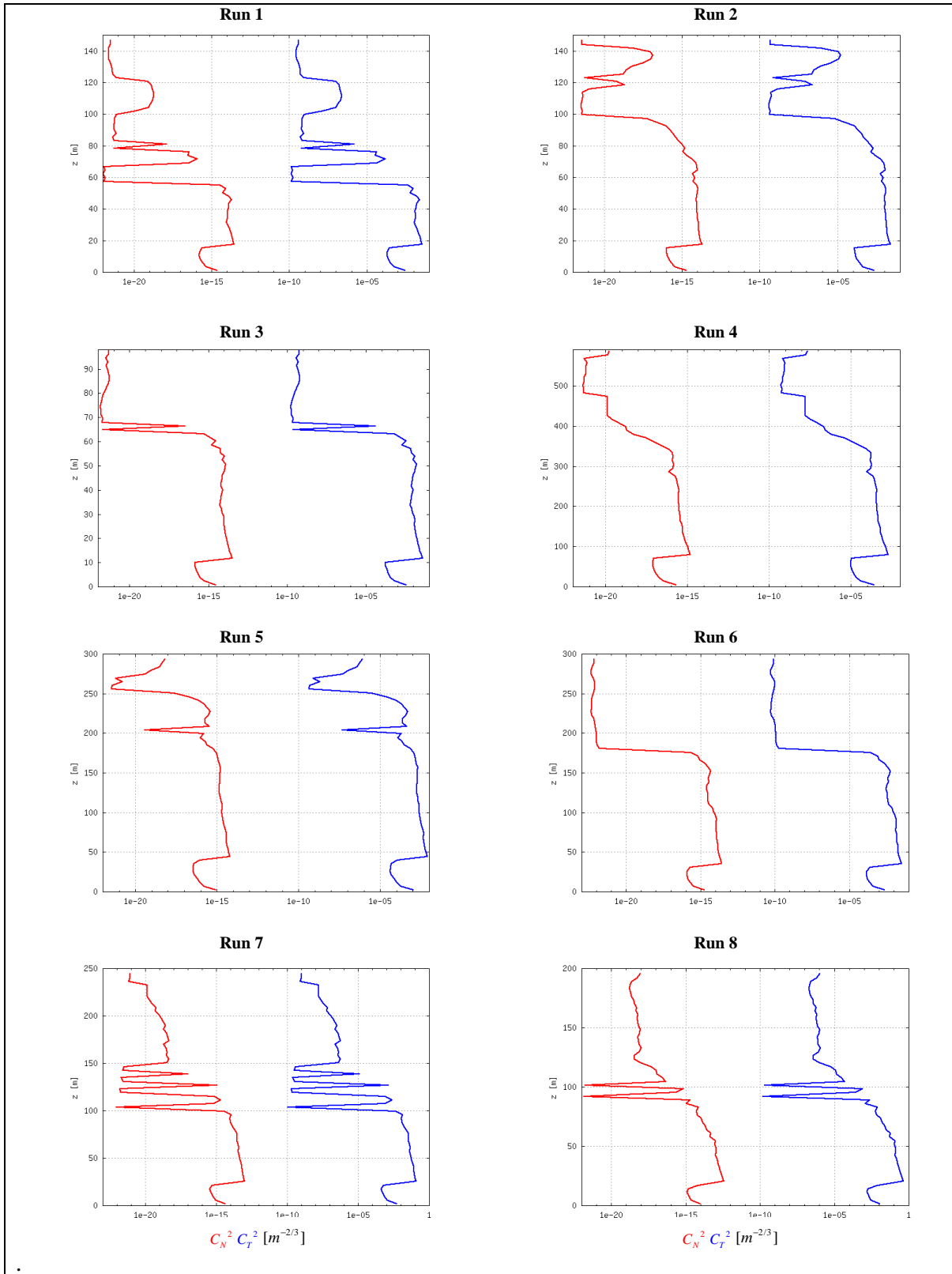
Figure 5.1. The simulated $C_N^{\,2}(h)$ and $C_T^{\,2}(h)$ log profiles for runs 1 to 8 of DB64

Seeing parameter values using DB64 Runs 1 to 8

Values of r_0 and ε_{FWHM} for the first eight SBL runs of DB64, obtained as indicated in Section 3.2.3 (with $\lambda = 532$ nm), are displayed in Table 5.1:

Table 5.1. Fried parameter value and seeing for the first eight runs in DB64.

Seeing parameters	Run1	Run2	Run3	Run4	Run5	Run6	Run7	Run8
r_0 (cm)	21	20	16	120	41	19	10	5
ε_{FWHM} (")	0.5	0.5	0.7	0.1	0.3	0.6	1.1	2.1

5.2.2. Results published in literature

Intense site testing campaigns have been taking place at Dome C in Antarctica, considered to be a site offering of the best astronomical seeing conditions on Earth. Balloon borne radiosonde measurements of $C_N^{\,2}$ profiles as well as seeing parameter values for Dome C have been made consistently over the past decade, and results are readily available in the literature. One such campaign, for which both $C_N^{\,2}$ profiles and seeing parameter values are available, is that which took place during the first winterover at Dome C in Antarctica in 2005 as reported on by Aristidi *et al*. (2009) and Trinquet *et al*. (2008).

The 2005 Dome C overwintering team launched meteorological balloon flights equipped with microthermal sensors to measure thermal fluctuations (mK) from Dome C to determine the vertical profile of the optical turbulence intensity $C_N^{\,2}(h)$ from the ground up to 20 km. The balloon transmitted the value of the refractive index structure constant every 1-2 seconds, which corresponds to a vertical resolution of 5-10 m. Meteorological parameters such as pressure, temperature, humidity and wind speed components were also provided by the soundings. Balloon launches started on the 15th of March 2005 (Flight Vol 520) during Autumn and concluded on the 19th of October (Flight Vol 575) during Spring.

3

Dome C is located at latitude 74.5° S on top of a local maximum of the Antarctic plateau, 3250 m above mean ice level. The Antarctic plateau is essentially free of topographic features. A surface roughness length of 0.005 m is allocated for such a featureless ice/snow surface. At the time of balloon launches, the AWS at Dome C provided surface measurements of wind speed, temperature, pressure and relative humidity (data and information obtained from IPEV/PNRA project "Routine Meteorological Observation at Station Concordia – www.climantartide.it"). Over the entire campaign, wind speeds ranged from 0-5 m.s^{-1}, temperatures from -74 °C to -52 °C (199-221 K), pressure from 618-658 mBar (61800-65800 Pa) and relative humidity from 14% to 60% (mostly either 14% or 15%).

Published results of observed $C_N^{\,2}(h)$ profiles

Thirty-two $C_N^{\,2}(h)$ profiles for the first 80 m above ground at Dome C in Antarctica (Aristidi *et al*. 2009) are displayed in Figure 5.2. The profiles are based on measurements made with balloon radio soundings, obtained during an astronomical site testing campaign at Dome C from 15 March (Flight Vol 520) – 19 October (Flight Vol 575) 2005 by Trinquet *et al*. (2008).

Published results of seeing parameter values

Seeing (ε_{FWHM}) for heights of 8 m and 33 m above the ice surface were retrieved from the above mentioned balloon profiles by Trinquet *et al*. (2008) by making use of Equation (2.21). Seeing at 8 m ranged from 0.5"-3.6" while that at 33 m ranged from 0.2"-2.5" over the entire campaign. These seeing values correspond to Fried parameter (r_0) values of 22 cm to 3 cm at 8 m and 54 cm to 4 cm at 33 m (for $\lambda = 532$ nm).
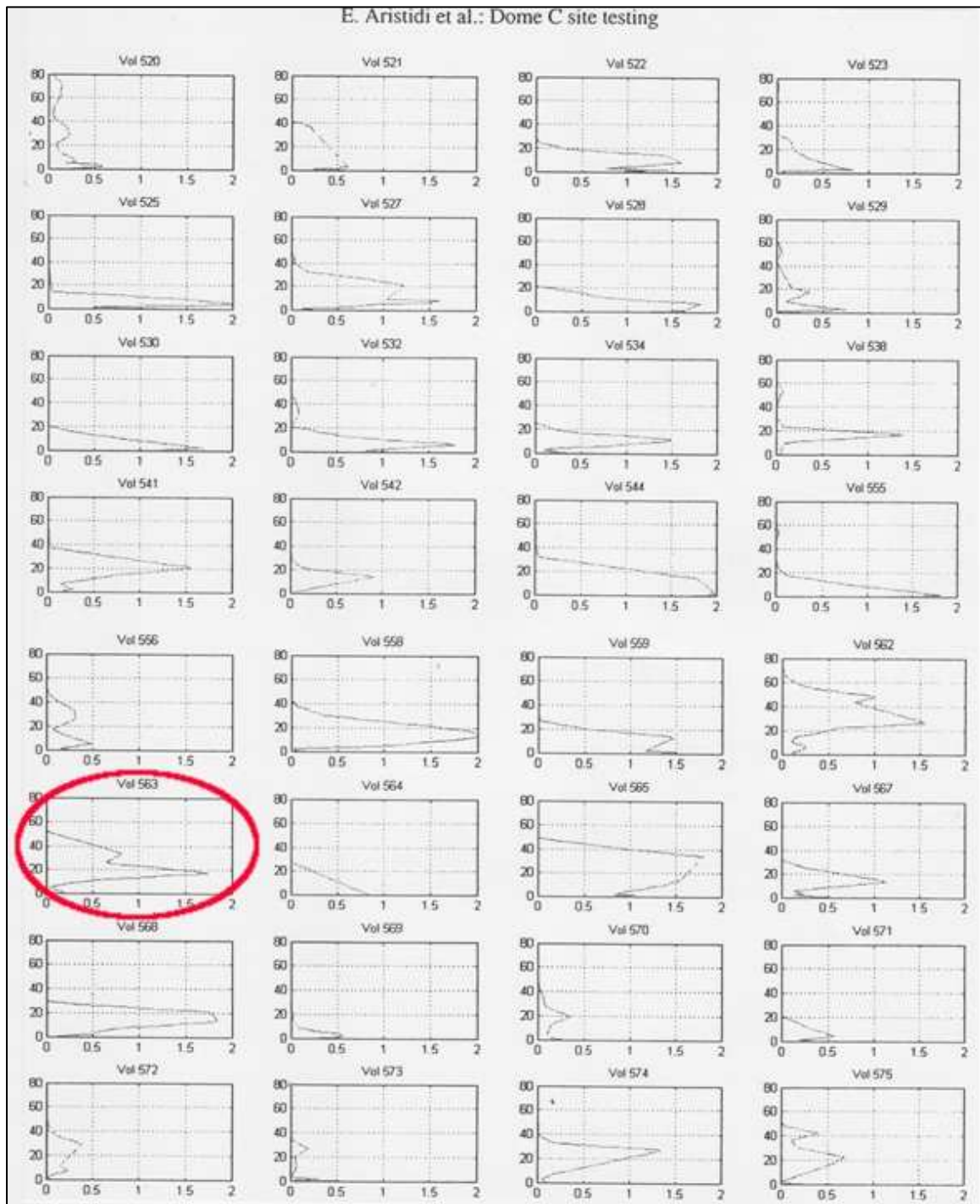
Figure 5.2. The observed $C_N^2(h)$ profiles obtained during site testing at Dome C in Antarctica (source: Aristidi *et al*., 2009). The value of $C_N^2(h)$ is indicated on a linear scale on the horizontal axis in units of $[10^{-13} \, \text{m}^{-2/3}]$ while the height above ground is displayed in [m] on the vertical axis. Flight Vol 563, circled in red, was utilized for comparison purposes.

5.2.3. Comparison of simulated and published results

Simulated vertical profiles of $C_N^2(h)$ and seeing parameter values have been obtained by making use of DB64 results for the nocturnal boundary layer. These profiles and values have been compared with observational profiles and seeing parameter values from literature. Such a comparison is necessary to verify that the profiles produced by turbulence modelling are at least similar in nature and order of magnitude to measured $C_N^2(h)$ profiles, and that seeing parameter values are of a similar order of magnitude to values appearing in the literature. This will then provide either negative or positive assurance that LESNIC gives reasonable results when its *a-priori* parameters are similar to some extent to the experimentally derived results.

Simulated results for $C_N^2(h)$ profiles with linear scale on x-axis

Profiles of $C_N^2(h)$ from DB64 were plotted on a logarithmic scale for the C_N^2-axis. Observational profiles of $C_N^2(h)$ from literature are displayed on a linear scale. Profiles of $C_N^2(h)$ for the eight runs of DB64, re-plotted on a linear scale for comparison purposes, as well as the LESNIC external control parameters for each run, are displayed in Figure 5.3.

Comparison of $C_N^2(h)$ profiles

Profiles of $C_N^2(h)$ obtained from the first 8 runs of DB64 by turbulence-modelling of the nocturnal boundary layer with LESNIC (Figure 5.3) were compared with 32 observational profiles (Figure 5.2) measured by balloon radio sounding at Dome C in Antarctica during the austral winter of 2005 by the Dome C overwintering team as part of an astronomical site testing campaign as reported in the literature (Aristidi *et al*. 2009).

Such a comparison is possible for the following reason: The study of turbulence in the PBL is based on the solution of the Reynolds-averaged Navier-Stokes equations, which present the conservation laws of momentum, energy and fluxes. The particular realisation of turbulence characteristics is calculated subject to boundary conditions at the top and bottom of the PBL. It is then possible to compare the numerical results with experimental data which have been collected at the same boundary conditions. Generally, the turbulence

Run 1

External control parameters	
Domain size [m]	300x300x150
Latitude [°]	70
Surface roughness [m]	0.05
Surface heat flux [K.m.s^{-1}]	-0.002
Geostrophic wind [m.s^{-1}]	3
Surface temperature [K]	283
Surface pressure [Pa]	90500
Relative humidity [%]	70

Run 2

External control parameters	
Domain size [m]	200x200x150
Latitude [°]	70
Surface roughness [m]	0.07
Surface heat flux [K.m.s^{-1}]	-0.002
Geostrophic wind [m.s^{-1}]	3
Surface temperature [K]	283
Surface pressure [Pa]	90500
Relative humidity [%]	70

Run 3

External control parameters	
Domain size [m]	150x150x100
Latitude [°]	90
Surface roughness [m]	0.03
Surface heat flux [K.m.s^{-1}]	-0.002
Geostrophic wind [m.s^{-1}]	3
Surface temperature [K]	283
Surface pressure [Pa]	90500
Relative humidity [%]	70

Run 4

External control parameters

Not available

$$C_N{}^2 \; [m^{-2/3}]$$

Figure 5.3. The $C_N{}^2(h)$ linear profile and LESNIC external control parameters for runs 1 to 8.

Run 5

External control parameters	
Domain size [m]	450x450x300
Latitude [°]	45
Surface roughness [m]	0.1
Surface heat flux [K.m.s^{-1}]	-0.003
Geostrophic wind [m.s^{-1}]	5
Surface temperature [K]	283
Surface pressure [Pa]	90500
Relative humidity [%]	70

Run 6

External control parameters	
Domain size [m]	400x400x300
Latitude [°]	45
Surface roughness [m]	0.1
Surface heat flux [K.m.s^{-1}]	-0.004
Geostrophic wind [m.s^{-1}]	5
Surface temperature [K]	283
Surface pressure [Pa]	90500
Relative humidity [%]	70

Run 7

External control parameters	
Domain size [m]	350x350x250
Latitude [°]	45
Surface roughness [m]	0.1
Surface heat flux [K.m.s^{-1}]	-0.005
Geostrophic wind [m.s^{-1}]	5
Surface temperature [K]	283
Surface pressure [Pa]	90500
Relative humidity [%]	70

Run 8

$C_N{}^2 \; [m^{-2/3}]$

External control parameters	
Domain size [m]	300x300x200
Latitude [°]	45
Surface roughness [m]	0.1
Surface heat flux [K.m.s^{-1}]	-0.006
Geostrophic wind [m.s^{-1}]	5
Surface temperature [K]	283
Surface pressure [Pa]	90500
Relative humidity [%]	70

Figure 5.3 (continued from the previous page). The $C_N{}^2(h)$ linear profile and LESNIC external control parameters for runs 1 to 8.

is determined by the geostrophic wind and the temperature difference between the top and bottom of the PBL ($\Delta T > 0$ corresponds to stable stratification, which is relevant to astronomical seeing conditions). Therefore PBL turbulence will be the same for hot climatic conditions (for example, $\Delta T = T_{top} - T_{bottom} = 35°C - 30°C = 5°C$) as it is for very cold climatic conditions, such as those of Antarctica (for example, $\Delta T = T_{top} - T_{bottom} = -30°C - (-35°C) = 5°C$).

LESNIC can only be used to provide a generalised profile based on the input parameters as indicated in Figure 5.3. These control parameters do not necessarily correspond with those prevalent at Dome C (meteorological surface conditions for Dome C are discussed in Section 5.2.2), and a direct comparison is therefore not possible. However, by comparing the profiles, it is possible to determine whether the profiles produced by LESNIC are at least of roughly the same shape and scale as the observed profiles, and whether LESNIC can therefore be used as a general tool to evaluate sites at some level.

In comparing the simulated $C_N^2(h)$ profiles of Figure 5.3 with the observed profiles of Figure 5.2, it is immediately apparent that the simulated profiles, in general, do not appear similar in shape to the observed profiles. However, from Figure 5.3, it is also apparent that the observed profiles are themselves dissimilar in shape for the entire observation period. Profiles change with every flight. Some profiles include a second peak, while others do not. The eight simulated profiles are similar in shape and also do resemble a few of the observational profiles in shape, especially Flights Vol 562 and 563 and, to a lesser extent, Flights Vol 538, 541 and 574.

One of the observed profiles which compares favourably in shape with the simulated profiles, Flight Vol 563, is displayed in Figure 5.4. The simulated profile produced in Run 8 is displayed in Figure 5.5 for comparison. The two $C_N^2(h)$ profiles compare well for similarity in shape and order-of-magnitude.

$$C_N{}^2\,[10^{-13}\,m^{-2/3}]$$
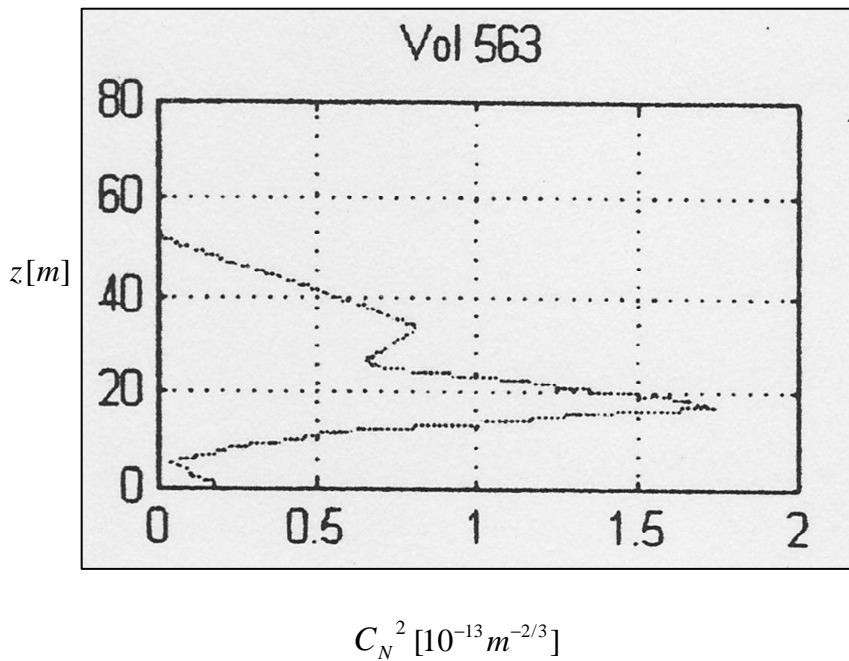
Figure 5.4. Flight Vol 563 $C_N{}^2(h)$ profile measured at Dome C, Antarctica (source: Aristidi *et al*., 2009).

$$C_N{}^2\,[m^{-2/3}]$$
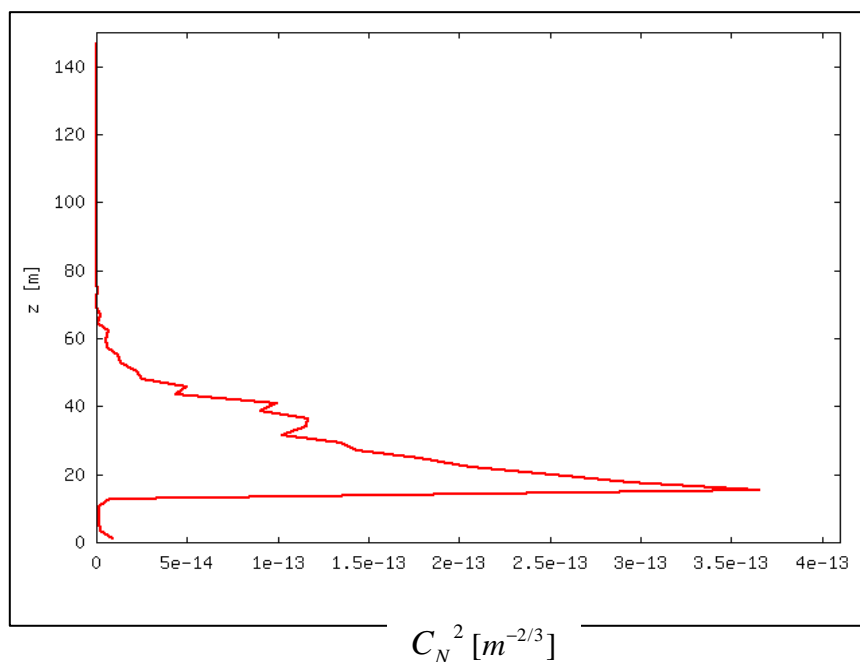
Figure 5.5. The LESNIC-modelled $C_N{}^2(h)$ profile for run 8 from DB64.

With regards to scale, for the observed profiles, Trinquet *et al*. (2008) reports $C_N{}^2$ values of 3×10^{-14} m$^{-2/3}$ near the ground, which rapidly decreases to 10^{-17} m$^{-2/3}$ at a height of 100 m. Simulated profiles display $C_N{}^2$ values in the region of 10^{-16}-10^{-13} m$^{-2/3}$. The quantitative

shapes of the simulated profiles, when compared to the observational profiles from literature, are generally quite reasonable.

Comparison of r_0 and ε_{FWHM}

Seeing parameter values calculated from the simulated profiles range from 0.1" to 2.1" for ε_{FWHM} and from 120 cm to 5 cm for r_0. Seeing parameter values retrieved from observed profiles range from 0.5" to 3.6" for ε_{FWHM} and from 22 cm to 3 cm for r_0 at 8 m and from 0.2" to 2.5" for ε_{FWHM} and from 54 cm to 4 cm for r_0 at 33 m. Seeing parameter values obtained from the model are therefore in close agreement with observed values (from literature).

5.3. Optical method

A recent trip to Matjiesfontein presented an opportunity to test newly acquired seeing monitor equipment. Preliminary seeing measurements for the PSF seeing experiment were performed as follows:

The seeing monitor setup consisted of the Meade 14" f/10 SCT with GOTO fork-arm mount supported by the heavy-duty tripod as well as the 4.4-μm Point Grey Grasshopper GRAS-20S4M monochrome CCD camera attached to a flip mirror on the exit pupil of the telescope. The seeing monitor was deployed outside the Matjiesfontein courthouse. Dark, clear, dry and windless conditions prevailed. Considerable ambient light was present. The two visible components of the Alpha Centauri binary system, Alpha Centauri A and B (α Cen AB) were centred in an eye piece which was also attached to the flip mirror. The CCD camera was set to capture short exposure images of ~ 1 ms at a frame rate of ~ 7 fps.

For the combination of:
- the 14" (= 350 mm) aperture diameter telescope with a focal ratio of f/10, therefore focal length of 3500 mm as given by Equation (4.1), and
- a CCD camera with 4.4-μm pixel size,

the image scale is given by Equation (3.5) as being 0.26 arc-second per pixel.

5.3.1. Point Spread Function (PSF) seeing experiment: calibration results using αCen binary separation

The first test entailed seeing monitor setup verification, i.e. determining whether the seeing monitor setup would perform as expected. The short 1-ms exposure images of the Alpha Centauri AB binary system captured at a frame rate of ~ 7 fps were analysed to determine the binary separation given by the seeing monitor setup. This observed separation could then be compared with the known separation according to the literature.

Image analysis thus consisted of the following –

1. Finding the separation between the principle, αCenA, and the companion, αCenB, of the Alpha Centauri AB binary star system:

   Image uploaded into GIMP image editor to provide x and y coordinates of pixels using Treshold tool to locate pixel with peak intensity value at centre of star image for both stars.

   Separation of components in CCD camera pixels is given by

   $$d = \sqrt{(\Delta x)^2 + (\Delta y)^2}. \tag{5.1}$$

   Separation of components in arc-seconds is given by

   $$\rho = 0.26''/\,\text{pixel} \times d \,\text{ pixels}. \tag{5.2}$$

   From Table 5.2, for the 10 images observed and captured with the seeing monitor setup, the average separation of the binary star components was calculated to be $5.3'' \pm 0.3''$.

2. Comparing the observed value for the binary star separation of 5.3" to the separation given by the literature of 5.4" (from The Sixth Catalog of Orbits of Visual Binary Stars, 2006).

The close agreement between the observed and stated values verifies and validates the operation of the current seeing monitor setup for the PSF seeing experiment.
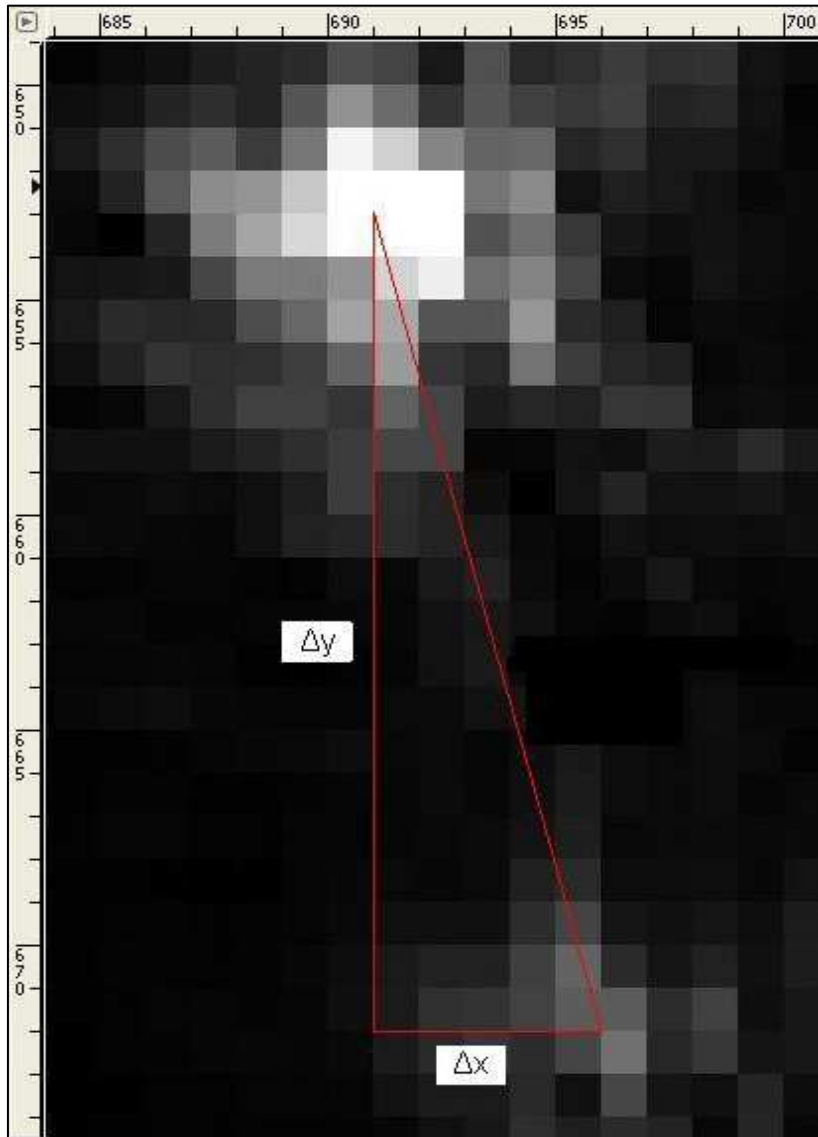
Figure 5.6. Separation of binary stars were found by importing captured images into an image editor, locating the pixel with peak intensity at the centres of both stars and calculating their separation.

Table 5.2. PSF seeing experiment: verification of seeing monitor setup by observing binary star separation.
Image no. 2 was a non-observation – the companion, αCenB, was not observed, probably being obscured by high thin cloud.

Image scale = 0.26"/pixel	αCenA		αCenB							
Image	x	y	x	y	$x_{\alpha2}-x_{\alpha1}$	$y_{\alpha2}-y_{\alpha1}$	$(x_{\alpha2}-x_{\alpha1})^2$	$(y_{\alpha2}-y_{\alpha1})^2$	d	ρ
no.	pixels	pixels	pixels	pixels	pixels	pixels	pixels	pixels	pixels	"
0	691	653	696	672	5	19	25	361	19.65	5.1
1	692	654	696	673	4	19	16	361	19.42	5.0
2	691	657	-	-	-	-	-	-	-	
3	689	653	694	675	5	22	25	484	22.56	5.9
4	693	654	696	673	3	19	9	361	19.24	5.0
5	691	655	695	675	4	20	16	400	20.40	5.3
6	689	655	696	676	7	21	49	441	22.14	5.8
7	688	655	694	674	6	19	36	361	19.92	5.2
8	691	653	695	672	4	19	16	361	19.42	5.0
9	688	655	693	675	5	20	25	400	20.62	5.4
Average separation (")									20.37	5.3
+/-									1.21	0.3
Separation from literature (") (2012)										5.4

5.3.2. Point Spread Function (PSF) seeing experiment: initial results with αCenA

The second test entailed performing a preliminary PSF seeing experiment. Images of the brightest star of the binary system, αCenA, which had been captured outside the Matjiesfontein courthouse, were analysed to determine the FWHM of the star's intensity profile and thus the seeing.

Image analysis thus consisted of the following –

1. Obtaining four intensity profiles of αCenA for each of the 10 images:

    Image uploaded into AstroArt astronomical image processing program and pixel lines drawn through centre of star image (as determined in previous experiment), providing the four intensity profiles for each image.
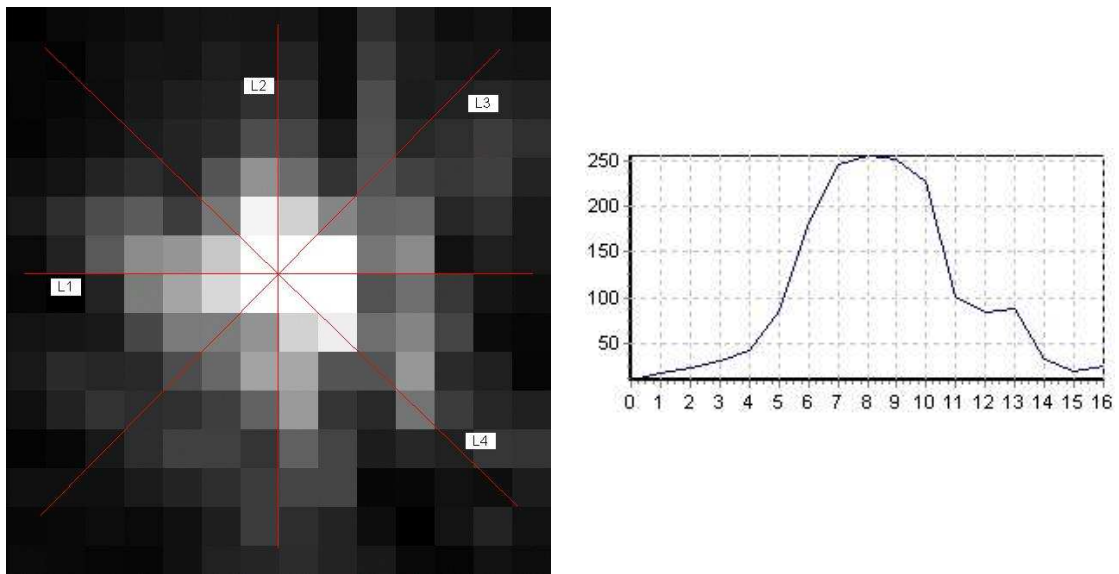
Figure 5.7. Intensity profiles were obtained by importing captured images into an astro-imaging application and analysing the images.

2. Performing a nonlinear regression analysis with a Gaussian fit to the star's intensity profile (4 profiles per image, 10 images):

    F`orm of Gaussian equation is given by

$$y = ae^{\left[-0.5\left(\frac{x-x_0}{b}\right)^2\right]}. \tag{5.3}$$
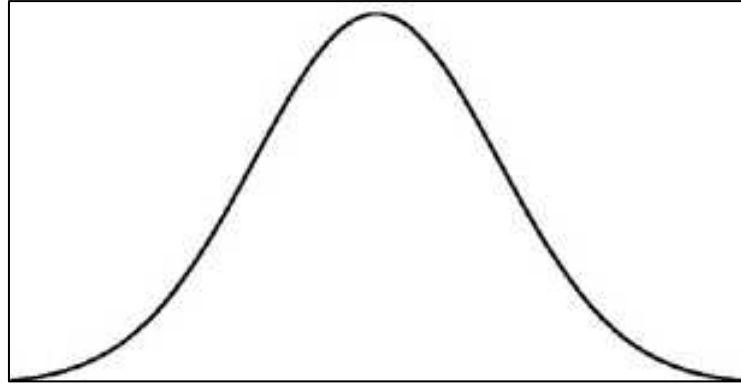
Figure 5.8. Bell-shaped Gaussian distribution curve.

3. Obtaining the standard deviation (b in pixels, see Table 5.3), from the Gaussian distribution, of the FWHM of the star's intensity profile.

4. Obtaining the standard deviation σ (Table 5.3) in arc-seconds (by converting from pixels to arc-seconds using the image scale)

$$\sigma\,["] = 0.26"/\,\text{pixel} \times \sigma\,[\text{pixels}]. \qquad (5.4)$$

5. Obtaining the FWHM, and thus the seeing ε_{FWHM} (Table 5.3), from the standard deviation σ according to Equation (3.7a)

$$\varepsilon_{FWHM} = FWHM = 2.355 \times \sigma. \qquad (5.5)$$

The average seeing measured outside the Matjiesfontein courthouse was $2.1" \pm 0.47"$, which is very good seeing conditions given the surroundings. It also compares well with previous seeing measurements at Matjiesfontein which delivered seeing of 1-2" (Combrinck *et al.*, 2007).

Table 5.3. PSF seeing experiment: initial seeing results at Matjiesfontein with αCenA.

Image scale = 0.26"/pixel

σ (") = **0.26* b**

ε_{FWHM} (") = FWHM (") = 2.355*σ

Image no.

Pixel line	0			1			2			3			4		
	b	σ	ε_{FWHM}	b	σ	ε_{FWHM}	b	σ	ε_{FWHM}	b	σ	ε_{FWHM}	b	σ	ε_{FWHM}
	pixels	"	"	pixels	"	"	pixels	"	"	pixels	"	"	pixels	"	"
1	2.424	0.63	**1.5**	2.946	0.77	**1.8**	3.947	1.03	**2.4**	2.095	0.54	**1.3**	5.512	1.43	**3.4**
2	2.647	0.69	**1.6**	2.660	0.69	**1.6**	5.722	1.49	**3.5**	2.891	0.75	**1.8**	3.853	1.00	**2.4**
3	2.133	0.55	**1.3**	2.632	0.68	**1.6**	3.957	1.03	**2.4**	2.720	0.71	**1.7**	3.465	0.90	**2.1**
4	2.525	0.66	**1.5**	3.182	0.83	**1.9**	3.942	1.02	**2.4**	4.178	1.09	**2.6**	5.165	1.34	**3.2**
Average/image (")			**1.5**			**1.7**			**2.7**			**1.8**			**2.8**

Image no.

Pixel line	5			6			7			8			9		
	b	σ	ε_{FWHM}	b	σ	ε_{FWHM}	b	σ	ε_{FWHM}	b	σ	ε_{FWHM}	b	σ	ε_{FWHM}
	pixels	"	"	pixels	"	"	pixels	"	"	pixels	"	"	pixels	"	"
1	2.896	0.75	**1.8**	6.541	1.70	**4.0**	2.774	0.72	**1.7**	3.496	0.91	**2.1**	3.008	0.78	**1.8**
2	2.375	0.62	**1.5**	4.712	1.23	**2.9**	2.527	0.66	**1.5**	4.158	1.08	**2.5**	3.166	0.82	**1.9**
3	3.939	1.02	**2.4**	3.382	0.88	**2.1**	2.656	0.69	**1.6**	2.825	0.73	**1.7**	3.248	0.84	**2.0**
4	3.980	1.03	**2.4**	3.972	1.03	**2.4**	3.179	0.83	**1.9**	2.504	0.65	**1.5**	3.467	0.90	**2.1**
Average/image (")			**2.0**			**2.8**			**1.7**			**2.0**			**2.0**

Overall average (")	2.1	+/-	0.5

6. Combination of methods

6.1. Introduction

In this chapter the use of a two-sided complementary approach to numerically model and experimentally measure seeing at a site is proposed. Seeing parameter values may be obtained from numerical modelling with LESNIC and also by experimental measurement with a seeing monitor. It should be possible to compare seeing values obtained by these two methods to verify whether modelled results obtained with LESNIC may be used in conjunction with measured results from the seeing monitor to predict the seeing at a site. Calibration of modelling will be accomplished by employing the measured results. The two-sided approach is an attempt at integrating methods from boundary layer meteorology and astronomical seeing. If seeing conditions could be connected to weather conditions, it would be possible to forecast seeing at a site. Experimental techniques alone cannot cover the almost infinite state of the PBL and also do not offer longer term prediction capability. On the other hand, LESNIC is based on prognostic equations and can thus be used as a predictive tool with due consideration of its limitations.

6.2. Proposed two-sided approach

To evaluate astronomical seeing conditions at a site, a two-sided approach is proposed – on the one hand, the use of a turbulence-resolving numerical model, the Large Eddy Simulation NERSC (Nansen Environmental and Remote Sensing Centre) Improved Code (LESNIC) while, on the other hand, obtaining quantitative seeing measurements with a seeing monitor. The latter should be used to verify and calibrate results produced by the LESNIC model.

Seeing monitor data should be compared with modelled results: (1) to determine whether LESNIC is suitable for modelling seeing conditions and, if so, (2) to fine-tune the model to make its seeing quality predictions more accurate and also (3) to calibrate the model. If a good correlation between actual seeing quality and the LESNIC model's predicted results can be found, it would be possible to employ meteorological data together with the

LESNIC model to select a suitable observing site as well as to forecast seeing quality at the site.

Seeing may be quantified in two ways: (1) theoretically, by making use of statistical parameters from the Kolmogorov model of turbulence (Kolmogorov, 1941) as developed by Tatarski (1961) and Fried (1965 & 1966) and (2) experimentally, by comparison of ideal and observed images.

An integrated approach should be followed to determine the seeing conditions at a site –

- On-site data collection with seeing monitor to provide seeing and Fried parameter values as follows:
    1. Capture image of bright star.
    2. Determine FWHM of star's intensity profile (PSF).
    3. Obtain seeing ε_{FWHM} from FWHM using Equation (3.7a).
    4. Calculate Fried parameter r_0 from seeing ε_{FWHM} by using Equation (3.7b).
- On-site data collection with Automatic Weather Station (AWS) to provide meteorological parameters such as temperature, pressure, humidity, wind speed etc. used as input into LESNIC model to obtain seeing and Fried parameter values from LESNIC as follows:
    1. Obtain $C_N^{\,2}(h)$ profile from Equation (2.13), where profiles of $C_T^{\,2}(h)$, $T(h)$ and $P(h)$ are provided by DATABASE64 using Equation (3.1) to Equation (3.4).
    2. Calculate Fried parameter r_0 from $C_N^{\,2}(h)$ profile using Equation (2.20).
    3. Calculate seeing ε_{FWHM} from Fried parameter r_0 using Equation (2.21).
- Comparison of seeing results ($r_{0_{\mathbf{L}}}$, $\varepsilon_{FWHM_{\mathbf{L}}}$) calculated with LESNIC model with measured seeing results ($r_{0_{\mathbf{SM}}}$, $\varepsilon_{FWHM_{\mathbf{SM}}}$).
- Calibration of LESNIC model by using measured seeing data to improve on LESNIC model and its parameters.
- Use of LESNIC to accurately forecast seeing conditions.

MODEL

LESNIC

$$C_N^2(h) = \left(80 \times 10^{-6} \frac{P(h)}{T^2(h)}\right)^2 C_T^2(h)$$

$$r_0 = \left(16.7\lambda^{-2} \frac{1}{\cos\gamma} \int_0^\infty C_N^2(h)dh\right)^{-3/5}$$

$$\varepsilon_{FWHM} = 0.98\frac{\lambda}{r_0} = 5.25\lambda^{\frac{-1}{5}}\left(\int_0^\infty C_N^2(h)\,dh\right)^{\frac{-3}{5}}$$

MEASUREMENT

SEEING MONITOR

PSF

$$\varepsilon_{FWHM} = FWHM = 2\sqrt{2\ \ln 2}\ \ \sigma \approx 2.355\ \ \sigma$$

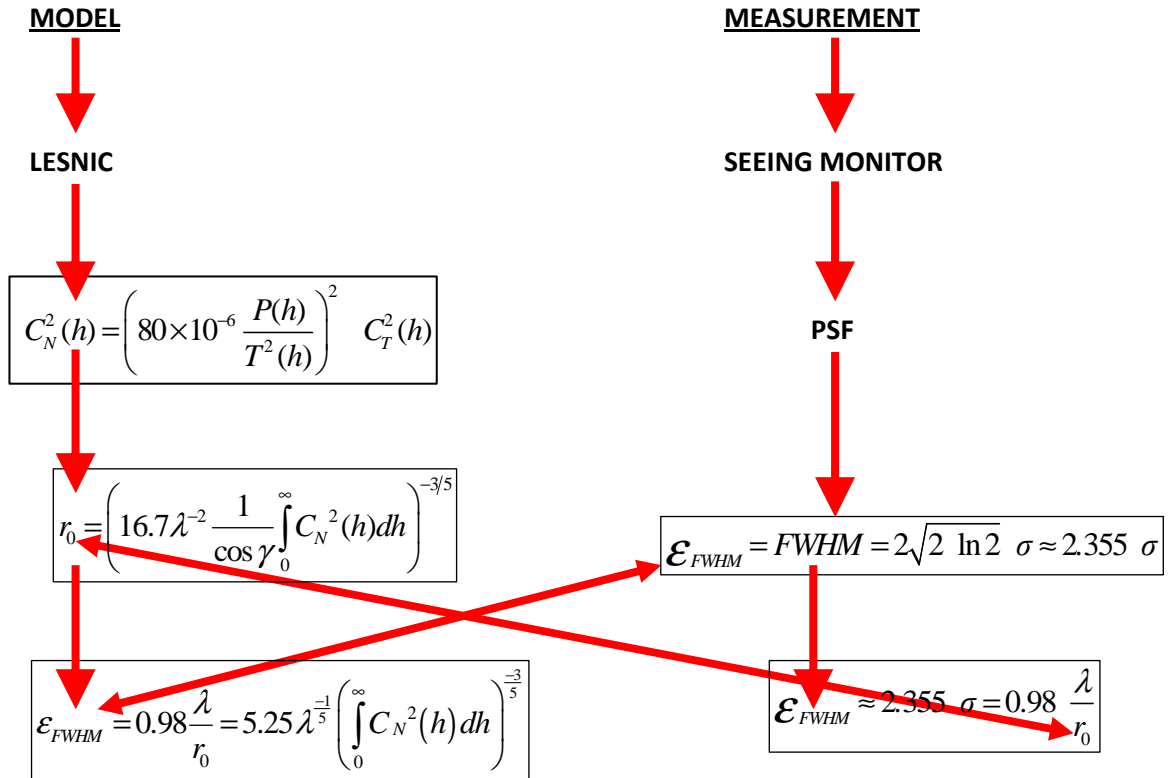$$\varepsilon_{FWHM} \approx 2.355\ \ \sigma = 0.98\ \frac{\lambda}{r_0}$$

Figure 6.1. Comparison of modelled and measured Fried and seeing parameter results.

7. Conclusion

7.1. Summary

In summary, due to high atmospheric extinction, high levels of cloud cover and bad astronomical seeing, HartRAO as site is not suitable to collect LLR data from. It is therefore necessary to identify a new site for the location of a space geodetic observatory able to deliver data of international standard. The site must be suitable for hosting an LLR system. The LLR's laser beam is degraded by turbulence in the atmosphere, especially in the PBL. The LLR requires seeing conditions of at least 1"-2". A potential site must therefore be characterised with respect to seeing conditions. Measuring seeing at various locations on-site will assist in determining the most suitable location for the LLR. To determine seeing at a site, a two-pronged approach, combining methods from boundary layer meteorology and astronomical seeing, is envisaged. Atmospheric turbulence can be modelled with a turbulence-resolving model such as LESNIC. Optical seeing conditions can be measured quantitatively with a self-built seeing monitor. In conclusion, to follow, a discussion of the current situation, conclusions and future plans.

7.2. LESNIC

The effects of turbulence on the propagation of a laser beam from the Earth to the Moon and back again may be found by determining the vertical distribution of turbulence, the $C_N^{\,2}(h)$ profile. $C_N^{\,2}(h)$ profiles can be used to determine astronomical seeing conditions as part of site characterisation. *In situ* methods of determining astronomical seeing are difficult, time-consuming and costly in terms of equipment. In practical terms, it is impossible to carry out observations which cover all PBL conditions. Employing a turbulence-resolving model such as LESNIC, supported by measurement of meteorological parameters by means of meteorological instrumentation, would seem feasible for delivering and predicting $C_N^{\,2}(h)$ profiles.

The suitability of using LESNIC to model seeing conditions was investigated. The LESNIC model seems capable of reproducing observed $C_N^{\,2}(h)$ profiles and delivering

seeing parameter values consistent with results from field campaigns as reported. Turbulence-resolving models, such as LESNIC, therefore show potential for delivering and predicting profiles and parameters to characterise astronomical seeing.

By making use of site-specific data for initial and boundary conditions as well as for topographic features and surface roughness, a turbulence-resolving model such as LESNIC may potentially be used to deliver and predict $C_N^{\,2}(h)$ profiles, which can then be used to determine astronomical seeing conditions as part of site characterisation. Numerical simulations will allow for determining conditions during specific observation periods and, more importantly, long-term seeing conditions as well.

7.3. Seeing monitor

Astronomical seeing parameters can also be measured by employing a seeing monitor on-site. Using the double star separation technique for verification and calibration purposes, and the PSF technique to measure the seeing ε_{FWHM}, the ideal PSF seeing monitor assembly must be able to deliver a resolution of better than 1 arc-second. The optimal combination of telescope, mount and CCD camera for the PSF technique was investigated. It resulted in the purchase of a second-hand 14" Meade LX200 GPS SCT with a computer-controlled heavy-duty alt-az fork-type mount as well as a Point Grey Grasshopper GRAS-20S4M CCD camera.

The newly acquired equipment and setup were tested during preliminary seeing measurements with the double star separation and PSF techniques outside the Matjiesfontein courthouse. The seeing monitor setup was verified by close agreement of an observed binary star separation and its stated value. Using the PSF technique, seeing was determined to be ~ 2", which agrees with previously determined seeing at Matjiesfontein.

Vibrations seem to be easily introduced to the fork-arm mount by any windy conditions and it takes a while for these vibrations to damp down. The alt-az fork-arm mount will have to be replaced with a GE mount eventually. The A-P 1600GTO GE mount was identified as the only mount with the required payload capacity. The 1600GTO is capable

of carrying 90 kg. The added payload capacity may seem excessive, but wind loading also increases the effective load imparted to the mount. An enclosure would drastically reduce the wind load effect, and one of the smaller mounts listed in Table 4.1 may prove to be sufficient.

A Point Grey Grasshopper GRAS-03K2M-C CCD camera, together with Mac Mini, was also acquired with a view to adding the DIMM technique to the seeing monitor's repertoire. The DIMM technique is the standard technique used for site characterisation. SAAO has put their DIMM software, TimDIMM, at our disposal. All that is still required for the DIMM to be fully functional is a two-holed mask with wedge prism.

The intention is to also procure a PBL optical module and employ the PBL technique in future. The PBL technique's attraction lies in its making use of differential image motion of points along the Moon's limb. The LLR's laser beam is transmitted to, and reflected back from, retro-reflector arrays on the Moon. In the PBL configuration, the seeing monitor is therefore pointing in the same general direction and through a similar column of air as the LLR telescope. This would make it possible to model atmospheric refraction of the LLR's laser beam.

Immediate plans include a short seeing campaign using the PSF technique at the Matjiesfontein site. Setup for the DIMM technique - TimDIMM software and mask with wedge prism - should be completed by this time. Employing both the PSF and DIMM techniques would allow for cross-correlation of results and verification, validation and calibration of equipment.

The seeing monitor development will proceed at HartRAO as testing site. Control software and software for data processing and image analysis must be developed, streamlined and automated. The seeing monitor can be calibrated against the SALT MASS-DIMM at the SAAO site in Sutherland. The team from the University of Nice plans an extended seeing campaign using a PBL, GSM and LuSci, together with the SALT MASS-DIMM, at Sutherland in the near future. The possibility exists that the team would be able to fit in a

short seeing campaign at Matjiesfontein. This would also present another opportunity to calibrate the self-built seeing monitor.

The short seeing campaign should give an indication of whether seeing conditions of better than the ~ 2", measured outside the Matjiesfontein courthouse, prevail at the site itself. For any potential site, though, site characterisation with respect to seeing will have to take place over a prolonged period of time to investigate seasonal variations in seeing. The best and the worst seeing conditions that can be obtained for a site will have to be investigated. Extended seeing campaigns should be planned at times when marked changes in meteorological conditions occur. Except for temporal variations in the seeing, spatial variations due to local topography dictate that seeing will have to be measured from various on-site locations and for different sectors of the sky. This would require the manufacture of a stable but portable steel pier to mount the seeing monitor on. The portable pier can then be bolted to foundations laid at the various on-site locations. During such campaigns, the seeing monitor will be protected from wind by screens, and from the rain by waterproof covering. Once the most suitable site and on-site location for the LLR have been identified, the seeing monitor will be set up as a permanent long-term site seeing monitor. It will be placed in an enclosure on a platform nearby the LLR.

7.4. Combination of methods

With the proposed two-pronged approach, the experimental results obtained with the on-site seeing monitor will be used to verify and calibrate the numerical results produced by the LESNIC model. Modelled results (with meteorological conditions as input) will be compared with quantitative seeing measurements to determine whether a good correlation exists between the LESNIC model's predicted results and actual seeing quality at a site.

Comparing observational data and modelled results will also give an indication of seeing quality's relation to meteorological conditions. If any relationship can be found, it would be possible to use existing meteorological data to select a suitable observing site and to forecast seeing quality at the site.

In order to connect LESNIC model results with seeing monitor results, the seeing monitor will have to collect data at a site for which vertical profiles of meteorological parameters are available, such as the SAWS site at Irene in Pretoria. The site-specific meteorological parameters will be used as input to the LESNIC model. Results obtained with the two methods can then be compared. Should the results show good agreement, the possibility exists that LESNIC can be utilised to build up a database of astronomical seeing conditions for any site on Earth.

References

1. André, J.C. [et al.]. 1978. Modeling the 24-hour evolution of the mean and turbulent structures of the planetary boundary layer. *Journal of the Atmospheric Sciences*, **35**, 1861.

2. Andrews, L.C. and Phillips, R.L. 2005. *Laser beam propagation through random media.* 2nd ed. Bellingham, WA: SPIE Press, 2005.

3. Argyle, B. (ed.) 2004. Observing and Measuring Visual Double Stars. *Patrick Moore's Practical Astronomy Series.* London: Springer-Verlag, 2004: 19 & 86.

4. Aristidi, E. [et al.]. 2009. Dome C site testing: surface layer, free atmosphere seeing, and isoplanatic angle statistics. *Astronomy and Astrophysics*, **499**, 955-965.

5. Avila, R., Vernin, J. and Masciadri, E. 1997. Whole atmospheric-turbulence profiling with generalized SCIDAR. *Applied Optics*, **36**(30): 7898-7905.

6. Avila, R. [et al.]. 2008. LOLAS: an optical turbulence profiler in the atmospheric boundary layer with extreme altitude resolution. *Monthly Notices of the Royal Astronomical Society*, **387**(4): 1511-1516.

7. Azouit, M. [et al.].1980. Remote sensing of atmospheric turbulence by means of a fast optical method: a comparison with simultaneous in situ measurements. *Journal of Applied Meteorology*, **19**: 834-838.

8. Azouit, M. and Vernin, J. 2005. Optical turbulence profiling with balloons relevant to astronomy and atmospheric physics. *Publications of the Astronomical Society of the Pacific*, **117**: 536-543.

9. Barletti, R. [et al.].1977. Astronomical site testing with balloon borne radiosondes: results about atmospheric turbulence, solar seeing and stellar scintillation. *Astronomy and Astrophysics*, **54**: 649-659.

10. Beckers, J.M. 1993. On the relation between scintillation and seeing observations of extended objects. *Solar Physics*, **145**(2): 399-402.

11. Beckers, J.M. 2001. A seeing monitor for solar and other extended object observations. *Experimental Astronomy*, **12**: 1–20.

12. Bonner, C.S. [et al.]. 2008. SNODAR: a new instrument to measure the height of the boundary layer on the Antarctic plateau. *Ground-based and Airborne Instrumentation for Astronomy II. Proceedings of the SPIE*, **7014**: 70146I-70146I-7.

13. Bonner, C.S. [et al.]. 2009. SNODAR: an acoustic radar for atmospheric turbulence profiling with 1m resolution. *Acoustics Australia,* **37**(2): 47–51.

14. Bonner, C.S. [et al.]. 2009. SNODAR II: probing the atmospheric boundary layer on the Antarctic plateau. *Optical turbulence: astronomy meets meteorology. Proceedings of the optical turbulence characterization for astronomical applications.* Sardinia, Italy, 15 - 18 September 2008: 264-270.

15. Bonner, C.S. [et al.]. 2010. SNODAR: 2009 performance at Dome A, Antarctica. *Ground-based and Airborne Telescopes III. Proceedings of the SPIE*, **7733**: 77334A-77334A-6.

16. Born, M. and Wolf E. 1999. *Principles of optics: electromagnetic theory of propagation, interference and diffraction of light*. 7th ed. Cambridge: Cambridge University Press, 1999.

17. Breedlove, G. and Jordaan, F. [eds.]. 2000. *Environmental Potential Atlas for South Africa (ENPAT 2000).* Compiled by the Department of Environmental Affairs and Tourism, the University of Pretoria and GIS Business Solutions, July 2000.

18. Bufton, J.L. [et al.]. 1972. Measurements of turbulence profiles in the troposphere. *Journal of the Optical Society of America*, **62**(9): 1068-1070.

19. Cassen, P., Guillot, T. and Quirrenbach, A. 2006. *Extrasolar planet: Saas-Fee Advanced Course 31. The effects of atmospheric turbulence on astronomical observations.* Heidelberg: Springer-Verlag, 2006: 130-142.

20. Chou, S.-H. and Ferguson, M.P. 191. Heat fluxes and roll circulations over the western Gulf Stream during an intense cold-air outbreak. *Boundary-Layer Meteorology*, **55**: 255-281.

21. Combrinck, W.L. and Combrink, A.Z.A. 2004. Proposed new international Space Geodesy Facility for southern Africa. *35th COSPAR Scientific Assembly*, Paris, France, 18-25 July 2004: 270.

22. Committee on the National Requirements for Precision Geodetic Infrastructure; Committee on Seismology and Geodynamics; National Research Council. 2010.

Precise geodetic infrastructure: national requirement s for shared resources. Washington DC: National Academic Press, 2010. Also available at: http://books.nap.edu/catalog.php?record_id= 12954 (accessed 10 July 2011).

23. Combrinck, W.L. [et al.]. 2007. Report on preliminary geotechnical and tropospheric site investigation for a proposed space geodetic observatory near Matjiesfontein in the Great Karoo. *South African Journal of Geology*, **110**(2/3): 225-234.

24. Conan, R. [et al.]. 1999a. Measurement of the optical relevant parameters for high resolution astronomy with the Generalized Seeing Monitor (GSM). *Catching the Perfect Wave: Adaptive Optics and Interferometry in the 21st Century. Proceedings of a symposium held as a part of the 110th Annual Meeting of the ASP.* New Mexico, USA, 28 June-1 July 1998: 27.

25. Conan, R. [et al.]. 1999b. Spatio-temporal analysis of the wave front with the GSM. *Astronomy with Adaptive Optics: present results and future programs. Proceedings of an ESO/OSA topical meeting*. Sonthofen, Germany, 7-11 September 1998, **56**: 133.

26. Coulman, C.E. 1985. Fundamental and applied aspects of astronomical "seeing". *Annual Review of Astronomy and Astrophysics*, **23**: 19-57.

27. Crescenti, G.H. 1997. A look back on two decades of Doppler SODAR comparison studies. *Bulletin of the American Meteorological Society*, **78**(4): 651-673.

28. Dickey, J.O. [et al.]. 1994. Lunar Laser Ranging: a continuing legacy of the Apollo program. *Science*, **265**: 482-490.

29. Dierickx, P. 1992. Optical performance of large ground-based telescopes. *Journal of Modern Optics* **39**(3): 569-588.

30. Echevarría, J. [et al.].1998. Site Testing at Observatorio Astronomico Nacional in San Pedro Mártir. *Revista Mexicana de Astronomía y Astrofísica*, **34**: 47-60.

31. Echevarría, J. 2003. Site Testing at San Pedro Mártir. *San Pedro Mártir: Astronomical Site Evaluation. Revista Mexicana de Astronomía y Astrofísica. Serie de Conferencias*, **19**: 41-43.

32. Egner, S.E. [et al.]. 2006. Beyond conventional G-SCIDAR: the ground-layer in high vertical resolution. *Advances in Adaptive Optics II. Proceedings of the SPIE*, **6272**: 627256.

33. Egner, S.E. and Masciadri, E. 2007. A G-SCIDAR for ground-layer turbulence measurements at high vertical resolution. *Publications of the Astronomical Society of the Pacific*, **119**(862): 1441-1448.

34. Erasmus, D.A. 1986. Meteorological conditions affecting observing quality on Mauna Kea. *Publications of the Astronomical Society of the Pacific* **98**: 254-259.

35. Erasmus, D.A. 1988 & 1996. *Relating seeing quality to meteorological conditions: development of seeing quality forecasts and improvement of site selection procedures.* Available at: http://www.saao.ac.za/~erasmus/overfsee.htm (accessed 6 March 2012).

36. Erasmus, D.A. 2000. Meteorological conditions and astronomical observing quality ('seeing') at candidate sites for the Southern African Large Telescope. *South African Journal of Science* **96**: 1-8.

37. Esau, I. 2004. Simulation of Ekman boundary layers by large eddy model with dynamic mixed subfilter closure. *Environmental Fluid Mechanics*, **4**(3): 273-303.

38. Fried, D.L. 1965. Statistics of a geometric representation of wave front distortion. *Journal of the Optical Society of America* **55**(11): 1427-1435.

39. Fried, D.L. 1966. Optical resolution through a randomly inhomogeneous medium for very long and very short exposures. *Journal of the Optical Society of America* **56**(10): 1372-1379.

40. Fuchs, A., Tallon, M. and Vernin, J. 1998. Focusing on a turbulent layer: principle of the "Generalized SCIDAR". *Publications of the Astronomical Society of the Pacific*, **110**(743): 86-91.

41. Fuensalida, J.J. [et al.]. 2004. An automatically controlled SCIDAR instrument for Roque de los Muchachos Observatory. *Second Backaskog Workshop on Extremely Large Telescopes. Proceedings of the SPIE*, **5382**: 643-647.

42. Garrat, J.R. 1992. *The atmospheric boundary layer. Cambridge atmospheric and space science series.* Cambridge: Cambridge University Press, 1992.

43. Grant, A.L.M. 1992. The structure of turbulence in the near-neutral atmospheric boundary layer. *Journal of the Atmospheric Sciences* **49**: 226-239.

44. Howell, S.B. 2006. *Handbook of CCD Astronomy*. Cambridge: Cambridge University Press, 2006.

45. Kolmogorov, A.N. 1941. The local structure of turbulence in incompressible viscous fluid for very large Reynolds' numbers. *Comptes rendes (Doklady) de l'Academie des Sciences de l'USSR* **30**: 301-305.

46. Kornilov, V. [et al.]. 2003. MASS: a monitor of the vertical turbulence distribution. *Adaptive Optical System Technologies II. Proceedings of the SPIE*, **4839**: 837-845.

47. Kornilov, V. [et al.]. 2007. Combined MASS-DIMM instruments for atmospheric turbulence studies. *Monthly Notices of the Royal Astronomical Society*, **382**: 1268-1278.

48. Kruger, A. C. 2004. *Climate of South Africa. Climate Regions. WS45.* South African Weather Service. Pretoria. South Africa.

49. Lawrence, J.S. [et al.]. 2007. Characterisation of the Dome C atmospheric boundary layer turbulence with a non-Doppler acoustic radar. *EAS Publications Series*, **25**: 31-34.

50. Léna, P. 1986. *Observational astrophysics*. Berlin: Springer-Verlag, 1986.

51. Longair, M.S. 1992. *High energy astrophysics: particles, photons and their detection.* 2nd ed. New York: Cambridge University Press, 1992.

52. Martin, F. [et al.]. 1994. GSM: a Grating Scale Monitor for atmospheric turbulence measurements: I. The instrument and first results of angle of arrival measurements. *Astronomy and Astrophysics Supplement Series*, **108**: 173-180.

53. Martinez, P. & Klotz, A. 1998. *A Practical Guide to CCD Astronomy*. Cambridge: Cambridge University Press, 1998.

54. Mobberley, M. 1998. *Astronomical Equipment for Amateurs*. London: Springer-Verlag, 1998.

55. Moeng, C.-H. and Sullivan, P.P. 1994. A comparison of shear- and buoyancy-driven planetary boundary layer flows. *Journal of the Atmospheric Sciences*, **51**(7): 999-1022.

56. Moore, A. [et al.]. 2006. Ground-layer turbulence profiling using a lunar SHABAR. *Ground-based and Airborne Telescopes. Proceedings of the SPIE*, **6269**: 62695U.

57. Napier-Munn, T. 2008. A mathematical model to predict the resolution of double stars by amateurs and their telescopes. *Journal of Double Star Observations* **4**(4): 156-163.

58. Nappo, C.J. 1991. Sporadic breakdowns of stability in the PBL over simple and complex terrain. *Boundary-Layer Meteorology* **54**(1-2): 69-87.

59. Obukhov, A.M. 1941. On the Distribution of Energy in the Spectrum of Turbulent Flow. *Doklady Akad. Nauk SSSR* **32**(1): 19-24.

60. Pope, S.B. 2000. *Turbulent flows*. Cambridge: Cambridge University Press, 2000.

61. Osborn, J. [et al.]. 2010. Profiling the surface layer of optical turbulence with SLODAR. *Monthly Notices of the Royal Astronomical Society*, **406**: 1405-1408.

62. Robert, C. [et al.]. 2009. C_n^2 profile from Shack-Hartmann data: first steps for CO-SLIDAR data processing. *Optical turbulence: astronomy meets meteorology. Proceedings of the optical turbulence characterization for astronomical applications*. Sardinia, Italy, 15 - 18 September 2008: 74-81.

63. Robert, C. [et al.]. 2011. *C_n^2 profile from Shack-Hartmann data with CO-SLIDAR data processing.* eprint arXiv:1101.3924. Available at: http://arxiv.org/abs/1101.3924 (accessed 10 October 2012).

64. Rocca, A, Roddier, F. and Vernin, J. 1974. Detection of atmospheric turbulent layers by spatiotemporal and spatioangular correlation measurements of stellar-light scintillation. *Journal of the Optical Society of America*, **64**(7): 1000-1004.

65. Roddier, F. 1981. *The effects of atmospheric turbulence in optical astronomy.* Progress in Optics. Amsterdam: North Holland Publishing, **19**: 283-376.

66. Roggeman, M.C. and Welsh, B. 1996. *Imaging through turbulence*. Boca Raton: CRC Press, 1996.

67. Sánchez, L.J. [et al.]. 2003. San Pedro Mártir: Astronomical Site Evaluation. *Astronomical Site Evaluation. Revista Mexicana de Astronomía y Astrofísica. Serie de Conferencias*, **19**: 23-30.

68. Sarazin, M. and Roddier, F. 1990. The ESO differential image motion monitor. *Astronomy and Astrophysics*, **227**: 294-300.

69. Sliepen, G. [et al.]. 2010. Seeing measurements with autonomous, short-baseline shadow band rangers. *Ground-based and Airborne Telescopes III. Proceedings of the SPIE*, **7733**: 77334L-77334L-11.

70. Starizona. 2000. *Starizona's Guide to CCD Imaging*. Available at: http://starizona.com/acb/ ccd/ccd.aspx (accessed 7 May 2012).

71. Stull, R.B. 1988. *An introduction to boundary layer meteorology*. Dordrecht: Kluwer Academic Publishers, 1988.

72. Tatarski, V.I. 1961. *Wave propagation in a turbulent medium*. New York: Dover Publications, 1961.

73. *The Sixth Catalog of Orbits of Visual Binary Stars*. 2006. 6th ed. , Washington, DC: U.S. Naval Observatory, 2006. Available at: http://ad.usno.navy.mil/wds/orb6/orb6ephem.html (accessed 15 April 2012).

74. Tokovinin, A. [et al.]. 2003. Restoration of turbulence profile from scintillation indices. *Monthly Notices for the Royal Astronomical Society*, **343**: 891-899.

75. Tokovinin, A. 2007. Turbulence profiles from the scintillation of stars, planets, and moon. *Workshop on Astronomical Site Evaluation. Revista Mexicana de Astronomía y Astrofísica. Serie de Conferencias*, **31**: 61-70.

76. Tokovinin, A., Bustos, E. and Berdja, A. 2010. Near-ground turbulence profiles from lunar scintillometer. *Monthly Notice of the Royal Astronomical Society*, **404**: 1186-1196.

77. Travouillon, T. 2004. *Optical turbulence on the Antarctic plateau*. September, 2004 [PhD thesis].

78. Trinquet, H. and Vernin, J. 2006. A model to forecast seeing and estimate C_N^2 profiles from meteorological data. *Publications of the Astronomical Society of the Pacific* **118**, 756-764.

79. Trinquet, H. [et al.]. 2008. Nighttime Optical Turbulence Vertical Structure above Dome C in Antarctica. *Publications of the Astronomical Society of the Pacific*, **120**: 203-211.

80. Tubbs, R.N. 2003. *Lucky exposures: diffraction limited astronomical imaging through the atmosphere*. September, 2003 [PhD thesis].

81. Védrenne, N. [et al.]. 2007. C_n^2 profile measurement from Shack-Hartmann data. *Optics Letters*, **32**(18): 2659-2661.

82. Vernin, J. and Muñoz-Tuñón, C. 1992. Optical seeing at La Palma Observatory, I. General guidelines and preliminary results at the Nordic Optical Telescope. *Astronomy & Astrophysics* **257**: 811-816.

83. Vernin, J. and Muñoz-Tuñón, C. 1995. Measuring astronomical seeing: the DA/IAC DIMM. *Publications of the Astronomical Society of the Pacific*, **107**: 265-272.

84. Vernin, J. and Roddier, F. 1973. Experimental determination of two-dimensional spatiotemporal power spectra of stellar light scintillation. Evidence for a multilayer structure of the air turbulence in the upper troposphere. Journal *of the Optical Society of America*, **63**(3): 270-273.

85. Wargau, W.F. 1994. Comparing seeing measurements at SAAO/Sutherland, Gamsberg/Namibia and ESO/La Silla. *Monthly Notices of the Astronomical Society of Southern Africa* **53** (9 & 10): 88-89.

86. Wilson, R.W. 2002. SLODAR: measuring optical turbulence altitude with a Shack-Hartmann wavefront sensor. *Monthly Notice of the Royal Astronomical Society*, **337**(1): 103-108.

87. Wilson,R.W., Butterley, T. and Sarazin, M. 2009. The Durham/ESO SLODAR optical turbulence profiler. *Monthly Notices of the Royal Astronomical Society*, **399**(4): 2129-2138.

88. Wilson, R.W., Butterley, T. and Osborn, J. 2009. Slodar Turbulence Monitors. *Optical turbulence: astronomy meets meteorology. Proceedings of the optical turbulence characterization for astronomical applications*. Sardinia, Italy, 15 - 18 September 2008: 50-57.

89. Wodaski, R. 2002. *The New CCD Astronomy.* Washington: New Astronomy Press, 2002.

90. Ziad, A., [et al.]. 2000. From the Grating Scale Monitor to the Generalized Seeing Monitor. *Applied Optics*, **39**(30): 5415-5425.

91. Ziad, A. [et al.]. 2010. Monitoring of the atmospheric turbulence profiles for the specification of ELT's adaptive optics systems. *Ground-based and Airborne Telescopes III. Proceedings of the SPIE*, **7733**: 77334J-77334J-7.

Appendix A1

Potential sites for locating a new fundamental space geodetic observatory are briefly described referring to factors influencing atmospheric turbulence / astronomical seeing at a site, such as climate, topography and vegetation with reference to Breedlove & Jordaan (2000) and Kruger (2004) –
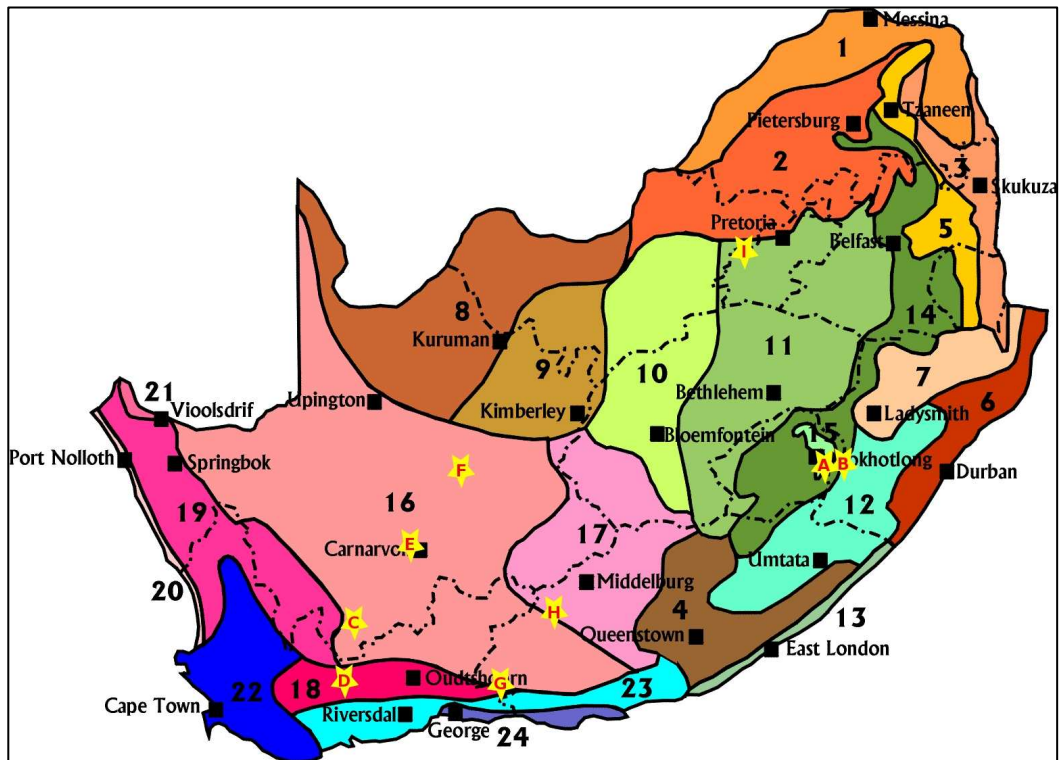
Figure A1.1. Potential sites for a new fundamental space geodetic observatory (and the climatic regions of South Africa in which they are located) (source: Kruger, 2004).

1 Northern Arid Bushveld 2 Central Bushveld 3 Lowveld Bushveld 4 South-Eastern Thornveld 5 Lowveld Mountain Bushveld 6 Eastern Coastal Bushveld 7 KwaZulu-Natal Central Bushveld 8 Kalahari Bushveld 9 Kalaharu Hardveld Bushveld 10 Dry Highveld Grassland 11 Moist Highveld Grassland 12 Eastern Grassland 13 South-Eastern Coast Grassland 14 Eastern Mountain Grassland 15 Alpine Heathland 16 Great and Upper Karoo 17 Eastern Karoo 18 Little Karoo 19 Western Karoo 20 West Coast 21 North-Western Desert 22 Southern Cape Forest 23 South-Western Cape 24 Southern Cape.

- Lesotho [A]: The first site identified and investigated was in Lesotho at 3300 m above sea level. The initial costs for infrastructure were far too high however (Combrinck & Combrink, 2004 and Combrinck *et al*., 2007).

- Underbergh/Shaleburn [B]: Since the Lesotho site is not viable, an area in and around Underbergh has come under investigation. Shaleburn weather station is located in KwaZulu-Natal, ~ 15 km west of Underbergh, at the foot of the Drakensberg. It is

surrounded by the mountains of the Great Escarpment with elevations of between 1500 and 3000 m. It lies on the Eastern Plateau Slope at an elevation of 1609 m. It is in an area of lowlands with high and low mountains and strongly undulating irregular land. Grassland and cultivated land covers the area. It lies on the border of the alpine heathland and eastern grassland climate region. Rainfall is high and occurs mainly during the summer, peaking between December and February.

- Sutherland [C]: The South African Astronomical Observatory (SAAO) site at Sutherland was also considered. Sutherland is located in the southern Northern Cape. The site is located on the interior plain at an elevation of ~ 1760 m. Mountains and lowlands with shrubland predominate. It falls in the Great and Upper Karoo climate region of South Africa. It is a dry and extreme climate. Rainfall is autumnal. In winter, temperatures are very low and the wind comes from the north. In summer, temperatures are high and the wind comes from the south-west. Concerns were raised about the laser (from the laser ranger) causing too much light pollution (Combrinck & Combrink, 2004 and Combrinck *et al*., 2007). Astronomical seeing is determined by the Differential Image Motion Monitoring (DIMM) technique at SAAO. It would be ideal to compare seeing monitor and DIMM measurements at this site. Future collaboration with SAAO is to be continued.

- Matjiesfontein [D]: A valley just 4 km south of Matjiesfontein was identified next. The Matjiesfontein Village Educational Trust indicated that they will donate this piece of land for the use of a space geodetic observatory. Matjiesfontein is located in the Western Cape, ~ 100 km south of Sutherland, in close proximity to SAAO facilities. The site is at elevations between 800 and 1500 m and forms part of the Cape Fold region (Witteberge). It is surrounded by low mountains and lowlands with parallel hills. Land cover consists of shrubland and fynbos. It falls in the Little Karoo climate region of South Africa with low autumnal rainfall. The site provides clear skies (low cloud cover and water vapour content) and infrastructure (close to N1 and railway station, gravel road to site, overhead high voltage line ~ 1 km from site, new water source nearby, small local community) and is accessible. It is located in a small depression shielding it from RFI. The Council for Geoscience conducted geophysical and geotechnical site surveys, which included a magnetic, electromagnetic and seismic

refraction survey. The site meets criteria for site stability. Preliminary astronomical seeing measurements indicated that seeing at the site was comparable to that of Sutherland. The technique employed a small telescope to resolve features on the Moon with known angular separation. This delivered periods of good seeing (1-2 arc-sec) (Combrinck *et al*., 2007).

Figure A1.2. Panoramic view – Matjiesfontein site (courtesy: Roelf Botha).

Figure A1.3. From left to right: Matjiesfontein site – looking north towards proposed LLR location on ridge; on-site Davis Vantage Pro2 Automatic Weather Station (AWS); looking southeast from the LLR ridge down into the valley.

- Klerefontein [E]: The most recently proposed location is the Karoo Array Telescope (KAT) / Square Kilometre Array (SKA) base-station at Klerefontein, which lies 10 km west of Carnarvon in the Northern Cape and ~ 190 km northeast of Sutherland. The site is at an elevation of ~ 1300 m. It forms part of the central interior plain with lowlands and parallel hills. Land cover consists of shrubland. It falls in the Great and Upper Karoo climate region. This site offers the necessary infrastructure (roads, electrical mains power, high-speed fibre-optic link, support facilities, accommodation) without any additional expense to HartRAO. Locating a HartRAO outstation at the KAT/SKA base-station should also promote synergy with the MeerKAT project. The Space Geodesy programme has already been tasked with installing a weather station and GNSS receiver at the site in support of observations made by the C-Band All Sky Survey (C-BASS) telescope located there. Klerefontein is situated in the Astronomy Geographic Advantage Protection (AGAP) zone, which precludes locating an S/LLR

3

with aircraft detection by radar at the site. It would therefore be necessary to furbish any S/LLR system intended for Klerefontein with optical aircraft detection. A Russian SLR system, which HartRAO has been asked to host, uses optical aircraft tracking, and Klerefontein would therefore be an ideal location to place such a system.

- Prieska [F]: Hilly areas to the north and south of Prieska came under consideration due to the extremely low cloud cover at this locality. Prieska is located in the Northern Cape ~ 160 km northeast of Klerefontein. It lies on the interior pre-Karoo surface with hills and slightly irregular plains dominating the landscape. The elevation varies between ~ 1200 and 1400 m. Land cover consists of shrubland thicket and bushland. Similar to Sutherland and Klerefontein, it falls in the Great and Upper Karoo climate region.

- Willowmore [G]: Hilly and mountainous areas encircle Willowmore, which is located in the Eastern Cape ~ 270 km east of Matjiesfontein. The elevation varies between ~ 800 and 1500 m. It forms part of the Cape Fold region with both high and low mountains as well as lowlands with parallel hills occurring. Shrubland and fynbos make up the degraded land cover. The area is ~ 80 km from the Indian Ocean where the climate regions of the Little, Great and Upper Karoo as well as South Western Cape meet.

- Graaff-Reinet [H]: This Eastern Cape town is located ~ 160 km northeast of Willowmore. It forms part of the mountains of the Great Escarpment. A mountainous region, starting to the east of Graaff-Reinet and sweeping through an arc to the southwest, surrounds the town. Shrubland, fynbos and grassland provide degraded land cover. Climate regions of the Great and Upper Karoo as well as Eastern Karoo meet here. The Eastern Karoo is a wetter region than the Great and Upper Karoo and the late-summer to autumn rainfall season peaks from February to March.

In comparing the above sites for water vapour, rainfall and cloud cover (data from http://disc.sci.gsfc.nasa.gov/AIRS as well as www.weathersa.co.za), Shaleburn and Sutherland have the least amount of water vapour, Matjiesfontein and Klerefontein the lowest annual rainfall, while Klerefontein and Prieska have the least amount of cloud cover.

HartRAO [I] will be employed as reference and test site. HartRAO is located ~ 50 km northwest of Johannesburg, just inside Gauteng's border with Northwest Province. HartRAO lies in the central highlands at an elevation of ~ 1380 m with highly dissected and undulating parallel hills as well as lowlands surrounding it. Land cover consists of thicket and bushland, woodland as well as grassland. The regional climate is moist highveld grassland bordering on central bushveld. Rainfall maximum occurs during December and January. The 1-m OCA telescope will be refurbished at HartRAO in a movable structure that is being built on-site for housing the entire S/LLR system in the end. On completion, the S/LLR system will be relocated to the chosen site for the new fundamental space geodetic station.

Appendix A2

An Octave program, 'plot_CN2_notlog_8.m' below, was written and used to calculate $C_N^2(h)$ from the $C_T^2(h)$ profile as well as temperature $T(h)$ and pressure $P(h)$ profiles. The C_T^2 parameter was calculated from rates of temperature variance dissipation ε_θ and turbulence kinetic energy dissipation $\varepsilon^{-\frac{1}{3}}$ by calling the Octave program, 'dissipationLES64.m' also given below, provided by Dr Esau from NERSC.

plot_CN2_notlog_8.m
```
%
% calculate CN2 from Gladstone law (CT2) making use of relative humidity (RH) and
gradtheta
clear;
unorgb=[1 1 1];
% temperature at Matjies [K] (=10 C)
Tbase=283;
% pressure at Matjies in Pa (convert back to hPa/mbar before using in Gladstone's
equation)
Pbase=90500;
% relative humidity (ratio of actual mixing ratio,r, to saturation mixing ratio, xs)
RH=70;
% constant? in Classius Clapeyron equation
eps=0.622
% heat of vaporisation of water (latent heat: water vapour) [J/kg]
Hv=2.257e6
% universal gas constant [J/(kmol.K)]
R=8310
% Specific gas constant [J/(kg.K)]: dry air - sd, water vapour - sw
Rsd=287.052;
Rsw=462;
% Specific heat [J/(kg.K)]: air - a, water vapour - w
%Cpa=1004;
Cpd=1004;
Cpw=1840;
%gravitational acceleration [m/s2]
g=9.8076;
% pressure constant in Gladstone relation [hPa]=[100 Pa]
Pg=80e-6;
% wavelength of green laser light [m]
lamda=532e-9;
%% load database64
load -mat DATABASE64_16hr_final.bin;
load -mat DATABASE64_16hr_final_3D.bin;
% select only tst cases
```

```
ind_tst=[indexdb.tst_begin:indexdb.tst_finish]; nn_total=numel(ind_tst);
q=squeeze(db(ind_tst)); q3=squeeze(d3(ind_tst));
clear db d3;
% calculate spectral dissipations1
for ii=1:nn_total;
   dq(ii)=dissipationLES64(q(ii),q3(ii),4,20,11,2);
end;
%
% initialize total CN2 for summing and calculating q1
CN2total=0;
%initialize q's for summing
q_1total=0;
q_2total=0;
q_3total=0;
q_4total=0;
q_5total=0;
% surface Monin-Obukhov length scale [m] (Ls-von Karman const)
%Ls=18.5885;
psi=1-(2.5*(q(8).z(2)/q(8).Ls(32)));
% surface temperature, T1 [K] (ts-theta star; kappa-temperature scale [K]; surface
roughness [m])
T(1)=Tbase-(q(8).ts(32)/q(8).kappa)*((log(q(8).z(2)/(2*q(8).z0)))-psi);
% surface pressure
P(1)=Pbase;
% CT2 at surface
CT2(1)=1.6*(dq(8).mt_mean_rdissEt)(1).*(dq(8).mt_mean_rdissEk.^(-1/3))(1);
% CN2 at surface
CN2(1)=((Pg*(P(1)/100)/((T(1))^2))^2)*CT2(1);
%
for k=1:63;
% saturated vapour pressure (depends on T (not a constant T0) so therefore variable?)
es(k)=611*exp((eps*Hv/Rsd)*((1/273)-(1/(T(k)))));
% saturation mixing ratio (depends on es (not constant T0) and P (not constant P0) so
therefore also variable?)
xs(k)=eps*(es(k))/(P(k));
% actual mixing ratio from RH and xs (saturated mixing ratio)
r(k)=(RH/100)*(xs(k));
% adiabatic rate
gamma(k)=g*(1+((Hv*(r(k)))/(Rsd*(T(k)))))/(Cpd+((Hv^2)*(r(k))*eps/(Rsd*((T(k))^2)))
;
% temperature profile
T(k+1)=T(k)+(((q(8).gradT(k,32))+gamma(k))*(dq(8).z(k)-dq(8).z(k+1)));
% pressure profile
P(k+1)=P(k)-g*(dq(8).z(k+1)-dq(8).z(k))*(P(k)/(Rsd*T(k)));
%CT2 from dissipations
CT2(k+1)=1.6*(dq(8).mt_mean_rdissEt)(k+1).*(dq(8).mt_mean_rdissEk.^(-1/3))(k+1);
%CN2 profile from Gladstone's relation
CN2(k+1)=((Pg*(P(k+1)/100)/((T(k+1))^2))^2)*CT2(k+1);
CN2total=CN2total+CN2(k+1);
% q's
```

```
q_1(k)=CN2(k+1);
q_2(k)=q_1(k)*((dq(8).z(k))^(5/3));
q_3(k)=q_1(k)*((dq(8).z(k))^(5/6));
q_4(k)=q_1(k)*((q(8).absU(k,32))^(5/3));
q_5(k)=q(8).uu(k,32)/q(8).Nbv(k,32);
% q's summed
q_1total=q_1total+q_1(k);
q_2total=q_2total+q_2(k);
q_3total=q_3total+q_3(k);
q_4total=q_4total+q_4(k);
q_5total=q_5total+q_5(k);
end;
% Integrals
I1=q_1total;
I2=q_2total;
I3=q_3total;
I4=q_4total;
I5=real(q_5total);
% Seeing parameters
r0=(0.423*((2*pi/lamda)^2)* I1)^(-3/5);      % Fried parameter [m]
epsilonFWHM=0.98*lamda/r0;              % Seeing (FWHM) [radian]
hAO=(I2/I1)^(3/5);                 % Seeing layer [m]
thetaAO=0.31*r0/hAO;                  % isoplanatic angle [radian]
sigmaI_sq=19.12*(lamda^(-7/6))*I3;        % scintillation rate [%]
vAO=(I4/I1)^(3/5);                % wave front parameter [m/s]
tauAO=0.31*r0/vAO;                  % coherent wave front time [s]
fG=1/tauAO;                 % Greenwood frequency
epsilonTOT=5.41*(lamda^(-1/5))*((I1)^(3/5)); % median seeing in whole atmosphere
L0=(I5/I1)^(-3)                 % Special coherence outer scale (Nbv
                        - Brunt-Vaisala frequency [1/s],
                         % uu  - total <U'U'> [m2/s2])
figure;
% P profile
%plot((P(1:end)/100),dq(1).z(1:end),'g-','LineWidth',2); hold on;
%xlabel('Pressure [hPa]'); ylabel('z [m]');
%grid;
%print('-dpng','P1_CN2_from_CT2_humidity_gradtheta_test_1.png');
%print('-depsc','P1_CN2_from_CT2_humidity_gradtheta_test_1.eps');
%semilogx(q(1).gradT(:,32), dq(1).z(1:end),'m-','LineWidth',2); hold on;
%xlabel('d{\theta}/dz'); ylabel('z [m]');
% T profile
%plot(T(1:end),dq(1).z(1:end),'c-','LineWidth',2); hold on;
%xlabel('Temperature [K]'); ylabel('z [m]');
% CN2 profile
plot(CN2(1:end),dq(1).z(1:end),'r-','LineWidth',2); hold on;
% CT2 profile - dissipations
%semilogx(CT2(1:end),dq(1).z(1:end),'b-','LineWidth',2); hold on;
xlabel('C_{\fontsize{10}_N}^{2}'); ylabel('z [m]');
%semilogx(dq(1).mt_mean_rdissEt,dq(1).z,'g-','LineWidth',2); hold on;
%semilogx(dq(1).mt_mean_rdissEk,dq(1).z,'c-','LineWidth',2); hold on;
```

```
print('-dpng','CN2_notlog_8.png');
print('-depsc','CN2_notlog_8.eps');
```

dissipationLES64.m
```
function d=dissipationLES64(q,q3,nv,dbin,navr,tint);
% d=dissipationLES64(q,q3,nv,dbin,navr,tint);
% calculate the structure with dissipation and related characteristics
% from LESNIC database 64
% dbin - number of averaging intervals for spectra approximation
% navr - number of bins in Kolmogorov subrange of scale
% tint - number of samples in time averaging
%% Set up common data
d.file_name=q.fname;
d.nx=q.ndim(1); d.ny=q.ndim(2); d.nz=q.ndim(3); d.nv=q.ndim(5); d.nt=q.ndim(4);
d.tint=tint;
d.lx=q3.ldim(1); d.ly=q3.ldim(1); d.fac=q3.ldim(1)/q3.ndim(1);
d.dbin=dbin; d.navr=navr;
nx=d.nx; nz=d.nz;
b=9.81/300;
nt=numel([q.u(1,:)]); TT=[nt-tint+1:nt];
d.z=q.z;
d.mt_u=squeeze(mean(q.u(:,TT),2));                    d.mt_v=squeeze(mean(q.v(:,TT),2));
d.mt_absU=abs(d.mt_u+i*d.mt_v);
d.mt_gradU=gradient(d.mt_absU,d.z');
d.mt_gradu=gradient(d.mt_u,d.z'); d.mt_gradv=gradient(d.mt_v,d.z');
d.mt_t13(1:nz-1)=squeeze(mean(q.uw(2:nz,TT),2));
d.mt_t23(1:nz-1)=squeeze(mean(q.vw(2:nz,TT),2));
d.mt_t13(nz)=d.mt_t13(nz-1); d.mt_t23(nz)=d.mt_t23(nz-1);
d.mt_us=sqrt(abs(d.mt_t13+i*d.mt_t23));
d.mt_mean_rdissEk=max(0,abs([d.mt_t13]'.*d.mt_gradu+i*([d.mt_t23]'.*d.mt_gradv)));
if (nv>3);  % calculate potential energy dissipation
   d.mt_th=squeeze(mean(q.absT(:,TT),2));
   d.mt_gradT=gradient(d.mt_th,d.z');
   d.mt_rN=sqrt(b*d.mt_gradT);
   d.mt_wt(1:nz-1)=squeeze(mean(q.wt(2:nz,TT),2));
   d.mt_wt(nz)=d.mt_wt(nz-1);
   d.mt_mean_rdissEk=max(1e-12,d.mt_mean_rdissEk+b*[d.mt_wt]');
   d.mt_mean_rdissEt=max(1e-12,-[d.mt_wt]'.*d.mt_gradT);
   d.mt_mean_rRig=b*d.mt_gradT./d.mt_gradU.^2;
%                                                          d.mt_mean_rRifd=-
b*d.mt_wt./abs(d.mt_t13.*[d.mt_gradu]'+i*(d.mt_t23.*[d.mt_gradv]'));
   d.mt_mean_rRifd=-
b*d.mt_wt./(abs(d.mt_t13+i*d.mt_t23).*abs([d.mt_gradu]'+i*[d.mt_gradv]'));
   d.mt_mean_rN=d.mt_rN;
   d.mt_mean_rL=-sqrt(abs(d.mt_t13+i*d.mt_t23)).^3./(b*d.mt_wt);
   d.mt_mean_rdissEp=d.mt_mean_rdissEt.*(b./d.mt_mean_rN).^2;
   d.mt_mean_rRif=d.mt_mean_rdissEp./(d.mt_mean_rdissEk+d.mt_mean_rdissEp);
else
   d.mt_th=d.mt_u*nan; d.mt_N=d.mt_th; d.mt_gradT=d.mt_th;
```

```
    d.mt_wt=d.mt_t13*nan; d.mt_mean_rL=d.mt_wt;
    d.mt_mean_rRig=d.mt_mean_rdissEk; d.mt_mean_rRifd=d.mt_mean_rdissEk;
    d.mt_mean_rdissEt=d.mt_mean_rRig; d.mt_mean_rN=d.mt_mean_rRig;
    d.mt_mean_rdissEp=d.mt_mean_rdissEt;
    d.mt_mean_rRif=d.mt_mean_rdissEp;
end;
% find the turbulent PBL depth
ind=min(nx,min(find([d.mt_us].^2<0.05*[d.mt_us(1)].^2)+1));
d.mt_rHtau05=d.z(ind); d.mt_iHtau05=ind;
%% Second step: spectral dissipation from Kolmogorov interval of scales
disp(['Read ' d.file_name]);
Z1=[floor(1/5*d.mt_iHtau05):round(2/3*d.mt_iHtau05)];
x(:,:,:,1)=[q3.u3d];
x(:,:,:,2)=[q3.v3d];
x(:,:,:,3)=[q3.w3d];
x(:,:,:,4)=[q3.t3d];
ny=numel(squeeze(x(1,:,1,1))); d.ny_used=ny;
NFFT = 2^nextpow2(nx); % Next power of 2 from length of y
K = d.fac/2*linspace(0,1,NFFT/2);
Kx = [0:1:NFFT/2-1]; d.Kx=Kx; d.nKx=numel(Kx); nKx=d.nKx;
% obtain dissipation on each level
% interpolate the vertical velocity on U levels
for iz=2:nz; x(:,:,iz-1,3)=0.5*(x(:,:,iz,3)+x(:,:,iz-1,3)); end;
% calculate anomalies
xm=squeeze(mean(mean(x,2),1));   for iv=1:nv;   for iz=1:nz;   xa(:,:,iz,iv)=x(:,:,iz,iv)-
xm(iz,iv); end; end;
% calculate turbulent energy and velocity variations
e=squeeze(0.5*(xa(:,:,:,1).^2+xa(:,:,:,2).^2+xa(:,:,:,3).^2));
sex=squeeze(2*abs(fft(e,NFFT,1)/nx)); % absolute values of the energy spectra in x
(streamwise) direction
disp('Calculate TKE dissipation');
for iz=1:nz;
   icmp=floor(iz/nz*100); if (mod(icmp,20)==0); disp(['Completed ' num2str(icmp) '%']);
end;
   for iy=1:ny; disx(:,iy,iz)=(sex(Kx+1,iy,iz)'.*K.^(5/3)).^(3/2); end;
   d.last_u(iz)=squeeze(mean(mean(x(:,:,iz,1),2),1));
   d.last_v(iz)=squeeze(mean(mean(x(:,:,iz,2),2),1));
   d.last_U(iz)=squeeze(mean(mean(abs(x(:,:,iz,1)+i*x(:,:,iz,2)),2),1));
   d.last_t13(iz)=squeeze(mean(mean(xa(:,:,iz,1).*xa(:,:,iz,3),2),1));
   d.last_t23(iz)=squeeze(mean(mean(xa(:,:,iz,2).*xa(:,:,iz,3),2),1));
   d.last_Ek(iz)=squeeze(mean(mean(e(:,:,iz),2),1));
end;
d.last_gradu=gradient(d.last_u,d.z');
d.last_gradv=gradient(d.last_v,d.z');
d.last_gradU=gradient(d.last_U,d.z');
d.last_us=sqrt(abs(d.last_t13+i*d.last_t23));
[d.kx,d.dissEk,d.last_dissEk,d.factor_dissEk]=aggregation(nKx,dbin,navr,disx,d.mt_mean
_rdissEk,Z1);
%
if (nv>3);
```

% calculate temperature fluctuations spectra along x
```
tt=0.5*xa(:,:,:,4).^2;
stx=squeeze(2*abs(fft(tt,NFFT,1)/nx)); % absolute values of the energy spectra in x
```
(streamwise) direction
```
disp('Calculate TPE dissipation');
for iz=1:nz;
    icmp=floor(iz/nz*100); if (mod(icmp,20)==0); disp(['Completed ' num2str(icmp)
'%']); end;
    for iy=1:ny; dtx(:,iy,iz)=(stx(Kx+1,iy,iz).*(disx(:,iy,iz)).^(1/3))'.*K.^(5/3); end;
    d.last_wt(iz)=squeeze(mean(mean(xa(:,:,iz,4).*xa(:,:,iz,3),2),1));
    d.last_th(iz)=squeeze(mean(mean(x(:,:,iz,4),2),1));
    d.last_Et(iz)=squeeze(mean(mean(tt(:,:,iz),2),1));
end;
d.last_gradT=gradient(d.last_th,d.z');
d.last_N=sqrt(b*d.last_gradT+1e-6);
d.last_Ep=d.last_Et.*(b./d.last_N).^2;
d.last_L=-abs(d.last_t13+i*d.last_t23).^(3/2)./(b*d.last_wt+1e-6);

[d.kx,d.dissEt,d.last_dissEt,d.factor_dissEt]=aggregation(nKx,dbin,navr,dtx,d.mt_mean_rd
issEt,Z1);
```
% calculate own Rig
```
d.last_Rig=[d.last_N].^2./[d.last_gradU].^2;
d.last_Rifd=-b*d.last_wt./abs(d.last_t13.*d.last_gradu+i*(d.last_t23.*d.last_gradv));
d.last_dissEp=d.last_dissEt.*(b./[d.last_N]).^2;
d.last_Rif=d.last_dissEp./(d.last_dissEk+d.last_dissEp);
else
    d.factor_dissEt=nan; % const
    d.dissEt=d.dissEk.*d.factor_dissEt;
    d.last_dissEt=d.last_dissEk.*d.factor_dissEt; d.last_dissEp=d.last_dissEk
    d.last_th=d.last_U*nan; d.last_gradT=d.last_th; d.last_N=d.last_th; d.last_wt=d.last_th;
    d.last_Et=d.last_th; d.last_Ep=d.last_th; d.last_L=d.last_th;
    d.last_Rig=d.last_dissEt; d.last_Rifd=d.last_dissEt;
end;
```
%% Final step: functions
```
function [k,x,mx,factor]=aggregation(nk,dbin,navr,s,r,Z);
```
% local function for aggregation of the results
%
```
Bx=floor(linspace(1,nk,dbin));
for ii=1:dbin-1;
    x1(ii,:,:)=squeeze(mean(s(Bx(ii):Bx(ii+1),:,:),1));
    k(ii)=0.5*(Bx(ii)+Bx(ii+1));
end;
x1(ii+1,:,:)=x1(ii,:,:); k(ii+1)=k(ii);
x=squeeze(mean(x1,2)); avr=min(navr,dbin-2);
mx=squeeze(mean(x(dbin-avr-1:dbin-1,:),1));
factor=mean(r(Z))/mean(mx(Z)); % const
x=x*factor; mx=mx.*factor;
```

Appendix A3

Definition of CCD camera terms:

Bit depth / Analogue to Digital (A/D) resolution - of 16 bits implies that, during analogue-to-digital conversion (ADC), the CCD camera is capable of converting the analogue signal to 2^{16} or 65536 digital steps; bit depths of 8 or 12 might not be capable of utilising the CCD camera's Dynamic Range in full.

Dark Current - is caused by the generation of thermal electrons in the absence of light in the CCD camera itself; it is a function of exposure time and chip temperature and can be reduced by introducing regulated thermo-electric cooling to provide an operating temperature below 0 °C; dark frame calibration removes the effect of dark current from light frames.

Dynamic Range - is a measure of the difference between the highest and lowest intensities, as well as number of steps in between, which a CCD camera is capable of capturing in a single exposure; to obtain the Dynamic Range, divide Full-Well Capacity by Read Noise.

Frame rate – is the inverse of the time it takes to acquire a frame and read it out.

Frame transfer - exposure is controlled by electronic shutter; exposure and readout occur simultaneously; half of the pixel array is masked and used as a storage area while the other half is unmasked and used to collect the image; once the exposure has ended, the charge is rapidly transferred from the unmasked active imaging area to the masked storage area; readout from the storage area may proceed at a slower pace while the next exposure is being captured; high frame rates are possible but resolution is compromised.

Full frame - an electromechanical shutter is built into the CCD camera; when open, charge is accumulated; when closed, charge is transferred and read out; this provides the highest resolution but limits the frame rate.

Full-Well Capacity / Well Depth - is the number of electrons a pixel can store before it becomes saturated.

Interline - exposure is controlled by electronic shutter; alternating columns of active unmasked imaging area and masked storage area occur enabling rapid transfer from imaging area to storage area in adjacent columns; micro-lenses cover imaging and storage pixels in pairs and direct light to imaging pixels; continuous operation and high frame rates are possible but sensitivity (Quantum Efficiency) is compromised.

Linearity - in CCD cameras with a linear response, the reproduced signal increases in direct proportion to the amplitude of the original source.

Monochrome - black and white CCD cameras have higher sensitivity than colour CCD cameras.

Quantum Efficiency - is a measure of the efficiency with which detected photons are converted to electrons.

Read Noise - is generated by the CCD camera's electronics during ADC and is inherent in the sensor; it is the smallest signal that can be captured.

Appendix A4

Techniques and instruments that are currently employed and which have become the accepted standard to characterise and monitor sites with respect to seeing are compared in Table A4.1 and are as follows: balloon-borne radiosondes, instrumented masts, SHABAR (**SHA**dow **BA**nd **R**anging), LuSci (**Lu**nar **Sci**ntillometer), SCIDAR (**SCI**ntillation **D**etection **A**nd **R**anging), G-SCIDAR (**G**eneralised - **SCIDAR**), HVR-GS (**H**igh **V**ertical **R**esolution **G**-SCIDAR), LOLAS (**LO**w **LA**yer **S**CIDAR), SLODAR (**SLO**pe **D**etection **A**nd **R**anging), CO-SLIDAR (**CO**upled – **SL**ODAR SC**IDAR**); SODAR (**SO**nic **D**etection **A**nd **R**anging), SNODAR (**S**urface layer **NO**n-**D**oppler **A**coustic **R**adar), DIMM (**D**ifferential **I**mage **M**otion **M**onitor), MASS (**M**ulti-**A**perture **S**cintillation **S**ensor), MASS-DIMM, GSM (**G**eneralized **S**eeing **M**onitor) and PBL (**P**rofileur **B**ord **L**unaire or Lunar Limb Profiler).

Some instruments lend themselves to short intensive seeing campaigns while others are more appropriate to use as long-term seeing monitors on site. In order to determine whether a particular site would present favourable astronomical seeing conditions, a profile of the turbulence strength as a function of altitude, the $C_N^{\ 2}(h)$ profile, at the site is determined. Measurement of the $C_N^{\ 2}(h)$ profile throughout the PBL may be achieved by means of *in situ* measurements making use of sensors mounted on masts, balloons or even aircraft, or by employing remote sensing techniques based on the detection of light, acoustic or radio waves. *In situ* measurements with instrumented balloons provide high-resolution turbulence profiles from surface layer to free atmosphere but the technique is expensive and cannot be used for long-term site monitoring. The remote sensing instruments employed for turbulence and seeing measurements are usually inexpensive and simple to operate. Instruments used for site characterisation campaigns should additionally be as compact and robust as possible. Different remote sensing techniques are sensitive to different layers of the atmosphere and the techniques also differ in the vertical resolution they are able to achieve.

Table A4.1. Comparison of various seeing techniques / instruments (continued on next page).

Technique	Based on	Measured	Calculated	Vertical resolution	Height	Layer	Portability
Mast[1]	Micro-thermal soundings	$D_T(r)$, $C_T^2(h)$, $P(h)$, $T(h)$, $Rh(h)$, $V(h)$	$C_N^2(h)$, r_0, ε_{SL}	Depends on height intervals of sensors	10 – 50 m	Surface	
Balloon[2]	Micro-thermal soundings	$D_T(r)$, $C_T^2(h)$, $P(h)$, $T(h)$, $Rh(h)$, $V(h)$	$C_N^2(h)$ r_0, ε, θ_0, τ_0	5-10 m $V(h)$: 30-50 m	20 m – 30 km	Entire atmosphere excl. surface (0 – 20 m)	
SHABAR[3]/ LuSci[4]	Solar, lunar scintillation	Scintillation	$C_N^2(h)$, r_0, ε_{GL}		~ 100 – 200 m	Ground	Robotic
SCIDAR[5] G-SCIDAR[6] HVR-GS[7] LOLAS[8]	Binary star scintillation	Scintillation	$C_N^2(h)$, $V(h)$, r_0, ε, θ_0, τ_0	~ 200 m ~ 200 m ~ 25 m 12 m	Up to 25 km 0 – 22 km 0 – 1 km 0 – 1 km	Entire atmosphere excl. ground Entire atmosphere Boundary Boundary	$D_{telescope} \geq 1\,\mathrm{m}$ $D_{telescope} \geq 0.4\,\mathrm{m}$
SLODAR[9]	Binary star wave front slope	Wave front slope	$C_N^2(h)$, $V(h)$, r_0, ε	400-700 m 60 m – 150 m	0 – 18 km 0 – 1 km	Entire atmosphere Boundary	$D_{telescope} \geq 1\,\mathrm{m}$ $D_{telescope} = 0.4\,\mathrm{m}$
CO-SLIDAR[10]	Binary star scintillation + wave front slope	Scintillation + wave front slope	$C_N^2(h)$, r_0, ε		20 km	Entire atmosphere	$D_{telescope} \geq 1\,\mathrm{m}$
SODAR[11] SNODAR[12]	Sound pulse backscatter from turbulence	σ_0, $C_T^2(h)$ Doppler shift of scattered pulse	$C_N^2(h)$, $V(h)$	5 m 20 m 0.9 m	0 – 200 m 20 m – 1 km 8 m – 180 m	Ground Boundary Antarctic boundary	Robust, robotic
DIMM[13]	Differential image motion in twin images of star	Differential image motion variance - σ_l, σ_t	r_0, ε, σ_I^2, θ_0, τ_0	Integrated ε	Entire atmosphere	Entire atmosphere	$D_{telescope} = 8"-14"$ Compact, robust, robotic, site monitoring

Table A4.1. Comparison of various seeing techniques / instruments (continued from previous page).

Technique	Based on	Measured	Calculated	Vertical resolution	Height	Layer	Portability
MASS[14]	Scintillation of light from single star	Intensity fluctuations, scintillation indices	σ_I^2 fit to model provides $C_N^2(h)$, r_0, ε_{FA}, θ_0, τ_0	500 m Limited to six turbulent layers at 0.5, 1, 2, 4, 8 and 16 km in fixed-layer model	Entire atmosphere	Entire armosphere excl. ground (<0.5 km) - only free atmosphere seeing	$D_{telescope}$ = 8 "– 14 " Compact, robust, robotic, continuous site monitoring
MASS-DIMM[15]	Combination of MASS & DIMM	Scintillation indices, differential image motion variance	$C_N^2(h)$, r_0, ε, θ_0, τ_0, σ_I^2	MASS: 500 m DIMM: integrated ε	MASS: entire atmosphere excl. ground DIMM: entire atmosphere	Entire atmosphere + ground-layer seeing from DIMM – MASS: $\varepsilon_{BL} = \left(\varepsilon_{DIMM}^{5/3} - \varepsilon_{MASS}^{5/3}\right)^{3/5}$	Compact, robust, robotic, continuous site monitoring
GSM[16]	Single star Angle of Arrival (AA) fluctuations + scintillation	AA spatio-temporal correlations σ_I^2	ε, $\mathcal{L}_0$, σ_I^2, θ_0, τ_0, $V(h)$				4+ Maksutov telescopes each with $D_{telescope}$ = 10 cm
PBL[17]	DIMM of point along lower lunar limb	Differential image motion variance	$C_N^2(h)$, $\mathcal{L}_0(h)$, θ_0, r_0, ε (15+ layers)	High ε for 15+ layers	Entire atmosphere	Entire atmosphere	$D_{telescope}$ = 16 " (portable version)

1 Echevarría (1998 & 2003); Sánchez (2003)
2 Bufton *et al.* (1972) ; Barletti *et al.* (1977) ; Azouit *et al.* (1980) ; Vernin & Muñoz-Tuñón (1992) ; Azouit & Vernin (2005)
3 Beckers (1993 & 2001); Moore *et al.* (2006); Sliepen *et al.* (2010)
4 Tokovinin (2007); Tokovinin, Bustos & Berdja (2010)
5 Vernin & Roddier (1973); Rocca *et al.* (1974)
6 Avila *et al.* (1997); Fuchs *et al.* (1998)
7 Egner *et al.* (2006); Egner & Masciadri (2007)
8 Avila *et al.* (2008)
9 Wilson (2002 & 2010); Wilson, Butterley & Sarazin (2009); Osborn *et al.* (2010)
10 Védrenne *et al.* (2007) ; Robert *et al.* (2009 & 2011)
11 Crescenti (1997)
12 Lawrence *et al.* (2007) ; Bonner *et al.* (2008, 2009 & 2010)
13 Sarazin & Roddier (1990); Vernin & Muñoz-Tuñón (1995)
14 Kornilov *et al.* (2003) & Tokovinin *et al.* (2003)
15 Kornilov *et al.* (2007)
16 Martin *et al.* (1994); Conan *et al.* (1999a & 1999b); Ziad *et al.* (2000)
17 Ziad *et al.* (2010)

$D_T(r)$: temperature structure function

$C_T^2(h)$, $C_N^2(h)$: temperature and refractive index structure parameters

$P(h)$, $T(h)$, $Rh(h)$, $V(h)$: pressure, temperature, relative humidity, wind profiles

r_0 : Fried parameter

ε, ε_{SL}, ε_{GL} : total, surface layer, ground layer seeing

θ_0 : isoplanatic angle

τ_0 : coherence time

σ_0 : backscatter cross-section

σ_l, σ_t : longitudinal, transverse variation of differential image motion

σ_I^2 : scintillation index

$\mathcal{L}_0(h)$: outer scale of turbulence

Some instruments provide turbulence profiles from ground level to the top of the atmosphere, the so-called vertical turbulence profilers, which are able to provide the vertical distribution of $C_N{}^2(h)$, wind speed as well as the outer scale of turbulence. In contrast, the integrated turbulence monitors are only able to provide integrated values for the seeing. Remote sensing techniques generally also provide the classical Fried parameter and the seeing as well as other seeing parameters such as the isoplanatic angle, coherence time and outer scale of turbulence.

Instrumentation, such as the DIMM, MASS, MASS-DIMM, GSM and PBL, that could become available for use during short seeing campaigns, are described in detail below, as is the necessity of co-locating an AWS and cloud mapper with any on-site seeing monitor:

DIMM

The following discussion of the DIMM instrument is based on descriptions by Sarazin and Roddier (1990) as well as by Vernin and Muñoz-Tuñón (1995):

The DIMM has become the standard instrument for characterising sites with respect to astronomical seeing. It does so by estimating the integrated seeing over the entire atmosphere in the column of air above the telescope. DIMM measures differential image motion variance caused by atmospheric turbulence in two images (two columns of light) taken of the same star at exactly the same moment. Seeing is then related to this variance of differential image motion through use of the Fried parameter. A DIMM is usually a robust set-up, which allows for transportation over rough terrain during site testing campaigns. It consists of a telescope, mount and CCD camera. The telescopes used are commercially available SCTs with apertures ranging from 8" to 14". CCD cameras are inexpensive, off-the-shelf cameras able to provide a fast frame-rate and preferably offering an adjustable electronic shutter. A high-quality equatorial mount and auto-guiding are required for accurate pointing and tracking. A PC and the appropriate software allow for robotic control of the entire system. The telescope entrance pupil is covered by an aperture mask. Oftentimes the telescope's dust cover will have been modified to provide this mask. The mask has two circular sub-apertures cut into it. The sub-apertures vary in diameter

from ~ 5-11 cm and are separated by a distance of a few times the sub-aperture diameter, ~ 14-25 cm, depending on the telescope aperture diameter. A wedge prism is placed in one of the sub-apertures. It displaces the light coming through the sub-aperture. Well-separated twin images of the same star are thus detected by the CCD camera. A beam splitter could also be used to obtain such twin images.

A bright star, less than 30° from zenith, is observed for a few hours while it crosses the meridian. Each sub-aperture observes the star through a different column of air. A wedge prism on one of the sub-apertures allows a second image of the star to be formed by reflection of the light cone going through that sub-aperture. The two star images are

Figure A4.1. DIMM mask with wedge prism (source: Andrei Tokovinin).

detected by the CCD camera, which takes a set of ~ 200-400 short-exposure (~ 2-5 ms) images required to capture the rapid image motion. The variances in differential motions of the two image centroids are measured in directions longitudinal (parallel) and transverse (perpendicular) to the line connecting the centres of the two sub-apertures. Two independent values for the Fried parameter (r_0) are estimated - one related to the variance in longitudinal differential motion (σ_l), the other to the variance in transverse differential motion (σ_t). These two Fried parameter values should be the same but strong winds and finite exposure time will cause them to differ. Seeing (ε) is obtained from the Fried parameter values. Seeing estimates are referred to zenith and corrected for air mass, system noise and statistical errors. Two windows, each containing one of the image centroids, are displayed on-screen, as is the seeing value, FWHM, flux and scintillation index. Seeing

estimations are provided approximately every minute. Guiding takes place between 1-minute data accumulations. The differential technique allows distinguishing between image motion caused by turbulence and that caused by telescope vibrations and tracking errors. DIMM systems have become reliable, cost-effective, portable, easy to set up, operate and maintain and are now well-documented and easy to duplicate. DIMM systems can operate in robotic mode with all functions controlled by computer.

MASS

The MASS instrument is described in accordance with details provided in Kornilov *et al.* (2003) and Tokovinin *et al.* (2003):

MASS is a standard instrument for determining low-resolution atmospheric turbulence profiles above sites. Scintillation (or twinkling) of star light is caused by atmospheric turbulence. Scintillation from the light of a single star is measured in four concentric annular apertures in the image pupil plane. Intensity fluctuations in the four apertures are statistically analysed to provide scintillation indices (SIs). The indices are fitted to a turbulence-layer model and the turbulence profile $C_N^2(h)$ is recovered. MASS is a small, robust instrument fed by a SCT setup with auto-guiding similar to the DIMM setup. A small detector box contains the optics (including a segmentator), photo-multiplier tubes (PMTs) and electronics. The segmentator consists of a circular mirror surrounded by three concentric, reflective rings with varying tilts. It separates the image of the telescope exit pupil into four concentric-ring apertures A, B, C and D with inner and outer diameters ranging from 2 cm (A) to 13 cm (D), respectively. Scintillations are detected in the four concentric-ring apertures by the PMTs operating in photon-counting mode. The control software, Turbina, runs under Linux and controls the instrument through a graphical user interface (GUI) and provides real-time data reduction and automatic operation. A single bright star within 45° of zenith is observed. The flux from the star is spatially filtered by the four concentric-ring apertures. The varying aperture diameters allows for turbulent layers causing the scintillation to be identified and their contribution to the scintillation to be found. Light from each aperture is detected by four PMTs sampling at 1 ms in photon-counting mode. Turbina processes the photon counts and calculates SIs for each aperture every second. SIs for each aperture as well as each aperture pairing are calculated,

delivering four normal and six differential SIs. By knowing the weighting functions (WFs), which represent layer-contributions to SIs, and the SIs themselves, and by fitting these indices to a simple model with a small number of layers, a low vertical resolution (500 m) turbulence profile $C_N^2(h)$ is obtained. The fixed-layer model provides for six thin turbulent layers at 0.5, 1, 2, 4, 8 and 16 km altitude. The floating-layer model provides for three layers located at any altitude. Every minute, average indices are computed and turbulence parameters determined. The Fried parameter (and therefore the seeing) is related to the integral of $C_N^2(h)$ over the whole atmosphere. Near-ground turbulence does not produce any scintillation. MASS is therefore not sensitive to ground-layer turbulence (< 0.5 km). Only free-atmosphere seeing is estimated. The isoplanatic angle (θ_0) is also derived from the turbulence profile. Turbina displays the turbulence evolution on-screen in real time. The MASS has become a simple and inexpensive instrument and can be used as a turbulence profiler for continuous site monitoring.

MASS-DIMM

Kornilov *et al.* (2007) provides the basis for the following discussion of the combined MASS-DIMM instrument:

Ground-layer turbulence is not sensed by MASS as it does not produce any scintillation, whilst DIMM measures the seeing in the atmosphere as a whole. Combining MASS and DIMM, the seeing in the lowest 500 m can be found by subtracting the turbulence integral measured with MASS (free atmosphere seeing) from that measured with DIMM (total integrated seeing). The MASS-DIMM instrument uses the same telescope and observes the same star thereby sensing the same turbulent volume.

The SALT MASS-DIMM instrument is attached to a 10" LX200GPS Meade SCT, the same telescope feeding both MASS and DIMM channels. The telescope is mounted on an Astro-Physics 900 GTO equatorial mount mated to a sturdy pier at ground level. A Grasshopper Pixelfly CCD camera with fast frame-rate capable of taking short exposures is attached to the DIMM channel. DIMM data is processed with TimDIMM software, MASS data with Turbina 2.06 software. The system is controlled by Python script running on a

Mac mini. The MASS-DIMM instrument consists of a small detector box which houses common optics and electronics. Electronics consist of the PMTs, their high-voltage supply, photon counters and microprocessors. The light is split into a MASS channel and a DIMM channel by a pupil plate

Figure A4.2. The SALT MASS-DIMM in operation at the SAAO site in Sutherland with the MASS-DIMM instrument attached at the exit pupil displayed in insert bottom right.

assembly. The light is further separated into four MASS sub-channels by a segmentator and directed to the four PMTs. Two mirrors provide two DIMM sub-channels which direct the light to the CCD camera for detecting the two image centroids of the same star. A single bright star within 30° from zenith is acquired. The DIMM channel is used to centre and guide on the star. TimDIMM and Turbina software are started and seeing measurements made in both DIMM and MASS channels with 1-minute integration time. Measurements are terminated and a new target is acquired once the star moves outside of 30° from zenith. As described in the section above, DIMM measures the differential image motion of the star in the two DIMM sub-channels while MASS measures the scintillation of the same star in the four MASS sub-channels (corresponding to different turbulent layers in the atmosphere). The Fried parameter and thus seeing is estimated from the differential motion measured by the DIMM channel. The DIMM channel delivers total

integrated seeing (Fried parameter) for all layers, from the ground layer up to the free atmosphere, i.e. seeing in the entire atmosphere. From the scintillation indices measured by the MASS channel, a low-resolution turbulence profile is constructed, and seeing from 500 m above the telescope to the top of the atmosphere can be estimated. Ground-layer seeing can thus be determined from the difference between the seeing obtained from DIMM and that obtained from MASS.

The MASS-DIMM instrument is fast becoming the standard seeing monitor to be found at astronomical observatories. It is compact, robust, simple to use and relatively inexpensive and can be fully automated for continuous turbulence monitoring at a site.

GSM

The following discussion of the GSM instrument refers to descriptions in Martin *et al.* (1994), Conan *et al.* (1999a and 1999b) and Ziad *et al.* (2000):

The GSM measures the angle of arrival (AA) fluctuations at different points on the wave front and computes AA spatio-temporal correlations from which the seeing (ε), outer scale of turbulence ($\mathcal{L}_0$), isoplanatic angle (θ_0) and coherence time for the AA fluctuations (τ_0) may be deduced. It consists of several, usually four (providing six baselines), 10-cm aperture diameter Maksutov telescopes installed on equatorial mounts on piers set up in an L-shaped configuration to improve sensitivity to the outer scale. Accompanying each telescope is a detection module housing, optical and detector components. All telescopes observe the same single bright star at zenith angles between 0° and 45°. AA fluctuations are measured by flux modulation (produced by the displacement of the star image over a Ronchi grating) and the transmitted flux is detected by photomultiplier. AA covariances of the AA fluctuations for the various baselines are computed. Two of the telescopes share a mount and pier, operating as a DIMM and measures the AA differential variances from which the seeing (ε) is obtained. The outer scale ($\mathcal{L}_0$) is obtained from the ratio of AA covariances to differential variances. The recorded flux provides the scintillation index (σ_I^2) from which the isoplanatic angle (θ_0)

may be deduced. Wind speed of the turbulent layers is extracted from AA spatio-temporal correlations from which the wave front constant time (τ_0) is deduced.

During the Sutherland campaign, two Maksutov 10-cm aperture diameter telescopes, each with a detection module containing optics and PMT detectors, were set up in a binocular configuration. The GSM modules were mounted on an Astro-Physics 900 GTO equatorial mount mated to a rigid pier at ground level. A single star with magnitude < 3 and within 30° of zenith was observed through both apertures. For each of the modules, a diaphragm filtered out noise from the sky background, the light was aligned by a collimator and directed to an oscillating mirror, which deflected it onto the Ronchi grating and, on passing through the grating, was detected by the PMTs. Without turbulence present, light would produce a regular sine wave as it passes through the grating. With turbulence present, the phase of the sine wave is shifted. From the phase difference, the seeing, isoplanatic angle and outer scale of turbulence were deduced.
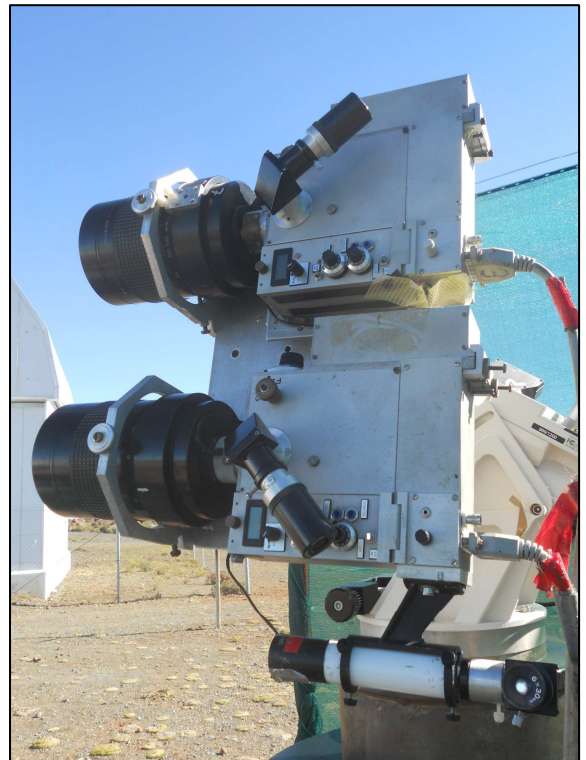

Figure A4.3. The GSM at Sutherland operated in DIMM mode with the two Maksutov telescopes sharing the same mount.

PBL

The PBL instrument is discussed with reference to Ziad *et al*. (2010):

The PBL is a new instrument capable of extracting both $C_N^2(h)$ and $\mathcal{L}_0(h)$ with high vertical resolution. A portable version of the PBL was used for the first time during the Sutherland seeing campaign. The PBL observes the lunar limb using the DIMM method. Equipment consists of a Meade 16M SCT mounted on an Astro-Physics 1200 GTO equatorial mount mated to a sturdy pier. The front aperture of the telescope is covered by a mask with two 6-cm diameter sub-apertures separated by ~ 30 cm. The imaging module contains the optics and a PixelFly CCD camera, which are all mounted on a micro-control plate for adjustment with software.

Figure A4.4. The PBL setup at Sutherland with SALT in the background.
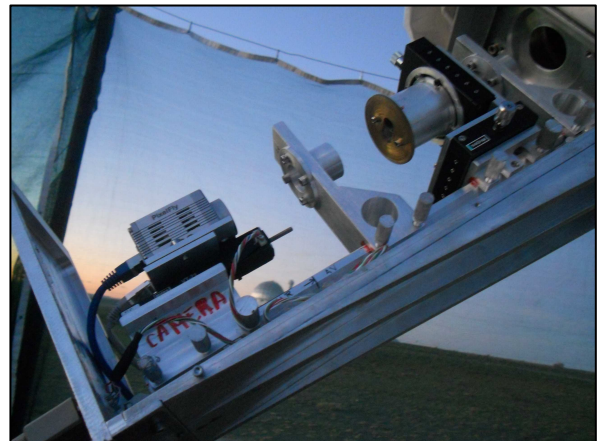

Figure A4.5. The PBL's optical module includes a PixelFly CCD camera.

The CCD camera has an imaging frequency of 33 Hz and its exposure time is set to 1 or 2 ms to freeze image motion. The two sub-apertures in the mask provide two images of the Moon's limb. A Dove prism is used to reverse one of the two images to prevent bright parts from overlapping. Two mirror images of the Moon's lower limb are thus obtained. The two sub-apertures observe the same points along the Moon's limb. Wave fronts arrive at the two sub-apertures from two directions separated by and angle θ. The Moon's limb provides a continuum of point sources with varying angular separation. The PBL measures the differential image motion of all these points along the Moon's limb. The $C_N^2(h)$ profile is retrieved by analysing the angular correlation of the differential distance between

the two lunar edges. The PBL is also capable of providing the outer scale profile, isoplanatic angle and the contribution to the seeing of 15+ layers. As with the DIMM method, the use of differential image motion compensates for telescope vibrations and tracking errors.

Weather station and cloud mapper

A site's atmospheric stability is dependent on minimal variation in air temperature and atmospheric pressure, on low relative humidity, precipitable water vapour, precipitation and wind speed as well as on a high frequency of clear-sky conditions. Knowledge of these parameters' diurnal and seasonal distribution is necessary to fully characterise a site with respect to meteorological and turbulence conditions and to determine the number of usable nights (or days) for observing. Basic weather data such as temperature, pressure, humidity, precipitation, wind speed and direction as well as cloud cover can be obtained from weather services, weather satellite data and climate diagnostic archives, which also make long-term meteorological records available, but temporal and spatial resolution may be poor. It is therefore necessary to have an Automatic Weather Station (AWS) installed at a site for continuous monitoring of local meteorological parameters in order to obtain both instantaneous and long-term records of meteorological data thereby establishing a baseline of basic on-site weather data. AWSs such as systems by Davis Instruments and Campbell Scientific Instruments are able to provide reliable measurement of air and soil temperature, barometric pressure, relative humidity, precipitation, wind speed and direction and solar radiation. Data are automatically recorded to a data logger module. A solar panel can be used to charge the 12-volt battery the data logger is connected to. Such an AWS should be installed in close proximity to the telescope. Instruments such as the Boltwood Cloud Sensor and the SBIG All Sky Camera can be installed to monitor cloud cover. The Boltwood cloud sensor detects clouds in and indirect manner – it senses infrared radiation from the sky to determine the sky temperature, compares it to the ambient temperature and reports clear sky conditions if the sky temperature is at least 20°C colder than the ambient temperature. The Boltwood Cloud Sensor also provides the temperature, humidity, dew point and is able to sense wetness and detect daylight. The SBIG All Sky Camera makes use of an SBIG ST237 CCD and a fisheye lens to capture images of the entire sky.

Figure A4.6. The Boltwood
Cloud Sensor at HartRAO.

Figure A4.7. The SAAO All Sky Camera at
Sutherland is located together with the
SALT MASS-DIMM in the ox wagon
enclosure.